Micro and Nanostructuring of Polymers by Femtosecond Laser Pulses

by

Ali Alshehri

Thesis submitted to the

Faculty of Graduate and Postdoctoral Studies

in partial fulfilment of the requirements

for the Doctorate in Philosophy degree in Physics

uOttawa

Department of Physics

University of Ottawa

Canada

Abstract

Micro/Nanostructuring of polymers by femtosecond pulses is of extreme importance because it drives applications in photonics and biomedicine. A femtosecond pulse, with an intensity of $\sim 10^{13}$ W/cm^2, is capable of causing an optical breakdown and inducing permanent modification in the material. With such high intensity, and considering the fact that polymers possess high band gaps, the interaction nature is completely nonlinear, and the material can be modified locally on the surface and in bulk. The irradiated regions exhibit fluorescence, and they display new wetting properties as a consequence of the optical breakdown of a material. The optical breakdown can be investigated by studying the nonlinear absorption. In this thesis, we discuss the nonlinear absorption of fs-laser pulses inside polymers using transmission measurements. We show a step–function–like behaviour of the transmission, dropping abruptly to $\sim 20\%$ at the optical breakdown threshold with a ~ 40 % reduction in the band gap. Utilizing spectroscopy, we show that the laser-modified regions contain randomly distributed nanoclusters. The presence of localized nanoclusters is responsible for exhibiting fluorescence within ~ 10 μm^3 for a single pulse. This feature was exploited to demonstrate high-density data storage in Polymethyl methacrylate (PMMA) without any special material preparation. We demonstrate up to 20 layers of embedded data that can be stored in a standard 120 mm disc. Storage capacity of 0.2 TBytes/disc can be achieved by adjusting read laser parameters. Besides the fluorescence capability induced in the bulk of polymers, the hydrophilicity shown by the fs–laser modified surface is utilized to study selective cell growth on the micro-structured Polydimethylsiloxane (PDMS) surface. We show that the C2C12 cells and rabbit anti-mouse protein attach preferentially to the modified regions when the surface is modified with low pulse energies. However, in the high pulse energy regime, the laser-modified regions exhibit superhydrophobicity inhibiting cell adhesion.

Dedication

In the memory of my father

List of publications included in my thesis

The work presented in this thesis has appeared/accepted in the following publications:

A.M. Alshehri, K.L.N Deepak, D.T. Marquez, S. Desgreniers, and V.R. Bhardwaj. Localized nanoclusters formation in PDMS upon irradiation with femtosecond laser. Optical Materials Express, 5(4):858–869, 2015.

A. M. Alshehri, S Hadjiantoniou, R J Hickey, Z Al-Rekabi, J L Harden, A E Pelling, and V R Bhardwaj. Selective cell adhesion on femtosecond laser-microstructured polydimethylsiloxane. Biomedical Materials, 11(1):015014, 2016.

Deepak L.N. Kallepalli, **Ali M. Alshehri**, Daniela T. Marquez, Lukasz Andrzejewski, Juan C. Scaiano, and Ravi Bhardwaj. Ultra-high density optical data storage in common transparent plastics. Scientific Reports, 6:26163, 2016.

A.M. Alshehri, V.R. Bhardwaj. Transmission based measurements of the nonlinear absorption inside polymers. Accepted for publication in Optical Materials.

Additional Publications

The following papers resulted as part of collaboration with my colleagues, and they are not directly related to this thesis.

F. Baset, K. Popov, A. Villafranca, **A.M. Alshehri**, J-M Guay, L. Ramunno, and V.R. Bhardwaj. Nanopillar formation from two-shot femtosecond laser ablation of polymethyl methacrylate. Applied Surface Science, 357:273–281, 2015.

Yang Li, Ping Lu, Farhana Baset, Zhonghua Ou, Jia Song, **Ali Alshehri**, Vedula Ravi Bhardwaj, and Xiaoyi Bao. Narrow linewidth low frequency noise er-doped fiber ring laser based on femtosecond laser induced random feedback. Applied Physics Letters, 105(10):101105, 2014.

Acknowledgements

I would like to express my gratitude to the several individuals whose help and support assisted my professional growth during the last five years. Sincere thanks are addressed to Professor Ravi Bhardwaj, my PhD project supervisor, who introduced me to the fascinating field of ultrafast photonics, and helped in the completion of this thesis. My thanks are extended to the PDF Deepak Kallepalli. The collaboration with Deepak resulted in the work presented in chapters 5, and 6. I also owe thanks to the rest of the group members, Abdullah, Mitra, Mariam, and May for productive discussions and for providing a good working atmosphere.

During my PhD journey, I worked with great researchers whom I like to acknowledge. My thanks go to Serg Desgreniers, Daniela Marquez, Juan Scaiano, Andrew Pelling, Ryan Hicky, Sebastian Hadjiantoniou, Zenab–Alrekabi, Louis Tremblay, and Johnson Efome. Contribution of each individual is highlighted in the following section. Special thanks go to my colleague, Abdullah Alharbi, for the fruitful discussion during both course time and research time. Deep thanks go to Andrzejewski Lukasz for his technical support. Without Lukasz's help, experiments would not have been implemented in a automatized way.

I am forever in debt to my mother, Maeeda Alshehri, and can never repay her care and support she granted me since my childhood until now; May Allah bless her. Words cannot help to express how grateful I am to my wife, Fatema Alshehri, for her encouragement, support, and patience during those long years. Last but not least, special thanks go to my beloved sons and daughters for all beautiful moments. Your presence im my life is always a relief of the daily troubles.

Author contribution

The work presented in this thesis resulted from the author effort under supervision of Prof. Ravi Bhardwaj. The work was completed in collaborations with other groups. The contribution of each individual is shown here.

Chapter 4 : All experiments related to this chapter were performed by Ali Alshehri, under the supervision of Prof. Bhardwaj. Ali Alshehri and Daniela Marquez recorded the UV-visible spectra. Ali conducted the analysis of data in daily discussions with Ravi. Ali wrote the first draft of the paper related to this work. Prof. Bhardwaj and Ali Alshehri modified and completed the final version.

Chapter 5 : All work related to the direct laser writing is performed by Ali Alshehri, under supervision of Prof. Bhardwaj. Ali and Professor Serge Desgreniers performed micro-Raman and photoluminescence measurements. Ali Alshehri, Daniela Marquez, Deepak Kallepalli, performed emission and excitation spectroscopy measurements. Ali, Prof. Bhardwaj, and Deepak conducted the analysis of data. Ali wrote the first draft of the paper related to this work. Prof. Bhardwaj and Ali Alshehri together modified and completed the final version of the paper. All authors contributed to the final manuscript.

Chapter 6 : All experiments related to this work were planned by Prof. Bhardwaj, Deepak Kallepalli, and Ali Alshehri. Ali and Deepak performed all experiments related to the work presented in this chapter. Ali, Deepak, and Daniela recorded absorption, emission, and excitation spectra. Deepak and Daniela Marquez recorded Fluorescence Life Time Imaging (FLIM) data. Prof. Bhardwaj, Deepak, and Ali conducted the analysis of the data. Deepak conducted the experiment related to the recovery and thermal stability of the recorded images. Andrzejewski Lukasz wrote the Labview program used in this project. Prof. Bhardwaj, Deepak, and Ali wrote the paper related to this work. All authors contributed to the final manuscript.

Chapter 7 : Ali Alshehri and Prof. Bhardwaj planned all experiments related to this work. Ali implemented all experiments related to the direct laser writing. The part that is related to cell seeding on the surface was performed by Zenab–Alrekabi, Ryan Hicky, and Sebastian Hadjiantoniou under the supervision of Prof. Pelling. Zenab did preliminary measurements and the final experiments were performed by Ryan and Sebastian. All confocal and phase contrast images related to this work were taken by Ali, Sebastian, and Ryan. All contact angle measurements were performed by Ali with help from Louis Tremblay and Johnson Efome. Ali analyzed the whole data and Ryan helped in the ANOVA statistical analysis. The first draft of the paper related to this work was written by Ali Alshehri. Prof. Bhardwaj and Ali Alshehri together modified and completed the final version of the manuscript. All authors contributed to the final manuscript.

List of Figures

2.1 Schematic diagram of the multiphoton process 11

2.2 Schematic diagram of the tunnelling process 12

2.3 Schematic diagram of the free carrier absorption and avalanche process . 15

2.4 Processes of transparent dielectrics modification by fs-laser pulses 20

2.5 Schematic diagram of the self-focusing phenomenon 36

2.6 Schematic diagram of the self-phase modulation 37

3.1 Schematic of experimental setup 45

3.2 Schematic of the knife edge experiment 51

3.3 Knife edge positions along the X-axis and spot size along the Z-axis . . . 54

4.1 Nonlinear absorption inside (a) SiO_2, (b) PDMS, and (c)PMMA 66

4.2 Pump pulse transmission as a function of number of pulses in PDMS . . 68

4.3 Transmission of probe pulse through modified regions 71

4.4 Absorption spectrum of pure and laser–modified PDMS, and Tauc's plot. 72

4.5 Colour map showing transmission of white light through embedded filters 74

5.1 SEM image of cross-section of a modified region 79

5.2 Element maps of (a) carbon and (b) oxygen 80

5.3 Photoluminescence from the laser modified PDMS 83

5.4 Raman spectra of laser modified and pristine PDMS 85
5.5 The light absorption spectrum of the pristine and laser–modified PDMS . 87
5.6 Fluorescence emission spectra at different excitation wavelengths 89
5.7 Fluorescence excitation spectra at different emission wavelengths 91

6.1 Fluorescence in PMMA from laser irradiated regions 100
6.2 5-bit encoding dynamics 101
6.3 Generic feature of fs-laser induced Fluorescence in all plastics 102
6.4 5–bit (32 grey-level) image fabrication 105
6.5 Variation of pixel size with laser pulse energy 106
6.6 3D stacked 5–bit images 108
6.7 Package density 109
6.8 Faster image retrieval – 3D stack vs single section 110
6.9 Variation of fluorescence signal with the number of stacked images 111
6.10 Photo-recovery and thermal stability of embedded data 113
6.11 Pearson correlation of images 115
6.12 Spectral analysis of pristine and modfied PMMA 116
6.13 Fluorescence lifetime measurement from the modified PMMA 118

7.1 SEM images of laser modified regions with 110 nJ and 125 nJ 125
7.2 SEM of images of laser modified lines on PDMS with 270 nJ and 430 nJ 126
7.3 Contact angle measurements 128
7.4 XPS spectra 130
7.5 Confocal image of rabbit anti mouse secondary antibody protein 132
7.6 Selective growth of C2C12 mouse myoblasts cells 134
7.7 Cell response on superhydrophobic and surrounding regions on PDMS . . 136

Contents

1 Introduction **1**

1.1 Goals of thesis 4

1.2 Organization of thesis 5

2 Basics of femtosecond-laser interaction with transparent dielectrics **8**

2.1 Deposition and dissipation of fs-pulse energy 9

2.1.1 Nonlinear absorption and ionization 9

2.1.2 Energy dissipation 14

2.2 Material damage 21

2.2.1 Refractive index modification and bulk damage 21

2.2.2 Ablation with fs-pulses 23

2.2.3 Nanoclustering 25

2.2.4 Damage with longer pulses 26

2.2.5 Incubation effect 27

2.3 Propagation of femtosecond laser pulses in dielectrics 29

2.3.1 Linear propagation 29

2.3.2 Optical dispersion 32

2.3.3 Nonlinear propagation 33

2.3.4 Nonlinear refractive index 34

2.3.5 Self-focusing . . . 35
2.3.6 Self-phase modulation . . . 36

3 Experimental methods 41

3.1 Laser system . . . 41
3.2 Materials . . . 42
3.2.1 Dielectric samples . . . 42
3.2.2 Biological samples . . . 43
3.3 Experimental setup . . . 44
3.4 Parameters of the laser beam . . . 48
3.4.1 Pulse duration . . . 48
3.4.2 Power measurements . . . 49
3.4.3 Spot size and knife edge measurements . . . 51
3.5 Characterization techniques . . . 53
3.5.1 Scanning electron microscope (SEM) . . . 53
3.5.2 Energy dispersive spectroscopy (EDS) . . . 55
3.5.3 X-ray photoelectron spectroscopy (XPS) . . . 55
3.5.4 Confocal microscopy . . . 56
3.5.5 Micro-Raman spectroscopy . . . 57
3.5.6 Contact angle measurements . . . 58
3.5.7 UV-visible spectroscopy . . . 58
3.5.8 Emission and excitation spectroscopy . . . 59
3.6 Fluorescence life time Imaging (FLIM) . . . 59

4 Transmission measurements of the nonlinear absorption in polymers 61

4.1 Introduction . . . 62
4.2 Nonlinear absorption . . . 65

4.3 Carbonization of polymers . . . 70
4.4 Reduction of the optical band gap . . . 71
4.5 Embedded micro-optical filters . . . 73
4.6 Conclusion . . . 75

5 Nanoclusters formation in PDMS upon irradiation with fs–pulses 76
5.1 Introduction . . . 77
5.2 EDS measurements . . . 79
5.3 Photoluminescence and micro-Raman spectra . . . 82
5.4 Absorption spectroscopy . . . 87
5.5 Excitation and emission spectroscopy . . . 88
5.6 Conclusion . . . 93

6 Ultra-high density optical data storage in transparent plastics 94
6.1 Introduction . . . 95
6.2 Multi-level encoding dynamics . . . 98
6.3 Recording and retrieving 5–bit images in 3D . . . 104
6.4 Recovery and thermal stability of recorded images . . . 112
6.5 Thermal degradation . . . 114
6.6 Spectral analysis . . . 115
6.7 Conclusion . . . 119

7 Selective cell adhesion on femtosecond laser microstructured PDMS 121
7.1 Introduction . . . 122
7.2 Surface topography . . . 125
7.3 Contact angle measurements . . . 128
7.4 Chemical changes to modified PDMS . . . 129

7.5 Protein adhesion 131
7.6 Cell adhesion 135
7.7 Conclusion 137

8 Conclusion and future outlook **138**

8.1 Summary 138
8.2 Future outlook 141

Chapter 1

Introduction

Manipulation of polymer properties on the micro/nanoscale dimensions is a fast growing field due to its potential numerous applications. Polymers are ideal materials in the fields of micro and nanoelectronics, biomaterials, microfluidic devices, integrated photonics, and cosmetics because of their unique mechanical and optical properties. The mechanical properties of certain types of polymers such as stress and strain are close to those of the human body. This biocompatibility can be exploited in medical applications such as tissue regeneration, scaffolds, and drug delivery. In addition, the optical properties of polymers are similar to most transparent dielectrics in that they possess high optical band gaps. Thus, they do not absorb visible and near infrared light, making them suitable materials in photonics when their properties are modified.

Polymer properties can be altered by irradiating them with energetic particles or light. Such irradiated polymers exhibit unique new properties that other dielectrics such as glass do not. For instance, the irradiated regions of polymers become photosensitive and give broad fluorescence because of the presence of nanoclusters or nanostructures that are formed within the modified regions. Such nanoscale-dimensional materials

are also responsible for alteration of the wetting properties of the irradiated regions. The assembly of nanoclusters or nanocomposites in polymers can be achieved utilizing other techniques such as the casting of films from a mixture consisting of nanoparticles and polymers, plasma deposition, RF co-sputtering, thermal decomposition of thin grown layers, sol-gel, electron beam irradiation, selective oxidization, and by depositing nanoparticles onto a surface and over growing the deposited area with additional matrix material. Each of the above techniques has its own drawbacks, such as requiring a multi-step preparation process, and the difficulty of embedding the nanoclusters inside the material [1–11].

The femtosecond laser technique has emerged as a new and versatile tool, capable of altering permanently the optical and wetting properties of dielectrics including polymers [12, 13]. Unlike the above techniques, using femtosecond laser is a single-step process for which minimal preparation of material is required. The permanent modification of a material properties is driven by the high intensities inherent in the fs–laser pulses because of the short pulse duration. This ultrashort feature allows to modify the material even with small pulse energy through nonlinear interaction.

The first step of the interaction involves excitation of carriers from the valence band to conduction band via nonlinear absorption of the pulse energy. The nonlinear absorption is due to the fact that the photon energy of 800 nm is 1.55 eV while the band gaps of polymers are higher than 3 eV. The mechanisms by which the nonlinear absorption and ionization take place are photoionization and avalanche ionization [14, 15]. The photoionization mechanism includes multiphoton nonlinear ionization and tunnelling ionization. Avalanche ionization occurs when free electrons in the conduction band absorb more photons and gain energy that is higher than the band gap of a material.

This allows it to promote another electron from the valance band to the conduction band through a collision process. After the creation of electron plasma, the energy is transferred from the electrons to lattice on picoseconds time scale. On the nanosecond time scale melting occurs resulting in damage to the material. Subsequently, the optical, chemical, and mechanical properties are completely altered [14, 16–18]. Detailed explanation of the fs–laser interaction with dielectrics is covered in chapter 2.

The fs-laser induced damage in transparent dielectrics is localized and confined to the focal volume because of the ultrashort feature of the pulse. The pulse energy is completely deposited in the system before any thermalization process occurs. The pulse duration is related to the diffusion length of heat by the following equation [19]:

$$l_{th} \approx \sqrt{D.\tau_\circ} \tag{1.1}$$

where $\tau_\circ$ is the pulse duration, and D is the thermal diffusivity. The thermal diffusivity for most polymers are in the order of 1×10^{-2} cm^2/s [20]. With such value, the diffusion length of heat with fs–pulses is ≤ 1 nm.

As a result of the ultrashort feature and the nonlinear interaction, the modified area could beat the diffraction limit when the pulse energy is at the modification threshold. The minimal damage radius r_{min}, by diffraction limit theory, is given by the following equation [21]:

$$r_{min} = \frac{1.22\lambda_\circ}{2NA} \tag{1.2}$$

where $\lambda_\circ$ is the wavelength of the laser, and NA is the numerical aperture of the focusing microscope objective.

Within such a small area/volume, the properties of polymers could be altered com-

pletely as a result of the nonlinear absorption of the laser pulse energy. Eventually, the nonlinear absorption would drive the localized change in density and/or the formation of a new nanocomposites or nanoclusters. The induced nanoclusters possess new behaviours, such as exhibiting fluorescence and displaying new wetting properties. The exceptional fluorescence quality of such localized nanoclusters could be exploited for fabrication of high density data storage in plastics. In addition, the localized alteration in the wetting properties could be utilized in patterned cell growth.

1.1 Goals of thesis

The work presented in this thesis is the contribution of the author to the field of fs-laser interaction with polymers during the course of the Ph.D. project. Despite the long history of the field of fs–laser interaction with polymers, there still remains a great deal to be learned about nonlinear absorption and the nature of the induced damage on the surface and in the bulk. The goals of this thesis are to discuss the nonlinear absorption of fs–pulses in polymers that drives fluorescence and changes in the wetting properties of polymers, to show that the fluorescence feature exhibited by modified regions can be used for data storage devices, and to show that the hydrophilicity induced within the modified surface can be utilized for selective cell growth.

We discuss nonlinear absorption in polymers utilizing transmitted light, as it is the only real–time measurable quantity. Despite the difficulty of the interaction with bulk, transmission measurements provide information about the ionization threshold and shot to shot dynamics. We show a step-function like behaviour in transmission of incident pulses inside polymers, unlike glass for which the absorption decreases gradually with the increase of the pulse energy.

We use spectroscopy to show that the irradiated regions with fs–pulses contain carbonaceous nanoclusters. Such low–dimensional materials are photosensitive and they exhibit fluorescence. We utilize the quality of fluorescence to demonstrate a novel technique to store data in 3D in polymers. The variation of fluorescence signal with the pulse energy is utilized to assign grey levels. The fluorescence signal represents 32 grey levels, which correspond to 5 bits. This novel method offers a storage capacity of 0.2 TBytes per disc of the size of a conventional Compact Disc(CD)/ Digital Versatile Discs (DVD).

Besides the fluorescence capability induced in the bulk of polymers, the micro/nanostructured surfaces exhibit local changes in the wetting properties (hydrophilicity and hydrophobicity). This alteration in the wetting properties is utilized to control cell adhesion to the micro-structured surface of PDMS. We show that the cell adhesion can be controlled in two ways. Cell adhesion is enhanced when the surface is modified with low pulse energies while high energies induce superhydrophobic surfaces, inhibiting the cell attachment. The following section gives more details about each chapter of this thesis.

1.2 Organization of thesis

Though each chapter can be stand alone, the general background of fs-laser matter interactions given in chapter 2, and the detailed description of the experimental procedures in chapter 3, provide an overview that relates to this thesis as a whole.

Chapter 2 gives the basic physics of the interaction of short pulses with transparent dielectrics. It is divided into three main sections: nonlinear absorption and electron–lattice coupling, types of damage, and propagation effects of fs–laser pulses in transparent media. The nonlinear absorption and dissipation of pulse energy are im-

portant for understanding how damage occurs in transparent dielectrics when they are exposed to fs-laser pulses. The section concerning fs-laser induced damage in dielectrics explores the types of damages that have been discussed in the literature. The section on pulse propagation provides a picture of some complications that could occur as a result of the self–actions of the pulse, such as self–focusing, and self–phase modulation. These complications should be avoided in the work related to data storage, which is discussed chapter 6.

Chapter 3 describes in detail the setups used in all experiments included in this thesis. It addresses experimental procedures and techniques that were used to measure laser parameters such as the pulse duration, the pulse energy, and the spot size. This chapter also gives an overview of the characterization techniques that were utilized to characterize the damage.

Chapter 4 discusses the nonlinear absorption of intense ultrashort laser pulses with polymers utilizing the transmission measurements. A step-function like self-limiting behaviour in transmission of incident pulses inside polymers is demonstrated, dropping abruptly at a certain threshold to $\sim 20\%$ ($\sim 35\%$) in PDMS (PMMA) and clamping beyond the threshold fluence. This chapter also discusses the blackening of the material as a result of the carbonization process. This process is associated with a significant reduction in the bandgap.

Chapter 5 discusses the formation of localized carbonaceous and siliconaceous clusters, confined to the modified region on a micron scale, when PDMS is irradiated by intense fs-laser pulses. Quasi-crystalline silicon nanoclusters, which vary in size depending on the incident laser fluence, are discussed utilizing micro–Raman technique. Broad photoluminescence from the modified region is presented with a shift toward a longer

wavelengths as the excitation wavelength is increased. Four distinct absorption bands contribute to the emission from the laser-modified region; two absorption bands are ascribed to each of the carbonaceous and siliconaceous clusters.

Chapter 6 demonstrates a completely novel, simple, and inexpensive method for storing data in 3D of commonly available plastics. This work is based on utilizing the fs–laser pulses to induce fluorescence centers in a localized region, representing a bit. Upon excitation by a read laser, each bit emits fluorescence with intensity that varies linearly with the energy of the laser pulse used to record the bit. By assigning different grey levels to the fluorescence intensity, multi-level data is encoded in each bit. This technique has the capability to transform the standard DVD/Bluray disc made of polycarbonate into a high-density storage disc with capacities as high as 0.5 TBytes.

Chapter 7 shows a single-step process for achieving patterned cell growth on a bio-compatible surface by altering chemical and topographical properties of the surface using a femtosecond laser. Selective and patterned growth of C2C12 mouse myoblast cells was achieved by nano/microstructuring the surface with two different energy regimes. At low laser pulse energies, cells attached to the laser-modified regions. At high pulse energies, the laser irradiated regions exhibited super-hydrophobicity, and cell attachment was inhibited. Enhanced cell adhesion was increased by a factor of 12 relative to the pristine material when the PDMS surface was initially treated with pluronic.

Chapter 8 reemphasizes the key points of this thesis. It also addresses several unresolved questions regarding the fluorescence from the fs-laser modified polymers. Finally, it gives suggestions for research in the area of fs-laser induced nanoclusters in polymers as well as recommendations for experiments that help in identifying such clusters.

Chapter 2

Basics of femtosecond-laser interaction with transparent dielectrics

This chapter presents the basic physics of the interaction of fs-laser pulses with transparent dielectrics, and the subsequent damage that could happen to the material. Fs-laser pulses with moderate energies can produce extremely high peak intensities when tightly focused, due to very short pulse durations. Such extreme intensities cause the material to be readily modified or ablated via a nonlinear ionization process. The damage occurs in transparent dielectrics by a fs-pulse basically pivots on two mechanisms, energy deposition and energy dissipation [22, 23]. This chapter covers three main parts: the deposition and dissipation of the pulse energy in dielectrics, types of damage that occur in the material, and the propagation effects of a fs-laser pulse in transparent media.

2.1 Deposition and dissipation of fs-pulse energy

2.1.1 Nonlinear absorption and ionization

The process of fs-laser pulse energy deposition in transparent dielectrics is well understood. A fs-pulse with $\lambda = 800$ nm can not be absorbed directly by dielectrics because the photon energy (1.55 eV) is less than the optical band gap of most glasses and polymers [14–16, 24–26]. For instance, the band gap of PDMS is ~ 5 eV [27], so at least four photons should be absorbed simultaneously to excite one electron from the valance band to the conduction band. Such nonlinear excitation requires very high intensity. Since the intensity depends inversely on focal spot size, tight focusing of a fs-pulse in a dielectric material leads to extreme intensities by which nonlinear excitation of the electron from the valance band to the conduction band can be fulfilled. The nonlinear excitation includes two mechanisms: photoionization and avalanche ionization. The photoionization process can be divided into two distinct regimes, based on the laser intensity and frequency: multiphoton ionization and tunnel ionization. Both processes will be discussed separately in sections 2.1.1.1, and 2.1.1.2.

2.1.1.1 Multiphoton ionization

Multiphoton ionization (MPI) refers to the excitation of the electron from the valance band to the conduction band in transparent dielectrics by the simultaneous absorption of multiple photons. Figure 2.1 shows a schematic diagram of the multiphoton process. In this figure, five photons, with 800 nm, are required to excite one electron from the valance band to the conduction band. The multiphoton process is highly dependent on the laser intensity. The multiphoton absorption rate is expressed by the following

equation [14]:

$$P(I)_{MPI} = \sigma_m \left(\frac{I}{\hbar\omega} \right)^m \cdot N_s \tag{2.1}$$

where σ_m is the m photons absorption cross section to elevate an electron from the valance band to the conduction band, $\hbar$ is the reduced Planck constant, ω is the frequency of the laser beam, I is the laser intensity, and N_S is the atomic density of solids. The number of photons is determined by the smallest m that satisfies the relation:

$$m\hbar\omega \geq E_g \tag{2.2}$$

where E_g is the bandgap energy of the dielectrics materials. For example, the optical band bandgap of a pure PMMA is 4.58 eV [28] . To fulfil the condition in equation 2.2, the ionization via multiphoton process should involve simultaneous absorption of three photons. The three-photon absorption cross-section of PMMA is $\sim 7{\times}10^{-86}$ ($cm^6.s^2/photons^3$) [29], requiring typical intensities of about 10^{13} W/cm^2.

2.1.1.2 Tunnelling ionization

At intensities higher than those required for MPI, tunnel ionization starts to play a major role during the interaction of the fs-laser pulse with dielectrics. For atoms, the tunnel ionization process occurs when the field of the laser suppresses the Coulomb potential, which holds the electron and atom together, allowing the electron to escape from its parent atom. In solids, the tunnelling ionization takes place by the direct transition from the valance band to conduction band. The process of tunnelling is shown schematically in figure 2.2. In tunnelling, the strong laser field distorts the band

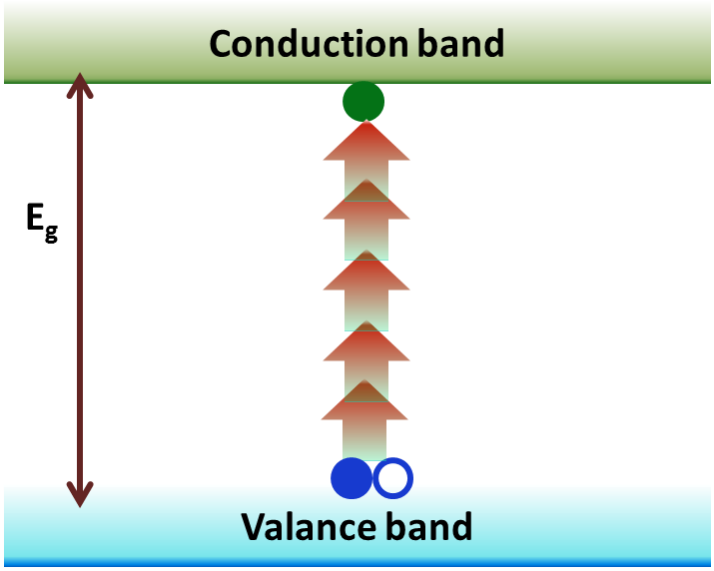

Figure 2.1: Schematic diagram of the multiphoton process of fs-laser pulses in transparent dielectrics.

structures and reduces the band gap of the material, allowing the electron to tunnel to the conduction band in a time-scale shorter than the pulse duration. Tunnelling can be differentiated from multiphoton ionization by calculating the Keldysh parameter.

2.1.1.3 Keldysh parameter

Although the concept of multiphoton ionization and tunnelling ionization is different, both can be described with Keldysh theory [30]. Typically, the Keldysh parameter is used to determine the transition between multiphoton and tunnelling photoionization. The Keldysh parameter (γ) is given by the following equation [15, 22]:

$$\gamma = \frac{\omega}{e}\left[\frac{m^* cn\epsilon_\circ E_g}{I}\right]^{1/2} \tag{2.3}$$

where I is the intensity of the laser at the focus, e is the charge of the electron, m^* is the effective mass of the atom, c is the speed of light, ω is the frequency of the laser,

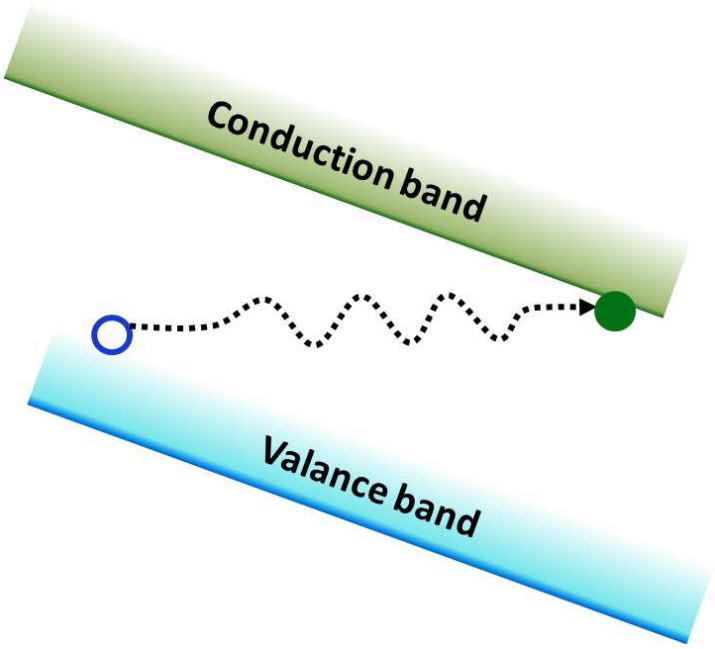

Figure 2.2: Schematic diagram of the tunnelling process of fs-laser pulses in transparent dielectrics.

and $\epsilon_\circ$ is the permittivity of the free space.

From equation 2.3, the Keldysh parameter depends on the laser frequency and laser intensity. In addition, it depends on material properties such as the refractive index (n) and optical band gap (E_g). In the limit of low frequencies, $\gamma \ll 1$, the ionization is in the tunnelling regime. In contrast, for high frequencies, but not to the extent of reaching the linear absorption regime, $\gamma \gg 1$, and the ionization is to be governed by the multiphoton process.

In transparent dielectrics, an intensity of $\sim 10^{13}$ W/cm^2 is high enough to modify the properties of a material. In such a regime of intensity, the interaction of the fs-pulse with transparent dielectrics is mostly dominated by the multiphoton ionization.

2.1.1.4 Avalanche ionization

Once seed electrons are produced by MPI, avalanche ionization can play a dominant role in generating free carriers. The avalanche ionization process entails free carrier absorption followed by impact ionization, as shown in figure 2.3. The initial existence of electrons in the conduction band is provided by either thermal excitation or the photoionization, multiphoton or tunnelling processes. The presence of an electron in the conduction band allows it to linearly absorb several photons, promoting it to higher states within the band [15, 22]. The sequential absorption of m photons and the multiple electron-phonon (lattice) collisions make electrons gain energy that satisfies the conduction band minimum, as in equation 2.2, allowing valance electrons to be promoted from the valance band to the conduction band via a collision process. Hence, the collision process ends up with two electrons in the conduction band [15, 22, 31]. This process can repeat itself as long as the laser pulse is present with enough intensity leading to excitation of large number of valance electrons. Thus, the electron density(N_e) in the conduction band increases according to the following equation [14]:

$$\frac{dN_e}{dt} = \beta(I)N_e; \tag{2.4}$$

where β is the avalanche ionization rate. It has been found that the avalanche rate changes linearly with the intensity of the laser pulse (I) as follows [14, 15]:

$$\beta(I) = \alpha_{av}I; \tag{2.5}$$

where α_{av} is the avalanche ionization coefficient. From equations 2.4 and 2.1, both multiphoton ionization and avalanche ionization depend on the laser intensity. Almost

all transparent dielectric materials can be modified and even ablated with intensities in the order of $10^{13} W/cm^2$. In this regime of intensities, Keldysh parameter γ in equation 2.3 is > 1. Hence, the injection of electrons in the conduction band of a dielectric by a fs-laser pulse is due to a combination of multiphoton ionization and avalanche.

It is difficult to know the exact contribution of each ionization process. However, rate equation proposed by *Stuart, et al* describes the nonlinear ionization of a dielectric by a fs-laser pulse in the regime of multiphoton and avalanche [14]. Under combined contribution of multiphoton ionization and avalanche ionization, equation 2.4 must be modified to the following equation:

$$\frac{dN_e}{dt} = \beta(I)N_e + P(I); \tag{2.6}$$

where $P(I)$ is the multiphoton rate. The combined action in the rate equation can be understood as follows: at the beginning of pulse, the contribution is from the multi photon process. This process reaches its maximum at the peak of the pulse, i.e in the first half of the pulse, and then it starts declining until it becomes unimportant at the end of the pulse. Electrons generated at the peak of the pulse play as seed electrons for the avalanche. So, strictly speaking, the ionization process is mainly dominated by avalanche in the second half of the pulse.

2.1.2 Energy dissipation

2.1.2.1 Plasma formation and electron-lattice coupling

Unlike the energy absorption process described above, dissipation of the pulse energy out of the focal zone is poorly understood. However, the widely accepted scenario is

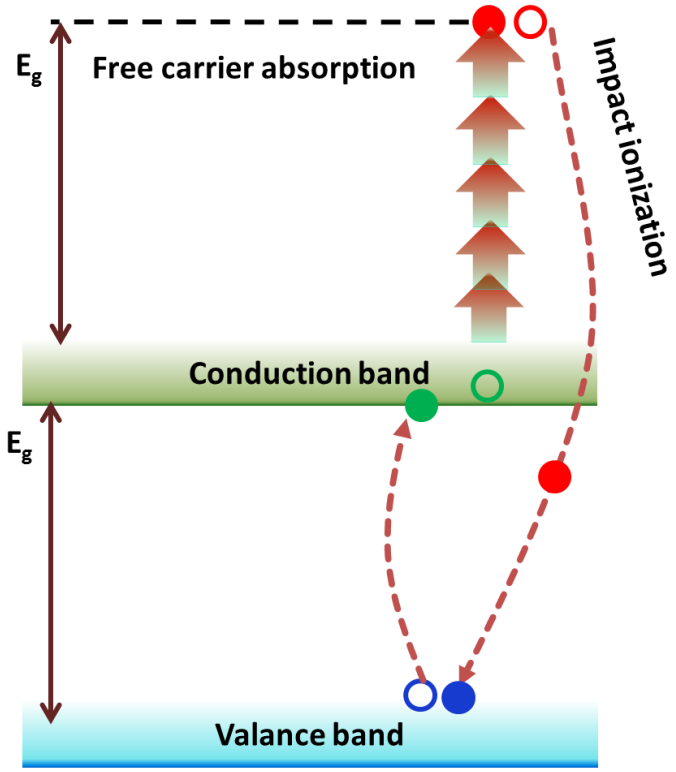

Figure 2.3: Schematic diagram of the free carrier absorption and avalanche process during the interaction of fs-laser pulses with transparent dielectrics. Conduction electrons (green) absorb photons and become free carriers (red), and then collide with valance electrons (blue).

that the accumulation of carriers (electrons), in the conduction band of the material by the multiphoton and avalanche, leads to the formation of free electron plasma. In the presence of the laser pulse, the electrons accumulate in the conduction band until the frequency of the plasma reaches the frequency of the incident pulse. Under this condition, the plasma is called critical plasma [14]. Such a dense plasma absorbs the pulse energy via free-carrier absorption [15]. After the pulse is gone, electrons start to give the energy to lattice through collisions in a time ranging from hundreds of femtoseconds to picoseconds. This energy dissipates out of the focal zone via thermal diffusion in longer time extending from picosecond to tens of microseconds. When the temperature of the material is high enough, it breaks the bonds and subsequent

rearrangement leads to refractive index modification, or ablation.

The absorption of the plasma can be expressed by the Drude model, and the plasma frequency (ω_p)is given by the following equation:

$$\omega_p = \sqrt{\frac{e^2 N_e}{\epsilon_\circ m^*}} \tag{2.7}$$

Where N_e is the carrier density, $\epsilon_\circ$ is the electric permittivity, and m^* is the effective mass. At the critical density ($N_{cr} \sim 10^{21} cm^{-3}$), the plasma oscillates with a frequency equalling the laser frequency. Such a plasma linearly absorbs energy from the remaining fraction of the pulse. The absorption coefficient, $\alpha_\circ$, is related to the imaginary part of the refractive index as follows [22, 31]:

$$\tilde{n} = n_r + i n_i \tag{2.8}$$

and the absorption coefficient is given by

$$\alpha_\circ = \frac{2\omega n_i}{c} \tag{2.9}$$

where n_r is the real refractive index and n_i is the attenuation coefficient. The real part is related to the phase velocity of the wave while the imaginary part expresses the absorption. Below the critical plasma, the real part in equation 2.8 is large and the absorption is negligible. In this case, the plasma acts as dielectric and the light is able to propagate through it. In contrast, if the plasma frequency is above the critical, the plasma behaves as a conductor. In this case, the imaginary part is large, and significant part of the pulse is absorbed by the plasma.

The complex refractive index is related to the dielectric function by $\sqrt{\tilde{\varepsilon}} = \tilde{n}$, which,

from the Drude model, can be given by equation 2.10

$$\tilde{\varepsilon} = 1 - \omega_p^2 \left[\frac{t^2}{1+\omega^2 t^2} + i \frac{t^2}{\omega t(1+\omega^2 t^2)} \right] \tag{2.10}$$

Hence, the absorption coefficient is given by the following:

$$\alpha_\circ = \frac{2\omega n_i}{c} = \frac{\omega_p^2 t}{n_r c(1+\omega^2 t^2)} \tag{2.11}$$

where t is the Drude scattering time, which is typically around 0.2 fs [32].

2.1.2.2 Electron energy

At the end of the fs-laser pulse, the energy is held mostly in the electron sub-system. Thus, the maximum electron temperature, T_e, can be calculated from the energy conservation law [31]. Electrons in the conduction band with energy of $k_B T_e \ll E_f$ form the electron gas plasma with a density number of N_e, the heat capacity of C_e is given by the following equations:

$$C_e = \frac{\pi^2 k_B^2 T_e}{2E_f}, \tag{2.12}$$

where k_B is the Boltzmann constant and E_f is the Fermi energy. The energy density of such plasma is expressed by equation 2.13,

$$W_e = C_e N_e T_e = \frac{\pi^2 k_B^2}{2E_f} N_e T_e^2 \tag{2.13}$$

and the energy density that is absorbed by the material during the pulse time, t_p is:

$$W(t_p) = \frac{2\alpha_\circ F_p}{l_{abs}}; \quad F_p = \int_0^{t_p} I(t)dt \tag{2.14}$$

where l_{abs} is the skin depth, F_p is the fluence, and $\alpha_\circ$ is the absorption coefficient. From equations 2.13 and 2.14 the maximum temperature of the electron plasma can be calculated from equation 2.15

$$T_{e,max} = \sqrt{\frac{4E_f \alpha_\circ F_p}{\pi^2 k_B^2 N_e l_{abs}}} \tag{2.15}$$

By taking $E_f \simeq 5$ eV, $N_e \simeq 7 \times 10^{22}/\text{cm}^3$, $F_p \simeq 2$ J/cm^2, and $\alpha_\circ / I_{abs} \simeq 1.6 \times 10^{-5}$ cm, the maximum electron temperature for a glass can be estimated to be $\sim 5.5 \times 10^4$ °K.

2.1.2.3 Lattice energy

At the end of the laser pulse, the temperature of the lattice is equal to the room temperature because the pulse energy is completely stored in the electron subsystem. The maximum energy can be estimated by taking into consideration the principle of energy conservation neglecting the energy losses due to scattering or ionization and modifications of the dielectric function:

$$C_e N_e T_e + C_l N_a T_l = W(t_p) \tag{2.16}$$

where C_l is the heat capacity of the lattice, N_a is the atomic density, and T_l is the lattice temperature. Electron–electron and electron–lattice collision typically proceed on time scales around hundred fs; energy transfer to the lattice takes place within a few picoseconds. When the process of electron-lattice energy transfer is completed, $T_e \approx T_l = T$.

The previous argument gives a simple picture of the transfer of pulse energy from electrons to lattice. The temperature evolution of the electron and lattice over the

time-scale until it reaches the thermal equilibrium (sub picoseconds) can be described by the two temperature model. In this model, the hot electrons start giving energy to the cold lattice through electron-phonon collision. Although the two temperature model was initially developed to describe the ultrashort pulse interaction with metal [33], it has recently been used to describe the interaction of fs-laser pulses with dielectrics [17]. This is because the free electron plasma behaves like metals, and absorbs photon energy linearly before any change occurs in the phase of the material. The two temperature model is given by equations 2.17, and 2.18, which should be solved simultaneously:

$$C_e(T_e)\frac{\partial T_e(t,r,z)}{\partial t} = \nabla(k_e(T_e)\nabla T_e) - G(T_e - T_l) + S(t,r,z) - H_e(t,r,z), \tag{2.17}$$

$$C_l(T_l)\frac{\partial T_l(t,r,z)}{\partial t} = \nabla(k_l\nabla T_l) + G(T_e - T_l) - H_l(t,r,z), \tag{2.18}$$

where, S is the laser energy density and is given in (W/m^3), k_e is the electron conductivity, k_l represents the lattice conductivity, H_e is the energy loss due to electron escape, H_l is the energy loss term due to the lattice removal, and this term contains both sensible heat and latent heat, C_e is the specific heat capacity of electrons, C_l is the specific heat of the lattice, and G is the electron–lattice coupling factor. Equation 2.17 shows that the electrons gain energy from the laser pulse, which contributes to raising their temperature. After that, the energy is distributed to the lattice via electron–lattice coupling as described by equation 2.18. After reaching the thermal equilibrium between electron temperature and lattice temperature, the energy is distributed to further parts of the material by lattice thermal diffusion. When the temperature of the lattice becomes higher than the breakdown threshold, permanent damage occurs within the irradiated spot. The degree and type of damage depend on the laser parameters such as

laser intensity, pulse duration and the repetition rate. They also depend on the thermal diffusion properties of the material.

To summarize, the nonlinear absorption of the fs–pulse energy and the subsequent thermalization processes that lead to the material modification are shown as a function of time scale in figure 2.4. The pulse energy is transferred to electrons by photoionization, either by multiphoton absorption or tunnelling as long as the pulse is present. Avalanche ionization takes place during the pulse time and it dominates in the second half of the pulse. Electron-electron collision and electron-lattice coupling start after the pulse disappears and the material reaches thermal equilibrium in picoseconds. Shock wave and thermal expansion that lead to the material modification or removal occur in nanosecond timescales and longer.

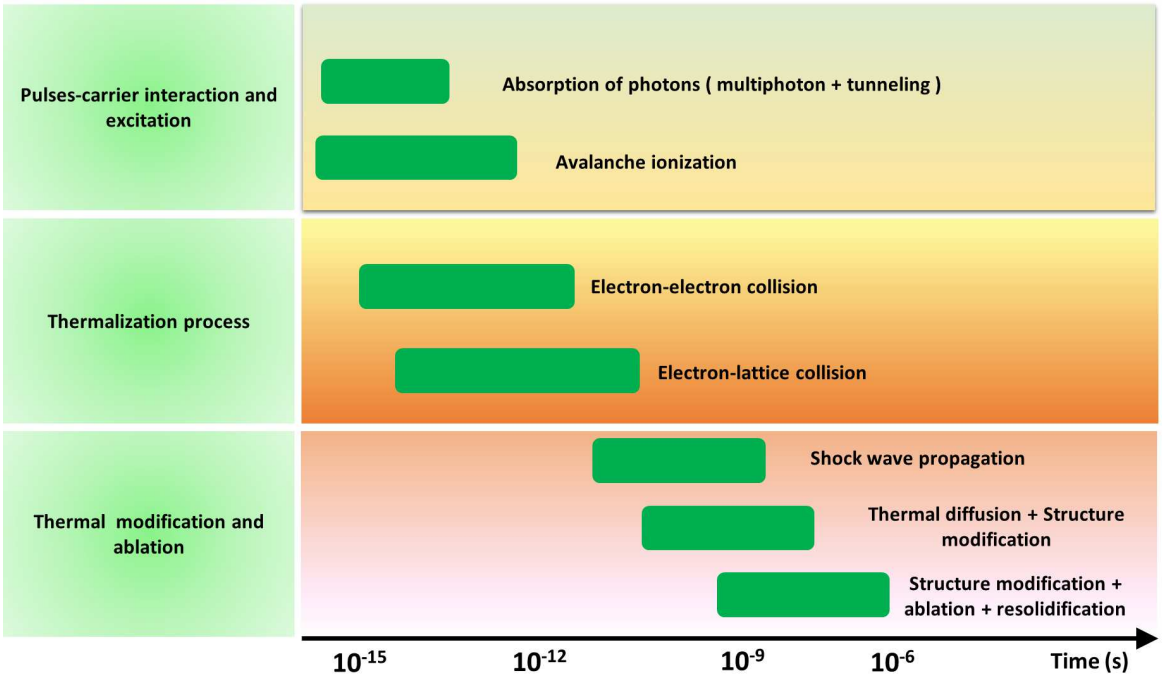

Figure 2.4: Processes of transparent dielectrics modification by a fs-laser pulse as a function of time. Each process is given a different colour (big bars). The small bars represent typical timescales for the relevant process.

2.2 Material damage

2.2.1 Refractive index modification and bulk damage

If the deposited energy in the material is high enough for nonlinear ionization, permanent damage occurs in the material, either on the surface or inside the bulk. Inside the bulk, the degree or the class of the damage induced by fs-pulses with λ= 800 nm can be classified into three types based on the laser fluence: smooth refractive index modification, birefringent refractive index change (nanogratings), and void formation (micro explosion) [19].

Smooth refractive index modification occurs when the pulse energy is very low, just above the modification threshold. In the literature, several mechanisms have been proposed to explain smooth refractive index modification in dielectrics upon irradiation with fs-pulses. One scenario is related to localized melting followed by quick re-solidification in the focal zone. This sudden process drives density variation that results in refractive index modification. This mechanism was reported in some materials like fused silica [12]. In another scenario, fs-pulse could lead to bond breaking followed by rearrangement of atoms. This process might increase or decrease the material density based on the thermal properties of the material and parameters of the laser. Both higher and lower refractive indices were reported in the literature. For instance, negative and positive refractive index contrast was reported in PMMA based on the laser parameters [34,35].

The birefringent refractive index change is caused by the periodic difference in the material density or composition within the irradiated volume leading to the formation of a nanograting-like structure [36]. The grating structure was always found to be oriented perpendicularly to the electric field of the laser and the direction of the beam

propagation, giving rise to birefringence. Currently, the essence of these self-organized nanostrucures is not fully understood. It has been proposed that the self-organized nanostructure is created as a result of an interference phenomenon that causes periodic modulation in the electron plasma concentrations, leading to a frozen modulation in the structures within the irradiated spot. In this model, the temperature and density of the plasma at which the nanograting–like structure occurs are not consistent with pulse energy delivered to the system. A recent theory to explain the formation of self-organized nanogratings was developed by *V.R. Bhardwaj, et. al.* [36]. This theory proposes that the pulse will ionize the material leading to the formation of inhomogeneous plasma. After multiple pulses, the plasma hot spots can grow in the shape of the spherical plasma. The local field enhancement at the boundary leads to asymmetric evolution of the spherical nanoplasma in the direction that is perpendicular to the polarization of the laser as well as the direction of the beam(k). The electric field at the pole and the equator of the sphere are given by equations 2.19, and 2.20, respectively:

$$E_P = \frac{3E\epsilon'}{\epsilon' + 2} \tag{2.19}$$

$$E_E = \frac{3E}{\epsilon' + 2} \tag{2.20}$$

where E_E and E_p are the local fields at the equator and poles of the sphere, E is an overall field, and ϵ' is the ratio of permittivities of nanosphere and dielectric medium. When $\epsilon' < 1$, the plasma is underdense and the field enhancement is along the equator, giving rise to nanoplane formation perpendicular to the laser polarization. Further growth of nanoplanes leads to quasi-metallic waveguiding, which results in the formation of a nanograting structure with a period of $\sim \lambda/2n$, where n is the refractive index of the

dielectric. Nanogratings are formed with moderate pulse energies, for example ($\sim$ 300 nJ for 0.45-NA focusing of 800 nm [36]).

If $\epsilon' > 1$, the plasma is overdense for which electron plasma density N_e is greater than the critical density N_{cr}. Under this condition, the plasma is akin to metallic picture because of the high density conduction electrons. So, a metal spheroid was used to model the overdense plasm [36]. In such case, the field is enhanced at the poles, and this leads the plasma to be elongated with the electric field of the laser [36, 37]. This has been confirmed in previous work by our group [38].

At pulse energies $>$ 500 nJ, when 800-nm is focused with 0.6 NA microscope objectives, micro-explosion takes place and a void is formed in the centre of the focal zone. Void formation occurs when high pressure is generated in the centre of the focal zone. When the pressure is higher than the young modulus of the material, a shock wave is generated and it propagates, leaving behind a void or less dense material [39].

2.2.2 Ablation with fs-pulses

Laser ablation is defined as the process by which the material is completely removed from the target as a result of direct absorption of the laser energy. Ablation occurs when the energy density of the focused pulse is so high that it overcomes the ablation threshold of the material [40].

Fs-laser ablation of the transparent dielectric materials is due to two mechanisms: Coulomb explosion and thermal vaporization [40]. The Coulomb explosion takes place at intensities close to the ablation threshold. In this process, if the pulse energy is high enough, the electrons gain kinetic energy and are ejected from the surface of the material. An electric field is created due to the charge separation between the moving

electrons and the parent ions at the surface of the target. Such an electric field is formed when the absorbed energy is higher than the Fermi energy of the material. In addition, the parent atoms are positively charged and the time that is needed for the bulk electron to refill the holes that were left behind the ejected electrons is in the order of picoseconds or even longer. Thus, the positively charged region becomes electrostatically unstable and a repulsion force arises between the positive ions, causing the surface to break apart and emit positive particles that accelerate in the remaining field [23].

If the laser intensity is significantly higher than the ablation threshold, beside Coulomb explosion, thermal vaporization also leads to ejection of material. Strong phonon emission is induced by the sudden laser-generated conduction electrons. Electron and lattice systems reach thermal equilibrium a few picoseconds after the end of the fs-pulse. At such time, the material in the irradiated zone starts expansion and several phenomena might take place such as melting, decomposition, evaporation, and photomechanical ejection. All of those phenomena result in ejection of material from the target surface [22, 23].

The presence of the two mechanisms was confirmed by time-of-flight mass spectrometry. Two components of emitted ions and electrons were reported during the ablation process with ultrafast laser pulses, fast and slow. The fast component, whose kinetic energy is high, was found to be composed of positive ions, and it was attributed to a Coulomb explosion. The slow component consists of the thermalized ions and electrons, and it was ascribed to the ablated particles with thermal process. In addition, the thermalization process leads to the ejection of large ions [23, 40–42].

There are some differences between the two mechanisms including the time-scale at which each process takes place, the quality of ablation, and the quantity of the material

that is ejected from the surface by each process. The Coulomb explosion takes place in picoseconds, while thermal ablation occurs in nanoseconds or even longer. In the Coulomb explosion process, the depth of the ablated region is a few nanometers per pulse, producing a shallow hole with a smooth surface. In contrast, the ablation rate per pulse as a result of the thermal process is magnitudes higher in comparison with that of the Coulomb explosion, generating a rough surface. Furthermore, the Coulomb explosion is known to be a cold process compared to thermal ablation. The above scenario is unique to ultrafast laser pulses. Thus, it is instructive to discuss the ablation process with longer pulses (section 2.2.4).

All damage types discussed in sections 2.2.1 and 2.2.2 represent macroscopic change in the irradiated regions. It is also instructive to discuss changes that occur on the microscopic scale when fs-pulse interacts with dielectrics and polymers. These changes include, for example: crystallization, amorphization, and clustering. Since this topic is very broad, the focus of the subsequent section will be on nanoclustering, which relates to the capability of the fs-laser modified regions in polymers to produce fluorescence and show different wetting properties.

2.2.3 Nanoclustering

This section provides an overview of nanocluster formation by fs-laser pulses, and chapter 5 discuses it in more detail. Nanoclusters are molecular entities that consist of atoms that are connected to one another and exhibit fluorescence properties. The formation of nanoclusters in a material entails two steps: the generation of plasma that has neutral atoms by photo ionization, and chemical reactions that are based on the collision and then lead to aggregations of neutral atoms and active ions [43]. The high temperature

and pressure that are generated in the focal zone lead to chemical bonds breaking and a formation of new bonds, via inelastic collisions. This process occurs in a time-scale of 0.1 to 10 ps [44].

The mechanism of the formation of nanoclusters by intense pulses is not completely understood. However, it is widely accepted that the inelastic, sticky collision is the process by which nanoclusters are formed. Such a collision might be between two neutral atoms, an atom-cluster, and a cluster-cluster. The assembly process starts with a dimer formation of two neutral atoms and a trimer is formed via third collision; this process of inelastic, sticky collision continues on. The size and shape of the nanocluster depend on a combination of laser parameters and material properties [31]. The work related to this thesis focuses on the fluorescence and wetting properties of the nanoclusters induced in polymers by fs-laser pulses.

2.2.4 Damage with longer pulses

The interaction of long pulses with transparent dielectric materials is quite different from that of ultrashort pulses. If the pulse duration is longer than a few tens of picoseconds, a significant fraction of the excited electron energy is transferred from the electrons to the lattice within the time–scale of pulse duration. For long pulses, the mechanism responsible for the promotion of electrons from the valance band to the conduction band is dominated by avalanche impact ionization. Thermally excited electrons, or the presence of defect states provides initial free carriers in the conduction band.

The long pulse duration enables the exponential growth of the electrons density in the valance band.

The process responsible for the transfer of energy from hot electrons to lattice, in the

presence of laser pulses, is thermal diffusion. Once the temperature of the irradiated zone overcomes the binding energy of the material, the material melts or fractures and damage occurs. The material damage that is created by longer pulses, tens of picoseconds and nanoseconds, is different from that induced by fs-laser pulses. The material starts to be ablated while the pulse is still present. Hence, the collateral damage resulting from long pulses is high in comparison to the damage caused by fs-laser pulses. Consequently, the surface of the ablated area is rough and material is ablated outside the focus region. In contrast, it is smooth and localized when a fs–pulse is used.

In general, the time that is required for the modification process to be completed in transparent materials, either by fs-laser pulses or by longer pulses, is in the scale of microseconds, or even longer. Therefore, another factor that should be considered is the repetition rate of the laser. The effect of the time interval between pulses is known as the incubation or accumulation effect. In the following section, the effect of incubation on the modification of transparent dielectrics will be discussed.

2.2.5 Incubation effect

The incubation effect is the process in which the ablation threshold depends on the number of pulses (N). The incubation effect is the result of two possible processes: accumulation of heat from pulse to pulse and the repetitive defects induced in the material. The heat diffusion time in the irradiated zone is in the nanosecond time–scale. Thus, the modification of transparent dielectrics with an oscillator is different from that with an amplifier because the typical repetition rate of the oscillator is $\sim$ 80 MHz versus a KHz regime for the amplifiers. Hence, the time between pulses is $\sim$ 10 ns for the oscillator versus tens of microseconds for most amplifier. Using high repetition

rate lasers in the micromachining allows the heat to accumulate from pulse to pulse. Such lasers allow machining with low pulse energies.

The second mechanism responsible for incubation effect is the accumulative defects within the irradiated zone. Defects are due to changes in chemical, mechanical and optical properties of the irradiated regions. Such accumulative defects cause the modification or ablation occur at lower pulse energies [45]. The density of defects increases from pulse to pulse until it reaches the saturation. The ablation threshold of the material decreases with the number of pulses, (N), and it can be expressed by

$$F_{th}^{N} = F_{th}^{1} N^{S-1} \tag{2.21}$$

where F_{th}^{1} is the ablation threshold for a single pulse and S is the incubation factor. When S equals 1 there is no incubation. In the case of an infinite pulse number, equation 2.21 can be modified to be

$$F_{th}^{N} = F_{th}^{\infty} + \Delta F_{th}^{1,\infty} N^{S-1} \tag{2.22}$$

where $\Delta F_{th}^{1,\infty}$ is the difference between the threshold with infinite number F_{th}^{∞} and the threshold of a single pulse, F_{th}^{1} [46]. In general, the incubation effect reduces the ablation threshold of a material. For example, the ablation threshold fluence of PMMA is 2.6 J/cm^2 for a single pulse while 1.4 J/cm^2 is enough to ablate the material with three pulses [38]. Since we are dealing with high intensities, it is instructive to discuss the propagation of fs–laser pulses in transparent media.

2.3 Propagation of femtosecond laser pulses in dielectrics

Previous sections of this chapter have discussed the absorption mechanism of highly intense fs–pulses in dielectrics, the dissipation of pulse energy within the irradiated regions, and the damage that could occur in the material. The following sections will explore linear and nonlinear propagation of fs–laser pulse in transparent dielectrics and polymers. The complications that could occur as a result of the linear and nonlinear propagation of the pulse through polymers will be highlighted.

2.3.1 Linear propagation

In the linear regime, the light does not change the frequency when it passes through the material. The material properties also do not depend on the field intensity of the light. In this regime, the response of optical system can be described by the relation between the polarization induced in the material and the strength of electric field. The interactions of fs-pulses with transparent dielectrics are described by Maxwell's equations [47]

$$\nabla \cdot \vec{D} = \rho \tag{2.23}$$

$$\nabla \cdot \vec{H} = 0 \tag{2.24}$$

$$\nabla \times \vec{E} = -\mu_{\circ} \frac{\partial \vec{H}}{\partial t} \tag{2.25}$$

$$\nabla \times \vec{H} = \frac{\partial \vec{D}}{\partial t} + \vec{J} \tag{2.26}$$

, where $\vec{E}$ is the electric field, $\vec{B}$ is the magnetic field, and $\vec{D}$, $\vec{H}$ are the derived fields. ρ is the free charge density, $\mu_\circ$ is the magnetic permeability, and $\vec{J}$ denotes the current density. By assuming a nonmagnetic material, which contains no current and no free charge, and by taking into consideration only the dipole moment response of the material, one can get the wave equation

$$\nabla \times \nabla \times \vec{E}(r,t) + \frac{1}{c^2}\frac{\partial^2 \vec{E}(r,t)}{dt^2} = \frac{-1}{\epsilon_\circ c^2}\frac{\partial^2 \vec{P}(r,t)}{\partial t^2} \tag{2.27}$$

where P is the dipole moment vector or the polarization, c is the speed of light, and $\epsilon_\circ$ is the electric permittivity of the space. In the linear regime, the laser intensity should be low, and the polarization is related to the electric field by

$$\vec{P}(r,t) = \epsilon_\circ \chi^{(1)} \vec{E}(r,t) \tag{2.28}$$

where the $\chi^{(1)}$ is the linear susceptibility tensor. For the isotropic media, $\chi^{(1)}$ is scalar and the tensor picture of the susceptibility can be dropped, reducing the wave equation 2.27 to [47]

$$\nabla^2 \vec{E}(r,t) + \frac{(1+\chi^{(1)})}{c^2}\frac{\partial^2 \vec{E}(r,t)}{\partial t^2} = 0 \tag{2.29}$$

The equations 2.27 and 2.29 represent the wave equations for the propagation of electromagnetic wave through transparent media. The electric field of electromagnetic plane wave propagating along the z-axis is given by [47]

$$\vec{E}(z,t) = A_\circ e^{i(Kz-\omega t)} \tag{2.30}$$

where K is the complex propagation constant for a wave propagating along z-axis and it

can be expressed by an equation similar to that of complex refractive index in equation 2.8

$$K = k + i\kappa \tag{2.31}$$

where k is the propagation constant vector, and κ indicates the extinction coefficient. So, equation 2.30 becomes

$$\vec{E}(z,t) = A_{\circ} e^{-\kappa z} e^{i(kz-\omega t)} \tag{2.32}$$

Since the energy transfer to a material is proportional to $|\ \mathrm{A}|^2$, intensity is related to $|\mathrm{A}|^2$, equation 2.32 can be rewritten

$$I = I_{\circ} e^{-\alpha_{\circ} z} \tag{2.33}$$

where the absorption coefficient is given by $\alpha_{\circ} = 2\kappa$. By inserting equation 2.30 into equation 2.29 and splitting real and imaginary components, one can get

$$k = \left[1 + \frac{1}{2}\chi^{(1)\prime}\right]\frac{\omega}{c} \tag{2.34}$$

$$\alpha_{\circ} = \frac{\omega}{2c}\chi^{(1)\prime\prime} \tag{2.35}$$

where

$$\chi^{(1)} = \chi^{(1)\prime} + i\chi^{(1)\prime\prime} \tag{2.36}$$

Where $\chi^{(1)\prime}$ is the real part of the nonlinear susceptibility, and $\chi^{(1)\prime\prime}$ is the imaginary part. The real part of the propagation constant K contains the refractive index while the imaginary part indicates the attenuation and includes the absorption coefficient, $\alpha_{\circ}$.

2.3.2 Optical dispersion

When a fs–pulse propagates through a dispersive media, it undergoes a chirp. In our experiments, the beam propagates through a series of dispersive media. Thus, the pulse duration at the sample is longer than the output of the laser by factor of two. Dispersion is the phenomenon in which the group velocity depends on the optical frequency. It can also be understood by the change in the medium refractive index with the frequency of light. The dispersion is described by the Taylor expansion of the propagation constant, $K(\omega)$, about its central frequency, $\omega_\circ$ in the following equation:

$$K(\omega) = K_\circ + \frac{\partial K}{\partial \omega}(\omega - \omega_\circ) + \frac{1}{2}\frac{\partial^2 K}{\partial \omega^2}(\omega - \omega_\circ)^2 + \frac{1}{6}\frac{\partial^3 K}{\partial \omega^3}(\omega - \omega_\circ)^3 + ... \tag{2.37}$$

where

$$\frac{\partial K}{\partial \omega} = \frac{1}{c}\left[n + \omega\frac{dn}{d\omega}\right] = \frac{1}{v_g} \tag{2.38}$$

$$\frac{\partial^2 K}{\partial \omega^2} = \frac{\lambda^3}{2\pi c^2}\frac{d^2 n}{d\lambda^2} \tag{2.39}$$

$$\frac{\partial^3 K}{\partial \omega^3} = -\frac{\lambda^4}{(2\pi)^2 c^3}\left[\lambda\frac{d^3 n}{d\lambda^3} + 3\frac{d^2 n}{d\lambda^2}\right] \tag{2.40}$$

The terms in equation 2.37 have the following meanings: the zero order contains the phase shift, and the first order describes the group velocity. The second and the third orders indicate the second and third order group velocity dispersion (GVD), respectively. The group velocity dispersion leads to spectral chirp and stretches the laser pulse. The duration of a Gaussian pulse after propagating through dispersive medium is given by,

$$\tau = \tau_\circ\sqrt{1 + \left(\frac{GDD}{\tau_\circ^2}4ln2\right)^2} \tag{2.41}$$

where $\tau_\circ$ is the full width at half maximum duration of the incident pulses and GDD is the group velocity dispersion for the total length of the medium. In the experiments related to this thesis, the chirp caused by the optical components in the beam path was taken into account, as will be discussed in the chapter 3

2.3.3 Nonlinear propagation

For stronger external fields, the frequency of incident light changes by propagating through the transparent media. Also, properties of the material become dependent on the field strength. So, the use of equation 2.29 is inadequate to describe the propagation of intense laser pulses through transparent materials. Thus, the nonlinear optical response is described by expanding the polarization as a power series of applied electric field [47]

$$\vec{P}(r,t) = \epsilon_\circ \left[\chi^{(1)}\vec{E} + \chi^{(2)}\vec{E}\vec{E} + \chi^{(3)}\vec{E}\vec{E}\vec{E} + ... \right] = \left[\vec{P}^{(1)} + \vec{P}^{(2)} + \vec{P}^{(3)} .... \right] \tag{2.42}$$

where $\vec{P}^{(n)}$ is the n^{th} order polarization that corresponds to n^{th}-rank tensor susceptibility ($\chi^{(n)}$). Amorphous solids, such as glass and most polymers, display inversion symmetry. Thus, χ^{2n} terms vanish in equation 2.42. The nature and the complexity of the nonlinear interaction is governed by the strength of the electric field. Each electric field in nonlinear terms can oscillate at a different frequency component that produces nonlinear polarization with new frequencies arising from the sum and/or difference of these components. For example, the second order nonlinear polarization contains two driving fields, E_1 with ω_1 and E_2 with ω_2. In isotropic media, for which that $\chi^{(2)}$ is a scalar, the nonlinear polarization consists of several frequency components, and it drives phenomena like second harmonic generation, sum and difference frequencies, and

optical rectification. Since all samples used in this thesis are polymers and glass, and since intensities are in the range of $10^{13} - 10^{14}$ W/cm^2, the occurrence of any mentioned phenomena is negligible. The third order nonlinear polarization contains three components for the electric field, E_1, E_2, and E_3 with frequencies of ω_1, ω_2, and ω_3. Hence, the interaction nature is more complicated and possible combination of optical frequencies drives different phenomena such as third harmonic generation, two photon absorption, and nonlinear refractive index.

2.3.4 Nonlinear refractive index

If the laser intensity is in the order of 10^{12} W/cm^2, the refractive index of a material changes with the laser intensity. The total refractive index can be expressed by

$$n = n_\circ + n_2 I \tag{2.43}$$

where n_2 is the nonlinear refractive index. The intensity I is related to the electric field by the following equation:

$$I = \frac{1}{2}\epsilon_\circ c n_\circ \mid E \mid^2 \tag{2.44}$$

The response of any transparent dielectric to the applied electric field is described by equation 2.42. This complicated response can be simplified for materials that display inversion symmetry. The focus here is on the interaction of fs-laser pulses with transparent dielectrics, particularly glass and polymers such as Polydimethylsiloxane (PDMS), Polymethyl methacrylate (PMMA) and Polystyrene (PS). Such materials are considered to be isotropic and centrosymmetric. Thus, the terms that have even exponents will be dropped and the tensor nature in equation 2.42 can be neglected. For an intensity

regime, limited to the occurrence of the third order nonlinearity, the polarization is given by,

$$P = \epsilon_{\circ}\left[\chi^{(1)} + \frac{3}{4}\chi^{(3)} \mid E \mid^2\right]E \tag{2.45}$$

Inserting equation 2.45 in the wave equation 2.27 leads to the expression for refractive index,

$$n = \sqrt{1 + \chi^{(1)} + \frac{3}{4}\chi^{(3)} \mid E \mid^2} \tag{2.46}$$

By squaring equations 2.43 and 2.46, the nonlinear refractive index n_2 is related to the third nonlinear susceptibility χ^3 by

$$n_2 = \frac{3\chi^{(3)}}{4c\epsilon_{\circ}n_{\circ}^2} \tag{2.47}$$

The nonlinear refractive index described by equations 2.43 and 2.47 is a constant that expresses the rate at which the refractive index changes as the laser intensity (I) increases. Occurrence of the nonlinear refractive index gives rise to other nonlinear phenomena such as self-focusing and self-phase modulation that will be briefly discussed in next following two sections.

2.3.5 Self-focusing

Self-focusing is the process in which a laser beam is forced to come to a focus when it propagates through a transparent material [47]. The self-focusing process is induced by the change in the refractive index when the material is exposed to an intense laser beam. For a Gaussian beam, the spatial variation in the intensity of the pulse is translated to a variation in the refractive index. By assuming a positive value of n_2, the refractive index of the medium increases by increasing the laser intensity. Therefore, the refractive

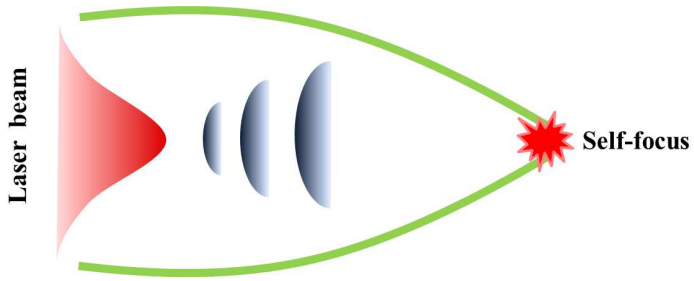

Figure 2.5: Schematic diagram of the self-focusing phenomenon.

index is higher in the centre compared to the index at the margins. This mismatch in the refractive index acts as a focusing lens for the beam. Although the occurrence of self-focusing depends on the laser intensity, its strength depends on peak power. The critical power p_{cr} after which the self-focusing phenomenon occurs is given by

$$p_{cr} = \frac{\pi(0.61)^2\lambda_\circ^2}{8n_\circ n_2} \tag{2.48}$$

where $\lambda_\circ$ is the central wavelength of the laser beam. Once the laser power exceeds p_{cr} , the self-focusing process occurs. When the power of the beam is $p \gg p_{cr}$, a catastrophic breakup takes place. The p_{cr} of the PDMS corresponds to an intensity of $\sim 5{\times}10^{13}$ W/cm^2. This value is estimated based on our measurements of the nonlinear refractive index, n_2 in PDMS using Z-scan technique.

Besides the spatial variation of the refractive index that leads to self-focusing, the temporal dependence drives an analogous process termed "self-phase modulation".

2.3.6 Self-phase modulation

The self-phase modulation means the change in the phase of the pulse during the propagation. The self-phase modulation process arises from the variation of the nonlinear refractive index with the time of the laser pulse. The dependence of the pulse intensity

on the time is translated to a dependence of nonlinear refractive index on the time that gives rise to a time dependent phase shift of the pulse. This phenomenon can also be

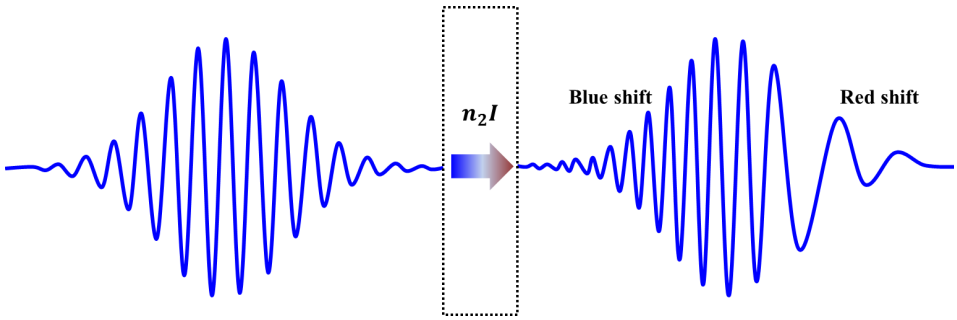

Figure 2.6: Schematic diagram of the self-phase modulation and its effect on the spectral content. The electric field is stretched at the leading edge of the pulse resulting in red shift and is compressed at the trailing edge leading to blue shift.

explained by the dependence of phase velocity on the intensity of the laser pulse. By assuming an instantaneous nonlinear response of a material in the absence of group velocity dispersion, the only effect of the medium is to change the phase. Assuming the propagation of the pulse [47] that has an electric field described by

$$\vec{E}(z,t) = \vec{A}(z,t)e^{i(kz-\omega_\circ t)} + c.c. \tag{2.49}$$

through a transparent medium is optically characterized by the nonlinear refractive index in equation 2.43. The change in the phase $\phi_{NL}(t)$ of the transmitted light is given by,

$$\phi_{NL}(t) = -n_2 I(t)\omega_\circ L/c \tag{2.50}$$

The time-varying phase of the wave modifies the spectrum of the transmitted pulse, and it becomes broader than that of the incident pulse. The temporal peak of the pulse corresponds to a refractive index higher than those leading and trailing edges do. Hence, the electric field is stretched at the leading edge, exhibiting spectral red shift, and is

compressed toward the trailing edge, producing a spectral blue shift, as shown in figure 2.6. The spectral content is described by defining the instantaneous frequency $\omega(t)$ that is given by

$$\omega(t) = \omega_\circ + \delta\omega(t) \tag{2.51}$$

where $\omega_\circ$ is the essential frequency and $\delta\omega(t)$ is the change in the frequency due to time dependence of the phase. For a Gaussian beam for which the intensity is expressed by [47],

$$I(t) = I_\circ sech^2(t/\tau_\circ) \tag{2.52}$$

the nonlinear phase shift in equation 2.50 becomes

$$\phi_{NL}(t) = -n_2 \frac{\omega_\circ}{c} L I_\circ sech^2(t/\tau_\circ) \tag{2.53}$$

and the change in the instantaneous frequency can be written as such

$$\delta\omega(t) = \frac{\partial\phi_{NL}}{\partial t} = 2n_2 \frac{\omega_\circ}{c\tau_\circ} L I_\circ sech^2(t/\tau_\circ) tanh(t/\tau_\circ) \tag{2.54}$$

where $\tau_\circ$ is the pulse duration, and L is the thickness of the medium. Assuming a positive n_2, the instantaneous frequency is shifted toward lower frequencies for the leading edge and is shifted toward higher frequencies for the trailing edge.

The self-action effects of the fs-laser pulse in transparent dielectrics and polymers plays a negative role in material processing. Since most of the work related to this thesis was carried out in the bulk, self-action effects should be taken into account. In the self–focusing nonlinear process, as the beam radius is reduced, the intensity becomes higher. Occurrence of self-focusing makes the intensity unpredictable in the

focus. Further increase in the laser intensity leads to filamentation. The consequence of the filamentation is to make the focus longer than usual. Thus, the fs–laser processing of polymers is undesirable in this regime. The occurrence of self-phase modulation leads to a chirp in the pulse duration. This makes the pulse duration unpredictable at the focus. Self–focusing and self-phase modulation are spatial and temporal effects on the pulse. So, they are present together all the time.

In the work related to this thesis, there are two factors that limit the occurrence of self-action phenomena, depletion of the pulse by nonlinear absorption, and the thickness. Depletion of the laser pulse is due to the fact that the number of atoms in the interaction region, for any transparent solid, is higher than the number of photons. This drives strong nonlinear absorption, and hence high efficiency of ionization. Thus, intensities that are required for nonlinear absorption can be reached without exceeding the threshold of self-focusing. For example, the critical power for silica glass is $\sim$ 2.5 MW, corresponding to an intensity of 2.9×10^{13} W/cm^2 for a pulse energy of 175 nJ, duration of 70 fs, spot size of and 1.65 μm. However, our results show that the ionization threshold for silica glass is $\sim$ 85 nJ, which is much less the self-focusing threshold. When intensity in the focus becomes high enough for multiphoton ionization, absorption occurs with high probability because of the high density of the material. Subsequently, the laser pulse gets depleted and the intensity is clamped along the focus [48].

In addition to the pulse depletion by the nonlinear absorption, the sample thickness plays a major role. In the work related to this thesis, the depth of of the focus inside the sample is between 50–800 μm. So, this short medium is not long enough for self-focusing phenomena to occur [48]. Based on the previous argument, glassy and polymeric materials can be ionized, which entails that they can be modified, before the occurrence

of self-focusing phenomena.

To summarize, this chapter has been divided into three main parts. The first part explored the nonlinear absorption and ionization of fs–laser pulses in transparent dielectrics, plasma formation, and energy dissipation via the electron lattice coupling. In the second part, nature and types of damage that could occur in the dielectrics were discussed. The effects of certain laser parameters like the pulse duration and repetition rate were also explained. The third part of this chapter outlined some linear and nonlinear propagation effects such as optical dispersion, self-focusing and self-phase modulation. In the following chapter we will discuss the experimental procedures used in this thesis.

Chapter 3

Experimental methods

This chapter gives a broad overview of the experimental methods used in this thesis. It includes a brief discussion about laser systems, materials, setup of experiments, and characterization techniques. It discusses the details that are not discussed in the following chapters. This chapter also presents the common experimental procedures among the following chapters in order to avoid any repetition though each chapter contains the necessary details. Although chapters from 4 to 7 are published/accepted papers, and they were written to be stand alone chapters, this chapter provides a general overview of the methods and techniques used and is therefore integral to the thesis as a whole.

3.1 Laser system

A regenerative amplifier that operates at 1 KHz and produces 40 fs pulses with an 800 nm wavelength was used in all experiments related to this thesis. The laser system consists of the Tsunami Ti:sapphire oscillator (*Spectra-Physics*) that is capable of producing pulses of $\sim$ 30 fs with pulse energy of $\sim$ 5 nJ at a wavelength of 800 nm and repetition rate of

76 MHz. The incoming seed pulses from the oscillator are amplified by the Spitfirepro regenerative amplifier (*Spectra-Physics*). The process of power amplification involves stretching the incoming pulses using a combination of multi-pass grating and mirrors to avoid any damage to the crystal. The selected stretched pulses then pass through the regenerative amplifier cavity multiple times, and are then recompressed by a grating compressor close to the original duration. The amplifier is capable of producing pulses of 40 fs and operates at a repetition rate of 1 KHz with a maximum pulse energy of 2.5 mJ.

3.2 Materials

3.2.1 Dielectric samples

A variety of dielectric transparent materials, with different sizes (100 to 250 mm^2) and thicknesses (1 to 3 mm), were used in the experiments presented in this thesis. These materials included poly methyl methacrylate (PMMA), polydimethylsiloxane (PDMS), polystyrene (PS), polycarbonate (PC), BK7, and fused silica. Commercial CQ grade PMMA, PS, and PC were purchased from *Goodfellow*. The BK7, and fused silica were supplied by *Fisher*, and *Hoya*, respectively. As for PDMS samples, they were prepared in the lab.

The PDMS samples were prepared by mixing a Dow Corning Sylgard 184 silicone elastomer base with a curing agent in a 10:1 ratio. The PDMS mixture was stirred for 10 minutes and degassed by placing it in a vacuum desiccator for 30 minutes. To prepare thick samples, the mixture was then poured between four glass slides that were taped onto a silicon wafer that was cleaned by methanol. Another glass slide was used

to gently spread the PDMS mixture so as to avoid any air bubbles formation in the samples. A 500 g weight was positioned on top of the glass slide to ensure that the PDMS had flat top and bottom surfaces. The mixture was cured in the oven at 80°C for two hours. Large sheets of $\sim$ 25 mm x 75 mm x1mm PDMS samples were prepared in this manner, and those sheets were subsequently cut into smaller samples of $\sim$ 10 mm x 10 mm x 1mm.

3.2.2 Biological samples

C2C12 mouse myoblast cells were cultured at 37° C and were incubated with 5% CO_2 in the Dulbecco's Modified Eagle Medium (DMEM), 10% Fetal Bovine Serum (FBS), and 1% streptomycin/penicillin (these materials were all from *Hyclone Laboratories Inc.*). Cells were seeded onto the substrates with a density of $\sim$ 2000 cells/cm^2. Immunofluorescence staining was carried out as follows: Mouse myoblasts cultured on PDMS substrates were fixed with 3.5% paraformaldehyde and permeabilized with 0.5% Triton X-100 for $\sim$ 5 minutes. The cells were then quenched in 0.15 M of Glycine for 25 minutes. Actin filaments were stained with Phalloidin Alexa Fluor 546 (Invitrogen), and the nuclei were stained with DAPI (Invitrogen). Moreover, vinculin (focal adhesions) was labelled with a mouse monoclonal anti-vinculin primary antibody (Invitrogen) and a rabbit anti-mouse IgG secondary antibody (Invitrogen) conjugated to Alexa Fluor 488 fluorophore (each used at a 1:200 dilution). For experiments using vinculin, actin filaments were stained with Phalloidin Alexa Fluor 546 (Invitrogen). Following each step, cells were incubated with a blocking buffer for 15 min (5% Horse Serum (Sigma)) in phosphate buffered saline (PBS) [49].

3.3 Experimental setup

The setup for this thesis project was designed for two types of experiments: The first type is directly related to ablation and modification of polymers. Three different experiments were performed using this setup: localized nanoclusters formation in PDMS by fs-laser pulses (chapter 5), high density data storage device recorded bit by bit by fs-laser pulses (chapter 6), and selective cell growth on a fs-microstructured PDMS surface (chapter 7). The second type of experiments is related to transmission measurements when the fs-laser pulse is focused inside polymers. This transmission experiment consists of two parts. The first part is related to the study of nonlinear absorption, which is discussed in chapter 4. The second part involves knife edge measurements of the spot size for all microscope objectives used in this thesis. The schematic of beam delivery and the experimental setup, for both types, is shown in figure 3.1.

Prior to each experiment, the sample was gently cleaned with air and methanol. The sample was then mounted on a glass slide that is attached to XYZ stages. The laser output from the amplifier has maximum power of 2.5 W, a wavelength of 800 nm, and a pulse duration of 45 fs. About 4% of the incoming beam was reflected by the beam sampler and directed to autocorrelation system to measure the pulse duration. The remaining part ($\sim$ 96%) of the beam was directed to the sample through a combination of half wave plate and a polarizer to control the power. The half wave plate was mounted on a rotation stage (PR50CC, Newport) that was connected to the computer and had a resolution of 0.02°.

Right before the microscope objective the beam was divided into two parts using a glass slide that was mounted 45° to the incident laser beam. The reflected part was directed to the fast photodiode (PD1) after passing through a series of ND filters to avoid

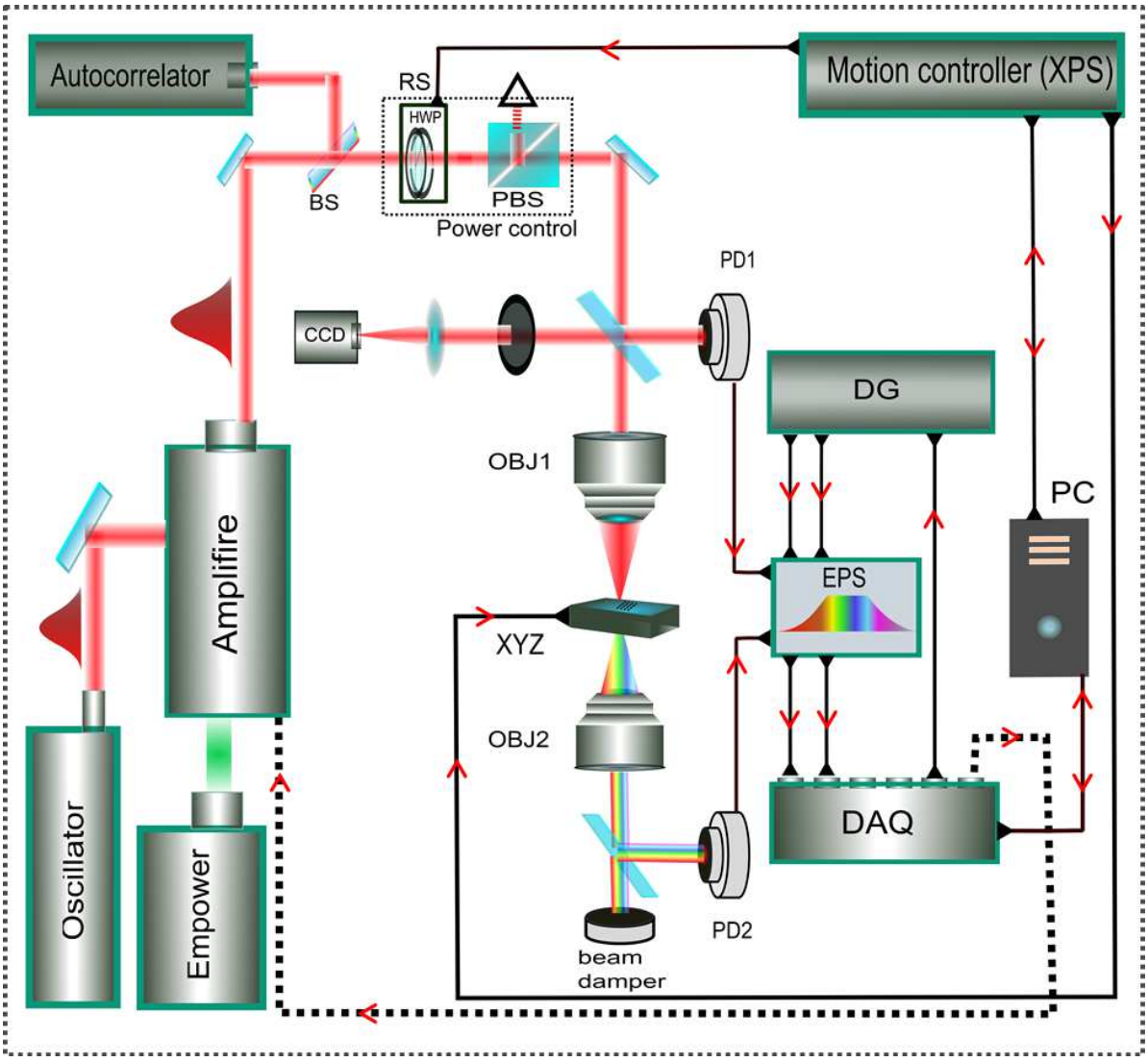

Figure 3.1: Schematic of experimental setup. BS = Beam Splitter, PBS = polarizer, HWP = Half Waveplate, OBJ = microscope objective, PD = Photodiode, DG = Delay Generator, DAQ= Data Acquisition card, and EPS = Electronic Pulse Stretcher, and XPS = motion controller.

any damage. This photodiode was used to monitor the power of the laser. The remaining part of the beam went to the sample after it was focused by a microscope objective (OBJ1). The reflected light from the surface of the sample was utilized to accurately determine the location of the laser focus relative to the surface. For this purpose, a pulse with an energy below the modification threshold was used. The reflected light from the surface of the sample was collected by the microscope objective, directed by the bottom surface of the glass slide, and focused by a lens onto a CCD camera(Mightex-SCE-BG04-U). The image of the surface appears as two dots on the screen. As the focus got closer to the surface the two dots got smaller and brighter.

The beam was focused either on the surface or inside the bulk using a 0.25 NA and 0.50 NA aspheric microscope objectives. To minimize the alignment errors, the back aperture of the microscope objectives was slightly overfilled with the beam that had a diameter of 12 mm at $1/e^2$. In this thesis, both single-pulse and multiple-pulse experiments were conducted and the writing of continuous lines was carried out either on the surface or inside the bulk.

As for the continuous line experiments, the sample was moved at a constant speed so that a specific number of laser pulses are present within the focal region. In these experiments, the laser produces pulses in a continuous mode with a repetition rate of 1 KHz. The translation stages (XMS50, XMS50, and VP-25XA, Newport) have a resolution of 50 nm along the lateral dimensions (X, Y) and 100 nm along the axial direction (Z). The stages were connected to the motion controller (XPS-C8, Newport) that was interfaced with Labview software and was programmed to choose specific patterns and laser parameters. Experiments that were performed using direct line writing are discussed in chapter 5 and 7.

Shot-by-shot experiments were performed using the same setup as the one shown in figure3.1, with the laser operating in the gated mode. Two types of experiments were carried out using the shot-by-shot setup: study of the nonlinear absorption of a fs-laser pulses in polymers, and the fabrication of a high density data storage device in plastics.

In the data storage device experiment where images were imprinted in the material, they were first spatially filtered to remove any artifacts. The data was encoded in the sample pixel by pixel, by moving the stages after every single pulse. Each picture was down-sized to a printable resolution. Utilizing histogram equalization, each image was divided into the desired number of grey levels as determined by its intensity distribution. To speed up the printing process and minimize wear on the translation stages, pixels with identical value were grouped into particles for which an individual map of coordinates was generated. Storing data was achieved by scaling the energy range of the laser pulses to the corresponding grey level. The experiment was completely motorized with a LABVIEW interface that was written for this purpose. The LABVIEW program was designed to encode data with the highest grey level first and then move to the second lowest level, and so on.

In the experiment of nonlinear absorption, the laser pulse was focused inside the material using a 0.25 NA microscope objective. The transmitted light was collected with the use of another microscope objective that had similar or higher numerical aperture. The second microscope objective was attached to the XYZ Positioning Stages in order to choose its position carefully so that it could collect all of the transmitted light. Both the incident and the transmitted light signals were collected by two avalanche photodiodes (APD120A2, Thorlab). Diffusers were attached to the photodiodes because of the small-active area they have. Diffuser changes the shape of the light distribution

from a Gaussian to a wide-top hat distribution. So, any problems due to alignment are eliminated. The transmitted signal was normalized to that of the incident pulse so that any fluctuation in the pulse energy was taken into consideration.

Triggering of the laser was achieved by using a data acquisition device (USB-6251, National Instrument) and the Timing Delay Generator (TDG) box. The desired number of pulses was controlled by the LABVIEW software, written for this purpose. Time between pulses in the cavity was determined by the repetition rate of the laser (1 KHz). However, in the gated mode the output of the laser could be a single pulse or multiple pulses with time intervals controlled by the time that is required to complete the motion of the translation and rotation stages. In the triggering mode, the signal initially came from channel 4 on the TDG box (not shown in figure 3.1) to the input of the data acquisition card. This signal was used as a reference for sending the triggering signal from the data acquisition card to the laser. The triggering signal was sent back to the enable-delay channel on the TDG . The time duration of the triggering signal was used to choose the number of pulses that are required for the experiment.

3.4 Parameters of the laser beam

3.4.1 Pulse duration

A fs-laser pulse that propagates through transparent media undergoes a chirp, which leads to a change in its duration. Such a change is due to the wide spectral width of ultrashort pulses and the group velocity dispersion of optical media [50]. Thus, dispersion needed to be taken into consideration during the experiment. The pulse duration was monitored by a single pulse autocorrelation system. A small portion (∼

4%) of the amplifier output was reflected by a thin beam sampler and was directed by optical mirrors to the autocorrelation system as shown in figure 3.1. The power was reduced insofar as it was possible to avoid any damage to the BBO crystal. The output of the amplifier had a pulse duration of 45 fs. There were several dispersive media that were used in all experiments, as shown in figure 3.1. The dispersive media in the beam path included a beam sampler (5 mm), a beam splitter (5 mm), a half wave plate (6.35 mm), a polarization cube(25.4 mm), Neutral Density filter ($\sim$ 1 mm), and a glass slide (1 mm). The beam splitters and the half waveplate are made of silica quartz while the polarization cube, ND filter, and the glass slide are made of BK7 glass. The group velocity dispersion (GVD) of the silica quartz and N-BK7 are 36.16 fs^2/mm, and 44.65 fs^2/mm, respectively [51]. The thickness and GVD were used to calculate the group delay dispersion (GDD) for each element. The pulse duration was stretched after passing through every single component. The pulse duration was calculated after each optical element using equation 2.41. By doing so, the effect of the previous optical component was considered in the successive calculation of the pulse duration. Before the microscope objective, the pulse duration was calculated to be $\sim$ 81 fs. However, $\sim$ 70 fs was measured by placing all components in front of the autocorrelator.

3.4.2 Power measurements

Measuring the laser power accurately is of high importance in femtosecond laser matter interaction and material processing experiments. In transparent dielectric materials, the thresholds of refractive index modification and ablation are highly dependent on the laser power. In the experiments for this thesis, the power was controlled by a combination of half wave plate and polarizer in addition to neutral density filters. The

wave plate was mounted in a motorized rotation stage (Newport, PR50CC) so that it was possible to control the power in fine increments. The average power measurements were achieved with a continuous wave power meter (407 A, Spectra-Physics), that was capable of measuring the power in the range of 1 mW to 30 W. The power was measured before the ND filter, which was placed before the microscope objectives. The power measurements were used to calibrate the photodiode (PD1) in order to monitor the power at low values. The PD1 was placed 90° to the beam direction as shown in figure 3.1. The pulse energy was calculated by dividing the average power by the repetition rate of the laser.

Because of the difficulty of directly measuring the power after the microscope objective, specific procedures were followed. First, the power was measured after passing through a small-scaled pinhole that mimicked the back aperture of the microscope objectives. Second, the loss of power caused by passing through the aspheric lens, which is $\sim 10\%$, was taken into consideration. Our results were compared with the theoretical value of a Gaussian beam passing through a small circular aperture, and all experimental measurements showed an agreement with the theoretical values. The total power in the beam at a radius of r is given by [21],

$$P = P_{\circ} exp\left(\frac{-2r^2}{w^2}\right) \tag{3.1}$$

if $r = w$, $P = P_{\circ}/e^2 \approx 0.865 P_{\circ}$, where $P_{\circ}$ is the total power in the laser beam before passing through the aperture, r is the radius of the aperture, w is the radius of the beam at $1/e^2$. The transmission of the aspheric objectives was 90% as specified by the manufacturer. The back aperture diameter of the objectives used were 5.5 mm for 0.25NA, and 8mm for 0.50NA. The $1/e^2$ beam diameter was 12mm.

3.4.3 Spot size and knife edge measurements

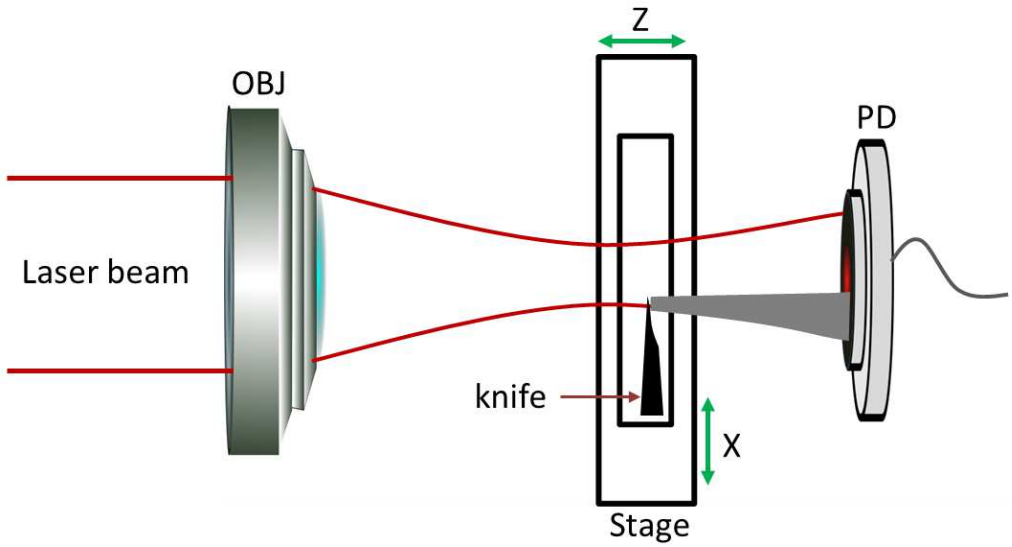

Figure 3.2: Schematic of the knife edge experiment. The shadow caused by the knife edge is represented by the grey colour [52].

Measuring the laser spot size is pivotal for the determination of the fluence in laser ablation/modification experiments. The spot size is defined to be the radius at which the power has fallen to $1/e^2$ of its peak value at the centre of the beam. The beam waist ($w(z)$) at any point along Z is given by [21],

$$w(z) = w_\circ \sqrt{1 + \left(\frac{M^2 \lambda z}{\pi w_\circ^2}\right)^2} \tag{3.2}$$

where $w_\circ$ is the smallest beam waist (spot size), which is obtained at z=0, λ is the wavelength, and M^2 is the quality factor for the Gaussian beam. The axial distance from the smallest beam waist to the point at which the beam waist is increased by a factor of $\sqrt{2}$ is called the Rayleigh length z_R, which is given by,

$$z_R = \frac{\pi w_\circ^2}{M^2 \lambda} \tag{3.3}$$

and thus, equation 3.2 becomes

$$w(z) = w_\circ \sqrt{1 + \left(\frac{z}{z_R}\right)^2} \tag{3.4}$$

In this thesis, the spot size was measured using the knife edge technique. In this technique, the beam is scanned spatially along X or Y, and the spot size is determined by measuring the transmitted power. To ensure accuracy, the transmission was collected after each fine move - 200 nm along X-axis. In addition, the spot size was also measured at fine increments (1 μm) along the Z-axis, before and after the focus. The spatial intensity of the Gaussian beam as a function of x and y is given by [53],

$$I(x,y) = \frac{2P_\circ}{\pi w^2} exp\left(-\frac{2x^2+2y^2}{w^2}\right) \tag{3.5}$$

The measured power on the photodiode decreases once the beam is interrupted by a knife edge moving in the X-direction as follows,

$$P(x) = P_\circ - \frac{2P_\circ}{\pi w^2}\int_{-\infty}^{x}\int_{-\infty}^{\infty} exp\left(-\frac{2x^2+2y^2}{w^2}\right)dxdy \tag{3.6}$$

from which the following equation can be derived

$$\frac{P(x)}{P_\circ} = erfc\left(\frac{\sqrt{2}x}{w}\right) \tag{3.7}$$

where $erfc$ is the complimentary error function, $P(x)$ is the measured power at a position x of the edge. The knife edge measurements were achieved by considering the standard setup of knife edge experiments as shown in figure 3.2. The laser was in the gated mode, and the transmitted power was measured for every single pulse. The beam was

scanned in the X direction with 200 nm increments and the transmission was measured after each move of the edge. The transmitted power is plotted as a function of the edge position along the X-axis as shown in figures 3.2(a) and 3.2(c). By assuming a Gaussian laser intensity, the data is fitted to equation (3.7), indicated by red lines. The spot size is calculated by considering $w_\circ$ to be a free parameter. A long distance was covered along X-axis direction to ensure full transmission when the edge was far from the beam as well as zero transmission when the beam was completely blocked. The sectioning along X-axis was repeated at different positions along Z-axis. The slicing of Z-axis was performed with an increment of 1 μm. The spot size was plotted as a function of the axial distance (Z) as shown in figures 3.2(b,d). The smallest spot size was obtained by fitting the data to equation (3.2). The spot sizes were measured to be 1.65 μm for 0.25 NA and 1.28 μm for 0.50 NA. The value of M^2 is 1.3 as it was given by the manufacture.

3.5 Characterization techniques

The laser-modified regions were characterized by several characterization techniques such as the Scanning Electron Microscope (SEM), Energy Dispersive Spectroscopy (EDS), X-ray photoelectron spectroscopy (XPS), Confocal microscopy, Raman spectroscopy, UV-Visible spectroscopy, emission and excitation spectroscopy, and contact angle measurements. In this section, an overview of each technique is provided.

3.5.1 Scanning electron microscope (SEM)

The morphology of femtosecond laser-modified/ablated regions were characterized using an SEM (JSM-7500F-JOEL). Because polymers are insulator materials, following procedures were followed to avoid any charging effect. First, samples were coated with

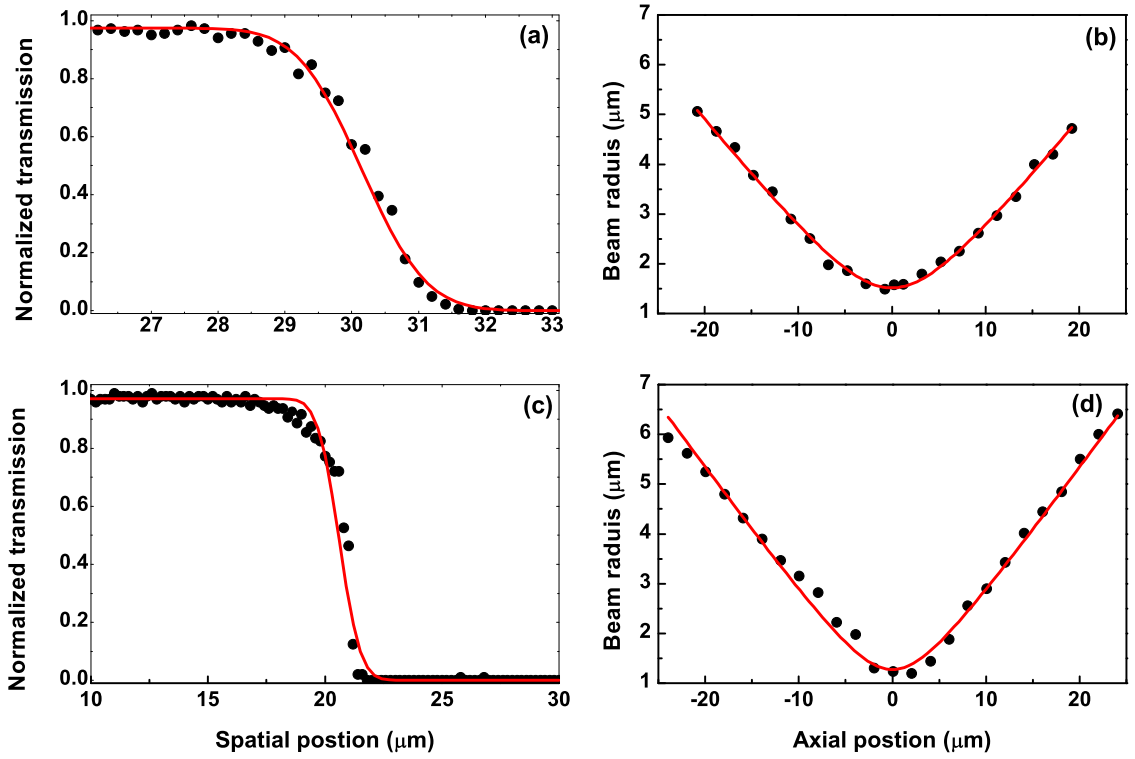

Figure 3.3: Translated knife edge positions along the X-direction and spot size along the Z-axis. The transmission is plotted as a function of the spatial edge position (X) for 0.25NA (a) and 0.50NA (b) microscope objectives. The spot size is plotted as a function of the axial direction (Z). The red lines are the theoretical fit to equation 3.7 (graphs a and c) and equation 3.3 (graph b and d). Data were fitted with reduced χ^2=0.007 (0.3) and R^2=0.99 (0.98) for 0.25 NA (0.50 NA) microscope objective. M^2 =1.3. Back aperture was 5 mm (8 mm) for 0.25 NA (0.50 NA).

a thin layer of gold to ensure that the surface was conductive and to allow the charge to dissipate on the surface. Second, sides were also coated with black carbon paint to ensure that there would be no accumulation of charges on the surface. Moreover, all pictures were taken at a low accelerating voltage (2 KeV). All measurements were carried out at the Centre for Catalysis Research and Innovation (CCRI) at the University of Ottawa - for both the SEM and EDS.

3.5.2 Energy dispersive spectroscopy (EDS)

The EDS device is in conjunction with the SEM. The EDS measurements were taken to compare the elemental compositions of the laser-modified regions and the unmodified ones. In EDS, a high energy electron beam strikes the sample and ejects electrons from the inner core shells like K_α. X-ray is generated with energy that equals the difference between the two levels when the atom returns to its ground state. The released X-ray hits the detector which converts it to a charge pulse. Then, the charge pulse is converted into a voltage signal with an amplitude corresponding to the energy of the detected X-ray [54].

3.5.3 X-ray photoelectron spectroscopy (XPS)

XPS is another technique that was used to chemically analyze the laser-modified regions by comparing them to the virgin spots. XPS is a quantitative analysis technique that gives information about compositions and chemical states of constituents that exist within a few nanometres below the surface of solid materials [55]. In XPS, photons with high energy from an X-ray source eject an electron from core shells of the atom, and the kinetic energy of an electron is measured simultaneously. The kinetic energy (E_{kin}) is related to the binding energy (E_{bin}) of the core electrons and the work function (ϕ) of the material according to the following equation:

$$E_{bin} = E_{ph} - (E_{kin} - \phi) \tag{3.8}$$

Where E_{ph} is the photon energy. For the XPS measurements, large areas of 1.2 mm $\times$ 1.2 mm were fabricated on the surface of the samples because the size of the beam tip

was $\sim$ 300 mum $\times$ 700 mum. XPS measurements were performed at CCRI using the Kratos Analytical device, model Axis Ultra DLD.

3.5.4 Confocal microscopy

Laser confocal microscopy is an imaging technique in which the resolution and contrast is increased by means of a small spatial aperture. The aperture is placed at the confocal plane of the scanning lens to suppress any out-of-focus scattered light. In the confocal microscopy, coherent light emitted by the laser is focused in the sample to produce fluorescence. The fluorescence signal goes back to the detector. Axial and spatial resolutions of the confocal are governed by the confocal parameter of the microscope objective and the diffraction limit.

The confocal microscope was used as a reading system in the data storage device experiment. After the data writing process, fluorescence from the laser-modified regions was recorded using the Nikon A1RMPST confocal fluorescence microscope. The beam was focused on the modified regions with a water immersion microscope objective for which the numerical aperture was 1.1 NA and the magnification was 25X. In this experiment, two excitation wavelengths of 488 nm and 405 nm with emission windows in 500 – 550 nm and 425 – 475 nm range, respectively were used. The power of the CW read laser and sensitivity of the detector for 488 nm (405 nm) excitation were 100 μW and 82 V (200 μW and 142 V), respectively. A stack of 20 layers along the Z-axis for each picture was taken to obtain the full intensity projection. An Image J software was used to analyze the fluorescence signal from the modified regions.

The confocal microscope was also used to investigate selective cell growth on the laser-micro-structured surface of PDMS. Images were acquired using an A1R resonant

scanner confocal microscope with a 60X water objective lens (Nikon, Canada). Brightness and contrast settings were optimized to maximize fluorophore signal. For the purpose of obtaining full intensity projections, pictures were taken in increments of 1 μm along the Z-axis. For cell growth experiments, images were acquired every 24 hours up to 72 hrs using a phase contrast microscope (Nikon, Canada). All biological experiments, which included cell preparation, seeding on the samples and, and taking both phase-contrast and confocal pictures, were carried out at the Pelling's Lab in biophysics.

3.5.5 Micro-Raman spectroscopy

Micro-Raman spectroscopy is a spectroscopic technique that provides information about vibrational and rotational frequency modes of a molecule. It gives a spectroscopic fingerprint for each molecules. It is based on the inelastic scattering of a laser light, usually in the visible region, with the target molecule. Since the photon energy is not conserved in such a scattering, the frequency of absorbed photons by the sample is re-emitted with an up or down shift in comparison with the original frequency of the photon. Raman shift is given by,

$$\Delta\omega = (\frac{1}{\lambda_\circ} - \frac{1}{\lambda}) \tag{3.9}$$

where $\Delta\omega$ is the Raman shift, $\lambda_\circ$ is the excitation wavelength, and λ is the Raman spectrum wavelength. Micro-Raman and photoluminescence spectra were collected using the back-scattering geometry with laser light focussed on the modified regions of the sample to a 5 μm spot using 50X (0.42 NA) or 100X (0.80 NA) long-working distance objectives. The spectral resolution of the system was 1 cm^{-1} (FWHM) for micro-Raman and 0.1 nm for photoluminescence. To enhance the signal to noise ratio and to ensure

the signal was collected only from the modified region, several closely spaced lines were fabricated in the PDMS in 3D such that the cross section consisted of 20 laser modified regions within an area of$\sim$15 μm^2. Samples were cut and the measurements were carried out on the cross section of the lines. All experiments related to Raman spectroscopy were conducted in Dr. Desgreniers's lab at the University of Ottawa.

3.5.6 Contact angle measurements

Wettability of the laser modified regions was studied using contact angle measurements obtained by VCA-optima system. In this system, a precise camera captures a picture of the droplet, and the contact angle is measured by the VCA software. Large areas of 1.2 mm $\times$ 1.2 mm were fabricated on the PDMS surface with conditions that are identical to those of the lines that were fabricated to study cell adhesion. The water contact angle was measured on both, the pristine and laser modified regions five seconds after releasing a 0.2 μl droplet from the syringe. All wettability measurements were taken at the Chemical Engineering Department at the -University of Ottawa.

3.5.7 UV-visible spectroscopy

The UV-visible spectroscopy refers to the absorption spectroscopy in the visible and ultraviolet regions. Typically, the results give the relationship between the absorbance on the Y-axis and the wavelength on the X-axis. The absorbance is increased dramatically at a wavelength that corresponds to the band gap of a material. All measurements were carried out using the Cary 100 spectrophotometer (Varian Inc.). The UV-visible absorption spectra were recorded in the transmission mode with a resolution of 2 nm. For UV-visible measurements, and emission and excitation spectroscopic studies, grat-

ing like structures were fabricated 300 μm below the surface in PDMS and PMMA, in area of 3 mm $\times$3 mm and 2 mm $\times$4 mm with a pitch of 2 μm.

3.5.8 Emission and excitation spectroscopy

To study the fluorescence capability of the modified regions, the emission and excitation spectra were recorded using a spectrophotometer (Perkin Elmer, Model LS50). For both excitation and emission spectra, the whole visible spectral region was scanned with intervals of 30 nm. Both fluorescence and excitation spectra were recorded using a slit width of 15 nm and a spectral resolution of 1 nm . Water Raman was used to calibrate the spectrometer.

3.6 Fluorescence life time Imaging (FLIM)

FLIM is an imaging technique that produces an image according to the differences in the exponential decay rate of the fluorescence from target material. Images were recorded using a confocal fluorescence microscope (Microtime 200, PicoQuant) system equipped with a frequency doubled picosecond pulse diode laser (485 nm, 100 ps, 40 MHz, LDH-D-C-485, PicoQuant). The FLIM system was used with configuration explained in reference [56]. Microstructures were fabricated near the surface of PMMA at 250 nJ, scan speed of 1 mm/s using 0.25 NA objective. The sample was placed on top of a clean coverslip positioned onto an oil immersion TIR objective (100X, NA 1.45, Olympus, PLAPO) and a beam splitter (500dcxr, Chroma) was used to reflect the excitation light onto the objective after collimation by a fiber optic cable. The epifluorescence signal was passed through a 510 nm long pass filter (Chroma). The fluorescence intensity images and lifetime traces were recorded using a single-photon-counting module (τ-

SPAD-100, PicoQuant) and Time Correlated Single Photon Counting Module (TSCPC), and processed through SymPhoTime program (PicoQuant).

Chapter 4

Transmission based measurements of the nonlinear absorption in polymers

This chapter discusses the interaction of fs-laser pulses with polymers, using transmission measurements. The interaction of intense ultrashort laser pulses with wide bandgap materials is dominated by nonlinear absorption that can be measured by monitoring the transmission of incident pulse or a weak probe pulse. Transmission of incident pulses focused inside glass exhibit a gradual decline after nonlinear absorption sets in at a certain threshold laser fluence. In contrast, we demonstrate a step-function like self-limiting behaviour in transmission of incident pulses inside polymers, dropping abruptly to $\sim 20\%$ ($\sim 35\%$) in PDMS (PMMA) and remaining nearly constant beyond the threshold fluence. The self-limiting threshold, which decreases with the number of incident pulses, is also associated with the onset of blackening in polymers. By measuring the transmission of a probe pulse we show that the degree of blackening

increases with the number of pump laser pulses reaching a saturation where only ∼40% of the probe is transmitted. Spectroscopic characterization of laser irradiated polymers indicate a localized reduction in the band gap when compared with pristine polymers. We exploit laser-induced blackening to fabricate embedded micro-optical white light filters by varying the laser fluence and the number of modified layers.

4.1 Introduction

Nonlinear absorption is pivotal to intense light-matter interaction when photon energy is less than the bandgap of the material. It is initiated by generation of free carriers in dielectrics, when the incident laser pulse promotes a large fraction of electrons from valence to conduction band by multiphoton and/or avalanche ionization. Nonlinear absorption is a precursor to optical breakdown of a material. It enables controlled deposition of pulse energy leading to localized material modification - key to many applications of ultrafast lasers. Examples include, fabrication of embedded waveguides [12, 34, 57, 58], gratings [59–61], and microfluidic channels [62, 63] for integrated photonics, nano/microstructuring [64], multi-modal imaging in biophotonics [65], and laser surgery [66].

Nonlinear absorption exhibits a threshold behaviour and its onset is typically determined by monitoring structural changes to the material both on the surface and in the bulk using microscopy. The most popular technique to detect any structural change is the scanning electron microscope. This technique is valid for transparent dielectrics as well as opaque materials. Optical microscope is another technique, but it is suitable only for transparent dielectrics. In this technique, confocal geometry is used to detect any change in the refractive index. In these two techniques, the smallest detectable

damage/modification gives the fluence threshold. However, the nonlinear absorption threshold could be slightly less than the lowest fluence value [38].

White light generation due to self phase modulation can be used to monitor the nonlinear absorption threshold. However, white light generation mostly indicates self–focusing phenomena, and the white light generation threshold is an order of magnitude higher than the damage thresholds.

Alternately, a reduction in transmission of the incident or probe pulse as a function of pulse energy provides an accurate measure of the onset of nonlinear absorption [15]. The threshold for nonlinear absorption depends on the material bandgap and laser parameters such as laser wavelength and pulse duration. It also decreases with the increase in number of pulses incident on the material due to incubation affects.

In glasses, the nonlinear absorption threshold for a single pulse was determined by monitoring the drop in the transmission. Transmission of a single pulse incident on a fresh spot remained unaffected as the pulse energy was varied up to a certain threshold value and then decreased gradually with further increase in pulse energy. The pulse energy at which the transmission starts to drop corresponds to the nonlinear absorption/ionization threshold. With band gap in the range of 4-10 eV for most glasses, the threshold intensity was found to be in the range of 1–5$\times 10^{13}$ W/cm^2 [15, 67, 68] – often lower than the self-focusing or visible damage threshold.

Irradiation of the same spot in fused silica showed a reduction in the ionization threshold compared to that of the single pulse. A threshold intensity of 9.5×10^{12} W/cm^2 was reported compared to 1.2×10^{13} W/cm^2 for fresh fused silica spot. Irradiation of the same spot with pulses of different energies also revealed shot–to–shot memory in nonlinear ionization. As the pulse energy was ramped up and down the transmission

curve exhibited hysteresis above the ionization threshold while it recovered completely below the threshold. The observed memory in nonlinear ionization was due to a positive feedback induced from shot to shot while the material maintains its original transparent nature. This behaviour was attributed to the change in the optical band gap of the material with successive laser pulses [67]. The change in the bandgap could be due to either a structural rearrangement [69] or new phase of the material induced locally by the laser pulses [70–72].

In polymers, a similar change in the material bandgap was observed upon ion irradiation [73, 74] and was attributed to formation of carbonaceous clusters [75, 76]. Intense femtosecond laser pulse can also readily form such nanoclusters through localized chemical rearrangement of the polymer backbone [27]. The carbonization process, which is the formation of nanoclusters arising from inelastic sticky collisions between neutral atoms, an atom–cluster, and/or cluster–cluster [31], renders the material to appear darkened. Photo-blackening has been reported in transparent dielectric materials both in the nonlinear regime induced by a femtosecond laser [26, 77, 78] and in the linear regime irradiated with UV light [79] , ions [80] and electrons [81].

In this chapter, we show transmission of incident femtosecond pulses focused inside polymers to be significantly different from glass. We demonstrate a step-function like self-limiting behaviour in transmission which drops abruptly at the threshold fluence and remains constant there after. Unlike in glass, this process is irreversible leading to permanent change in the material properties. We show that the material undergoes blackening at the self-limiting threshold reducing the transmission of a probe pulse. The degree of blackening, defined as the loss in transmission of the probe pulse, increases with the number of pump laser pulses reaching a saturation. UV-visible spectroscopy of

laser irradiated polymers shows about two orders of magnitude difference in absorbance and a shift in the bandage with respect to the pristine polymers, suggesting a significant reduction in the bandgap. Exploiting laser-induced blackening we demonstrate fabrication of embedded micro-optical white light filters by varying the laser pulse energy and the number of modified layers.

Nonlinear absorption of femtosecond pulses was studied by collecting all the transmitted light from the sample with an aspheric objective onto a photodiode equipped with a top hat diffuser in the front to minimize signal fluctuations. We found this simple arrangement to provide similar results to using an integrating sphere. Transmission is measured on a shot-to-shot basis using a computer-controlled data acquisition system. The photodiode signals monitoring the incident and transmitted pulses were stretched in time and converted to a broad square pulses whose height was proportional to the input signal intensity. The stretched pulses were then sampled at a high rate and averaged to obtain the incident/transmitted signal. This arrangement ensured measurement accuracy.

4.2 Nonlinear absorption

Figure 4.1 shows transmission of femtosecond pulses as a function of laser fluence in three different transparent materials (a) SiO_2, (b), PDMS, and (c) PMMA. The pulse energy was increased from shot-to-shot in small increments up to a certain value and then decreased while irradiating the same spot inside the sample multiple times. The full energy cycle contained 17,000 (11,000) pulses for SiO_2 (PDMS and PMMA). In SiO_2, the transmission is close to unity until the onset of nonlinear absorption around 80 nJ. Beyond this threshold the transmission decreases gradually (black curve) with

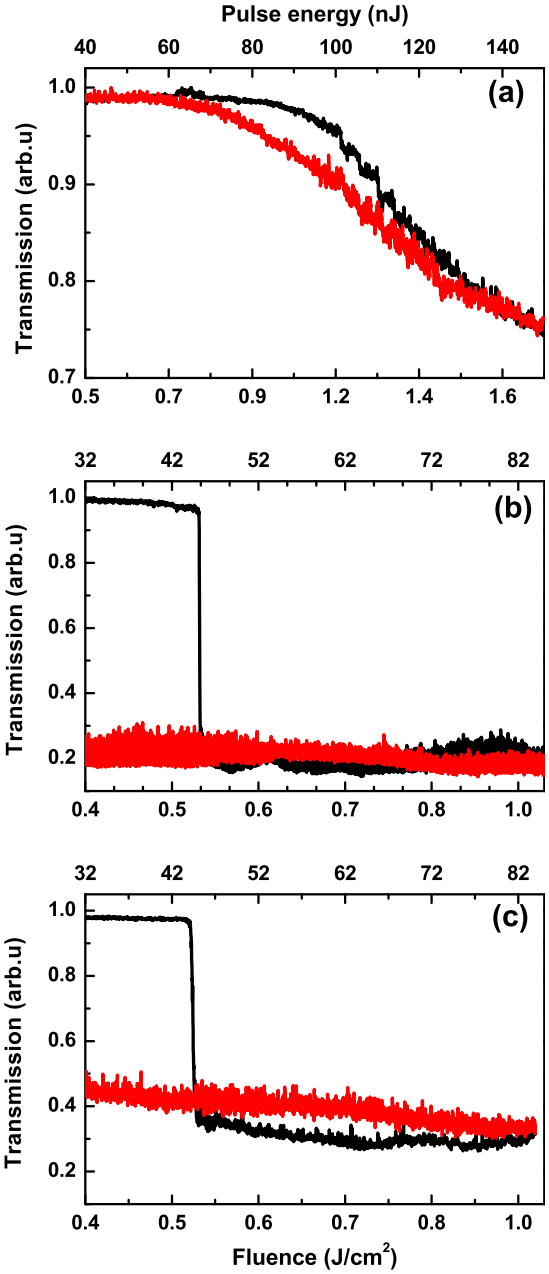

Figure 4.1: Nonlinear absorption inside (a) SiO_2, (b) PDMS, and (c)PMMA. Transmission is plotted as a function of pulse energy. The laser focus was stationary and the pulse energy was ramped up from shot to shot and then reduced. The full cycle contained 17,000 (11,000) pulses for SiO_2 (PDMS and PMMA). The black curve represents the first half of the energy cycle (low $\rightarrow$ high), while the red line denotes the second half (high $\rightarrow$ low). The energy scale is shown on top.

pulse energy to about 75% at 150 nJ. When the energy is gradually decreased without moving the laser focus the transmission (red curve) does not retrace the black curve and exhibits hysteresis. However, below the nonlinear absorption threshold the transmission recovers to its initial value suggesting no material damage. This behaviour has been attributed to memory in nonlinear ionization that eventually reduces the threshold energy $vis - a - vis$ material band gap leading to the well known incubation effect [67]. This well known behaviour of SiO_2 is used as a reference to highlight the differences observed in other materials presented in this chapter.

In contrast, transmission of femtosecond pulses in PDMS and PMMA (figure 4.1 (b,c)) is significantly different from that of SiO_2. First, at the onset of nonlinear absorption, the transmission abruptly plummets from unity to $\sim$ 20% (35%) in PDMS (PMMA). Second, the transmission curves do not exhibit hysterisis when the pulse energy is ramped up and down in a full cycle while irradiating the same spot. The transmission is clamped at $\sim$ 20% in PDMS irrespective of the pulse energy. In PMMA, the transmission is clamped at $\sim$35% when energy is increased and increases slightly as the energy is reduced. The abrupt drop and clamping of transmission above the nonlinear absorption threshold is indicative of a permanent change in the material induced by femtosecond pulses and reveals self-limiting behaviour of these materials. The self-limiting threshold depends on the pulse energy and the number of laser pulses in PDMS and PMMA.

Figure 4.2(a) shows transmission as a function of number of laser pulses irradiating the same spot for different pulse energies. The time delay between successive pulses is in seconds, necessitated by the need to measure transmission for every pulse. The number of laser pulses required to reach the self-limiting threshold is high for low pulse

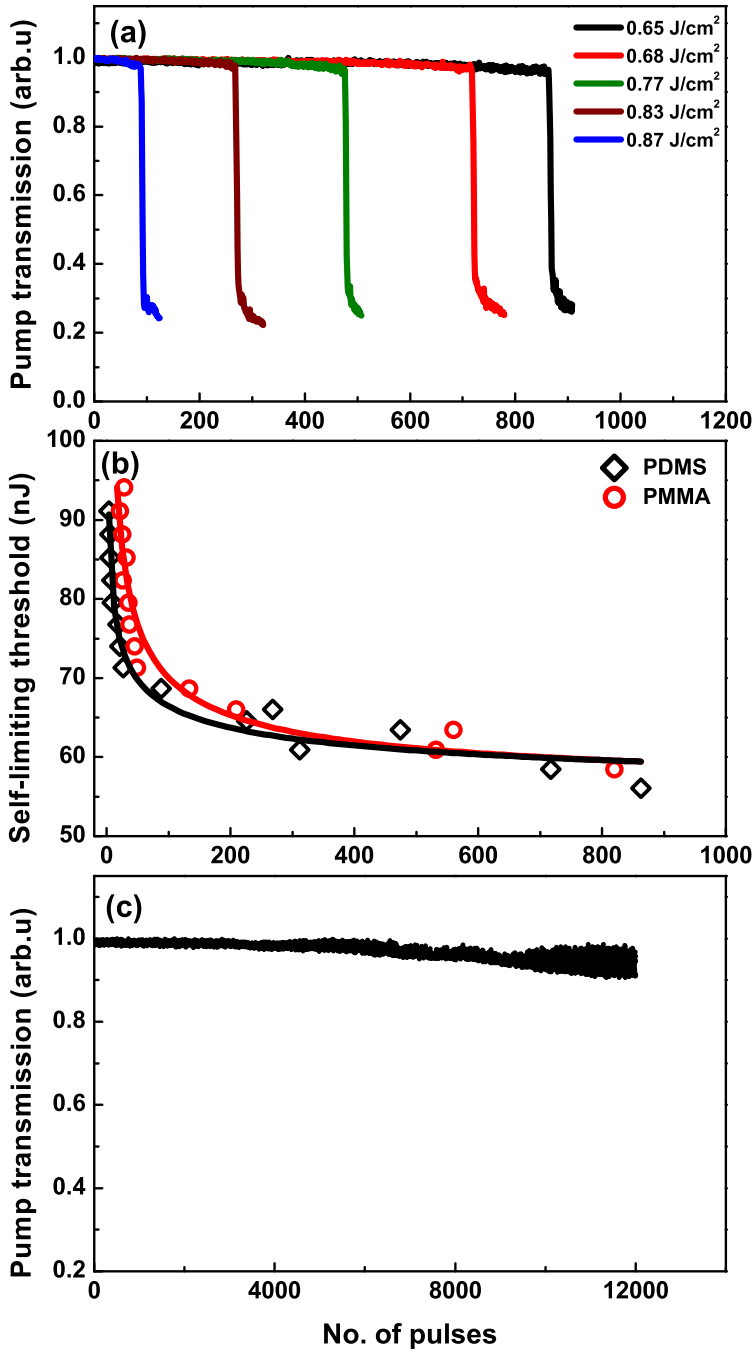

Figure 4.2: (a) Pump pulse transmission as a function of number of pulses in PDMS. (b) Self-limiting threshold, defined as the energy at which transmission decreases abruptly, as a function of number of pulses in PDMS and PMMA. Solid lines are theoretical fit to the data using the incubation model. (c) transmission of 10 nJ pulses suggesting they can be used as a probe because they do not modify material properties. The same spot was irradiated and the transmission was collected from shot to shot.

energies but decreases with increasing pulse energies. Figure 4.2(b) shows the self–limiting threshold, defined as the energy at which transmission decreases abruptly, as a function of number of laser pulses. The data is fitted to an incubation model [46] that was initially developed for laser ablation but could be extended to laser interactions inside the bulk. According to the model, the threshold fluence for N pulses is given by

$$F_{th}^{N} = F_{th}^{\infty} + \Delta F_{th}^{(1,\infty)} N^{S-1} \tag{4.1}$$

where $\Delta F_{th}^{(1,\infty)}$ is the difference between the fluence threshold for infinite number of laser pulses (F_{th}^{∞}) and that of a single laser pulse, and S is the incubation factor. We used single shot ablation thresholds of 1.4 J/cm^2 and 2.6 J/cm^2 for PDMS and PMMA, respectively [13, 38]. The thresholds for modification will be slightly lower. Solid lines in the figure represent fit to the experimental data for PDMS (black) and PMMA (red) giving F_{th}^{∞} and S values of 0.67 J/cm^2 (0.63 J/cm^2) and 0.58 (0.49) for PDMS (PMMA), respectively.

Results of figure 4.1 and figure 4.2 suggest that commonly available polymers can be used for optical limiting but the process is irreversible requiring to move the sample to expose fresh material to the incident radiation. In spite of this drawback, their step–like limiting behaviour can be an asset in ultrafast technologies. This is in contrast to conventional passive optical limiters that are reversible as they rely on the transient nature of nonlinear interaction of light with the material, such as absorption, refraction, scattering or phase transitions, which prevail on the time scale of electronic or thermal response of the medium [82–87].

4.3 Carbonization of polymers

Irradiation of polymers with ultrashort laser pulses leads to carbonization due to the formation of localized carbonaceous clusters [27, 88–91]. The presence of such clusters in the laser modified region can not only alter the transmission of the incident laser pulse but also transform the material from being transparent to translucent, exhibiting a degree of blackening. The extent to which laser-irradiated regions become opaque to incident light was studied by measuring the transmission of a weak probe pulse incident on the irradiated region at a later time (minutes after irradiation with pump pulses). Figure 4.2 (c) shows the transmission of a weak probe pulse ($\sim$ 10 nJ) at 800 nm as a function of number of pulses incident on the same irradiated spot suggesting the probe pulse has insufficient energy to alter material properties or cause any dielectric breakdown. Transmission of the probe was investigated by passing it through the modified regions irradiated by the pump pulse. Fresh material was irradiated as the pump energy was ramped up.

Figure 4.3(a) shows transmission of probe pulse as a function of pump energy for different number of pump pulses incident on the same spot in PMMA. The time delay between successive pulses is a millisecond, determined by the repetition rate of the laser. At low pump energies, transmission of the probe pulse remains close to unity in all cases but suddenly drops to 80% at $\sim$100 nJ for a single pulse irradiation and to 40% at 50 nJ for multiple pulses. Beyond these threshold energies the transmission of the probe pulse decreases marginally. Note that the time delay between successive laser pulses in figure 4.2(a) and figure 4.3(a) are different. As a result, for a given laser fluence the drop in transmission occurs for different number of laser pulses due to the dependence of incubation effect on time delay [46].

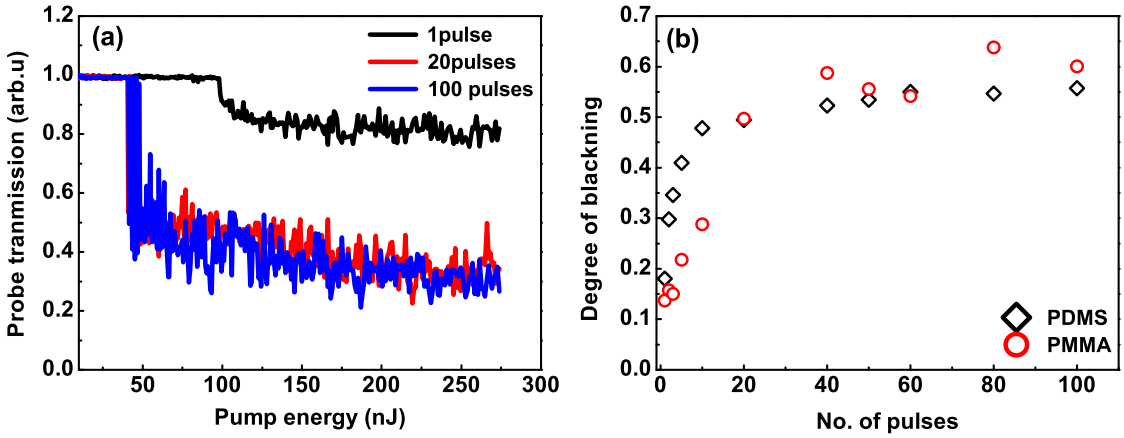

Figure 4.3: (a) Transmission of probe pulse through modified regions irradiated by pump pulses at different energies. Fresh material was irradiated every time the pump energy was varied. Probe transmission is shown for 1(black), 20 (red) and 100 (blue) pump pulses incident on the same spot in PMMA. Probe energy was 10nJ. (b) Degree of blackening as a function of number of pump pulses at an energy of 110 nJ for PDMS (black), and PMMA (red).

From the probe transmission data one can extract the degree of blackening, defined as the amount of probe absorption, at a specific pump pulse energy. This was obtained by normalizing the transmission of probe through the modified region with that of the pristine region and subtracting from unity. Figure 4.3(b) shows the degree of blackening as a function of number of pulses at 110 nJ of pump energy in PMMA and PDMS. The degree of blackening increases sharply with number of pulses in both materials and reaches a saturation after 20 - 30 pulses. The maximum amount of absorption of the probe pulse that can be achieved was $\sim 60\%$. These results suggest a change in the optical band gap of the fs-laser irradiated regions.

4.4 Reduction of the optical band gap

Figure 4.4(a) shows UV-visible-NIR absorption spectra recorded in the transmission mode for pristine and laser modified PDMS. To enable measurement of the absorp-

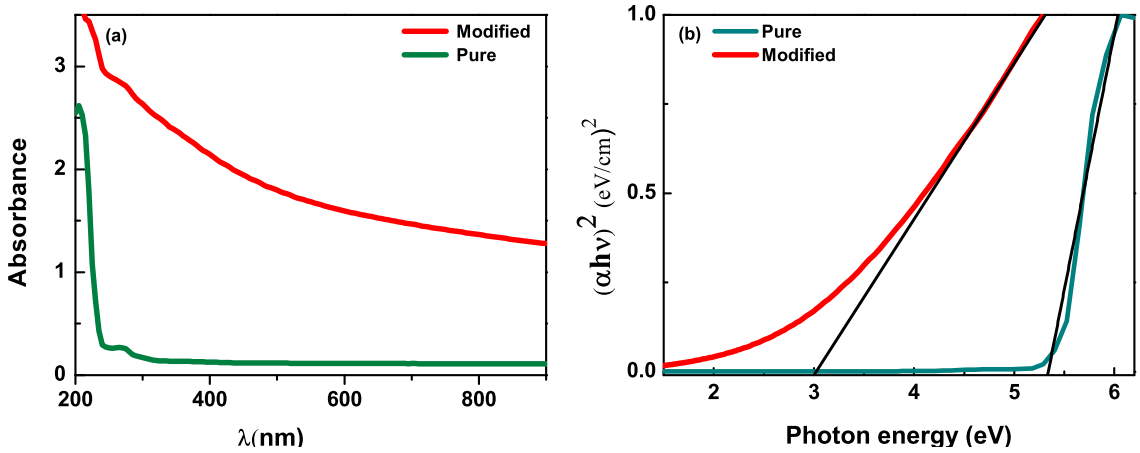

Figure 4.4: (a) Absorption spectrum of pristine (green), and laser modified (red) PDMS. (b) Tauc's plot showing normalized absorption coefficient as a function of photon energy for a direct band gap transition in pristine and laser modified PDMS.

tion spectrum a larger area of 3 mm x 3 mm was fabricated 300 μm below the surface consisting of 500 lines/mm, similar to the smaller modified regions of figure 4.5. Absorption spectra were recorded in the transmission mode with a resolution of 2 nm. The absorbance of the laser modified region increased significantly compared to that of the pristine PDMS. Predominantly higher absorbance of laser modified PDMS at shorter wavelengths could be due to Rayleigh scattering from nanometer sized carbonaceous and siliconaceous clusters formed upon irradiation [27].

UV-visible spectroscopy also provides information regarding variation in band-gap of a material after laser irradiation. Formation of carbonaceous clusters and the induced structural disorder affects the electronic structure. As a result, the optical absorption spectra of irradiated polymers are characterized by a shift in the optical absorption edges, which indicates a lowering of the energy gap. Close to the absorption edge, the band gap of a material is given by Tauc's relation [92],

$$\alpha h\nu = A(h\nu - E_g)^n \tag{4.2}$$

where α is the absorption coefficient, $h\nu$ is the photon energy, A is a scaling factor that describes band to band electronic transition rates, and E_g is the optical band gap of the material. In amorphous solids where no long range order exists only direct transitions are meaningful, so $n = 1/2$. This is because only energy of the electron involved in the optical transition needs to be conserved whereas in crystalline solids both energy and momentum needs to be conserved [73, 93, 94].

Figure 4.4(b) shows Tauc's plot for pristine and laser modified PDMS. The band gap was determined by plotting $(\alpha h\nu)^2$ versus hν and extrapolating the linear fit to intersect the abscissa. Band gap of 5.2 eV for pristine PDMS is in good agreement with published values [27, 95]. Tauc's plot for laser modified PDMS was obtained by subtracting the absorption spectrum of the pristine PDMS from that of the laser modified region since the 10 μm thick laser modified region was embedded in a 1mm thick PDMS sample. The band gap of the laser irradiated PDMS was $\sim$ 3 eV, about 40% reduction in comparison with pristine PDMS at an energy of 200 nJ. Similar reduction in band gap of materials upon femtosecond laser irradiation has been reported previously [67].

4.5 Embedded micro-optical filters

Results of figure 4.3 and figure 4.4(a) suggest the possibility of fabricating embedded micro-optical filters in polymers with varying degree of transmission over a wide range of wavelengths. Figure 4.5 shows a colour map of transmission of white light through an array of filters embedded 300 μm inside PDMS. Each 100 μm $\times$ 100 μm filter region consisted of 50 lines fabricated by moving the laser focus at a constant speed of 1 mm/s. A 2 μm line spacing ensured overlap of lines resulting in uniform modification. Each column in the array represents fixed pulse energy and writing speed while each row

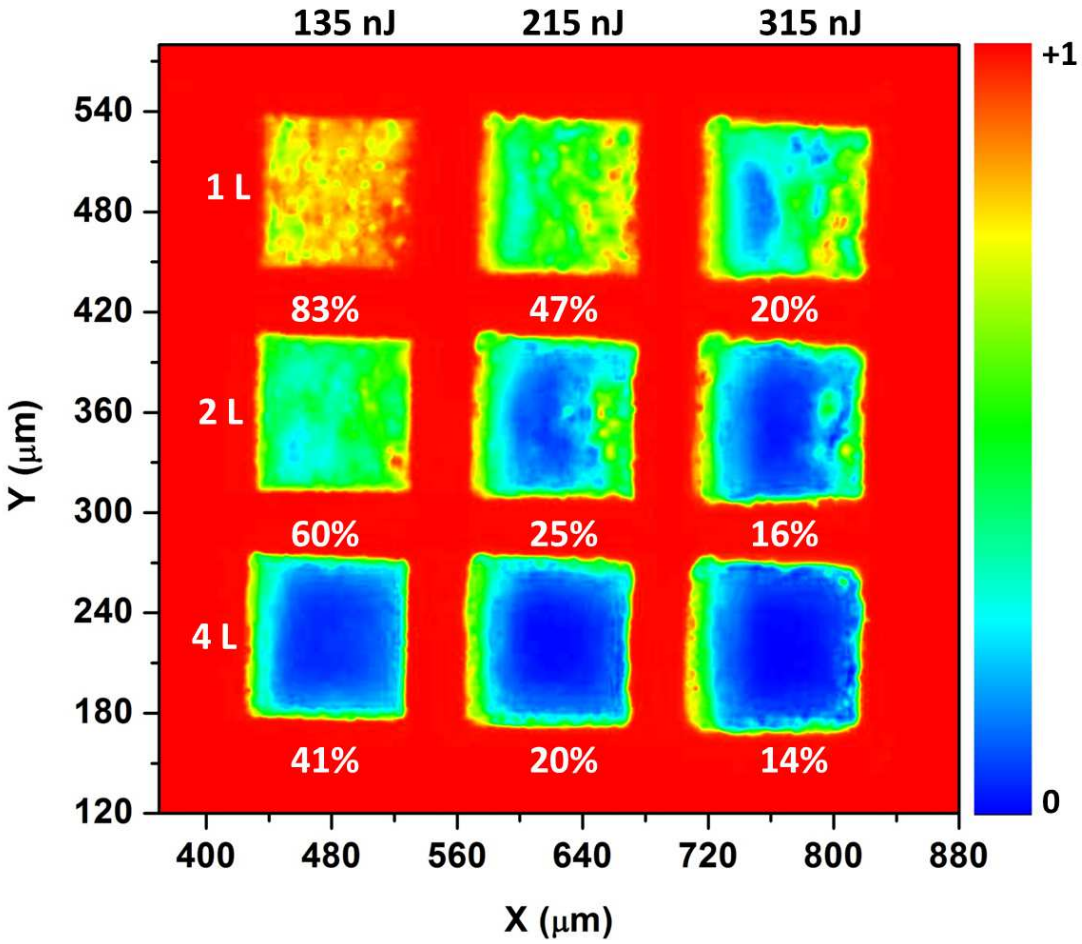

Figure 4.5: Colour map showing transmission of white light through an array of 100 μm x 100 μm laser modified regions embedded in PDMS. Columns correspond to different pulse energies (135, 215, 310 nJ) while rows correspond to the number of stacked (1,2, 4 layers). Numbers below each modified regions represent percentage of transmission.

represents number of layers stacked on top of each other with a spacing of 20 μm. The transmission of the white light through the modified regions is normalized to pristine PDMS. Red (Blue) colour represents the maximum (minimum) transmission denoted by 1(0). Number below each modified region represents the percentage of transmitted light. The transmission decreased with laser pulse energy and the number of stacked modified layers.

4.6 Conclusion

The self-limiting behaviour that we observed should be a characteristic of most polymers where nonlinear interaction of femtosecond pulses induces material modification by altering the polymer backbone. We demonstrate a steep drop in transmission of the incident pulses beyond a threshold fluence that depends on the number of laser pulses. We also show that the self-limiting behaviour is accompanied by laser induced blackening of the polymer that can be varied and utilized to fabricate embedded micro-optical white light filters. The observed phenomena can be associated to a reduction in the band gap of laser irradiated regions. Our results combined with laser induced refractive index modification pave way to new opportunities in the realm of embedded integrated photonics systems.

Chapter 5

Nanoclusters formation in PDMS upon irradiation with fs–pulses

This Chapter demonstrates formation of localized carbonaceous and siliconaceous clusters, confined to the modified region on a micron scale, when PDMS is irradiated by intense femtosecond pulses. Micro-Raman studies also suggest formation of quasi-crystalline silicon nanoclusters whose size varies with the incident laser fluence. The modified region produces broad photoluminescence whose intensity increases with laser fluence. We observed red-edge excitation effect in PDMS wherein the fluorescence from the laser modified region shifts to longer wavelengths as the excitation wavelength is increased to the red edge of the absorption band. Excitation spectra reveal four distinct absorption bands that contribute to the emission from the laser-modified region, two each ascribed to carbonaceous and siliconaceous clusters.

5.1 Introduction

Composites formed by embedding nanoclusters in metal, semiconductor and insulator matrices exhibit unique mechanical, optical, electrical and magnetic properties that can be tailored by varying the cluster size. Such nanostructured materials have potential applications in optoelectronics enabling efficient circuitry on nanometer dimensions [96], all optical switching in integrated optical devices due to enhanced nonlinear properties [97], charge storage [98], memory [96], strengthening of steel [99], spintronic devices due to large spin dependent transport and magneto-optical properties [100], biology [101] and green technologies like solar cells [102]. Nanoclusters are also of fundamental interest due to their quantum-size effect wherein the energy of optical transition depends on the cluster size. This effect in a matrix leads to photoluminescence of such clusters, which in some instances can be called as quantum dots. Nanoclusters are embedded in materials employing techniques such as ion implantation [2,103], RF co-sputtering [5,6], thermal decomposition of thin grown layers [7], sol-gel [8], ion-beam mixing [1], annealing of ion-exchanged glasses [104], electron beam irradiation [9], selective oxidization [10] and by depositing nanoparticles onto a surface and over growing the deposited area with additional matrix material [11]. Laser irradiation is known to alter optical properties of materials [12] and has also been employed to induce nanoclusters in dielectric materials.

Excimer lasers were used to form metal nanoclusters by photo-decomposition of organo-metallic crystals embedded in Poly(methyl methacrylate) [105]. The unique capability of ultrafast lasers to localize the interaction to micron dimensions was exploited to pattern functional microcrystals in 3D inside glass [106, 107] and to induce silver nanoparticle formation in silver containing glasses [108, 109] and polymers [110] by photoreduction and subsequent post baking. Si nanocrystals and amorphous Si clus-

ters [111] have also been shown to form when silicon-rich nitride films were treated with femtosecond laser. Several studies have also focused on laser induced transformation of nanoparticles embedded in matrices [112,113]. In almost all cases light interacted with matrices rich with specific atomic species leading to their precipitation into nanoclusters after post baking.

The mechanism by which the nanoclusters are formed depends on the extreme intensity of the fs-laser pulse at the focus. Such intensities are able to ionize, create a plasma, and break almost all bonds between atoms, within the interaction region. Nanoclusters are formed via rearrangement process due to the inelastic collisions between hot neutral atoms, atom-cluster, and cluster-cluster. The process of a nanocluster formation is fast, and it happens on a time scale of picoseconds [31]. The formation of nanoclusters that are localized within a micron scale inside the bulk can be utilized in data storage device, which was discussed in chapter 6.

This chapter discusses nanocluster formation by localized modification of the matrix structure itself. We show the formation of photoluminescent carbonaceous and siliconaceous nanoclusters within the laser modified region of a polymer after its backbone structure undergoes rearrangement. The clusters embedded in the polymer are characterized using energy dispersive X-ray spectroscopy, micro-Raman, UV-visible and fluorescence spectroscopy. Studies on surface irradiation of polymers, diamond-like carbon films and bulk silicon have demonstrated generation of carbon [114,115] and silicon clusters [116] in a laser ablation process. Although cluster formation mechanisms still remain unclear it is widely accepted that bond breaking occurs due to light-matter interaction resulting in formation of radicals that are active and act as cluster centres [117]. Similar underlying photochemical processes can be expected to occur when light inter-

acts with a bulk material in spite of its differences with surfaces. In fact, refractive index modification of fused silica by femtosecond lasers is associated with a rearrangement and subsequent reduction of SiO_2 ring structure. Moreover, extensive studies conducted on ion irradiation of polymers indicate structural rearrangement of the polymer backbone resulting in formation of carbonaceous clusters along the ion tracks [75, 79, 118]. However, the primary difference being ultrafast lasers enable spatial control of localized material modification in 3D and hence the nanocluster formation that can be randomly distributed within the modified region.

5.2 EDS measurements

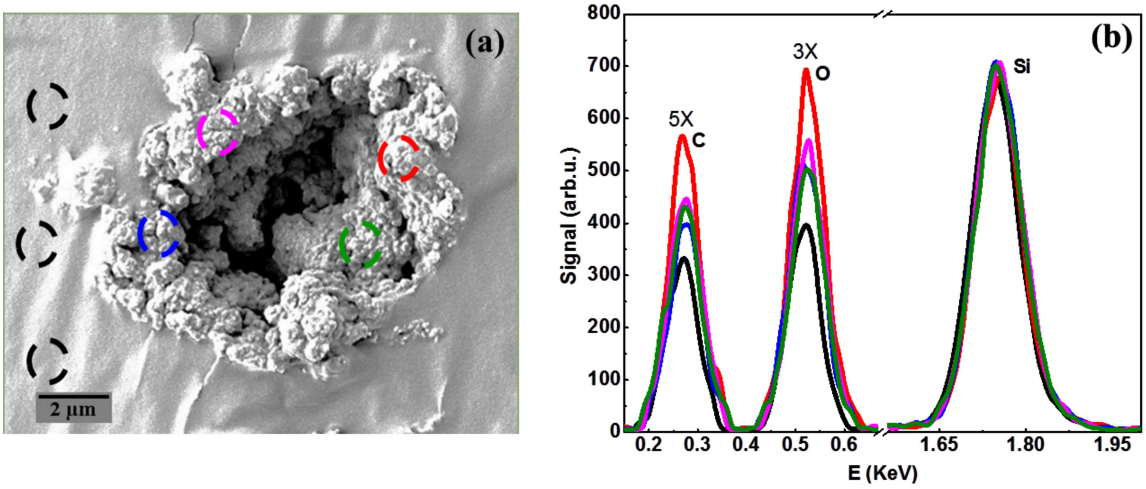

Figure 5.1: (a) SEM image of cross-section of a modified region fabricated 300 μm below the surface with a speed of 100 μm/s and a pulse energy of 200 nJ. (b) EDS spectra from different spots within and outside the modified region, identified by coloured circles in (a). The spectrum shown in black represents an average over three regions.

A Ti Sapphire laser system described in chapter 3 was focused 300 μm below the surface of PDMS by a 0.25 NA (16X) aspheric microscope objective to fabricate lines. After laser modification of PDMS the samples were cleaved and gold coated for characterization

with scanning electron microscope (SEM) and energy dispersive X-ray spectroscopy (EDS). The spatial resolution of EDS was $\sim$1 μm.

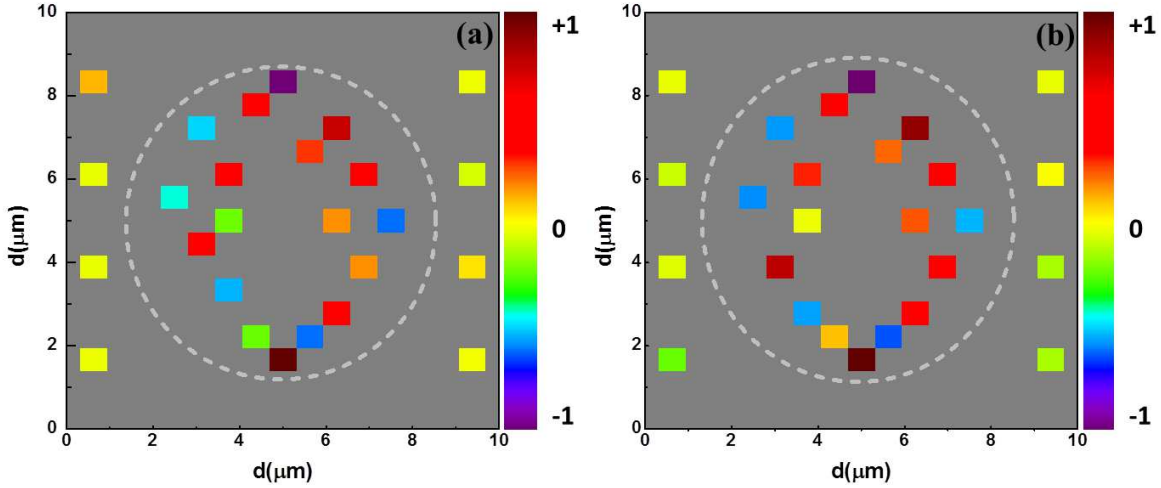

Figure 5.2: Element maps of (a) carbon and (b) oxygen within and outside the modified region, outlined by the dashed circle. The scale represents elemental concentration normalized to the unmodified region.

Figure 5.1(a) shows a SEM image of a cross-section of the laser modified region consisting of a void in the middle surrounded by material that is ablated from the centre. High temperatures and pressures generated within the focal volume due to the optical breakdown process transformed the material into a new form consisting of an agglomeration of nanometer sized clusters with marked faceting. This suggests that on a microscopic scale bond breaking and subsequent rearrangement of atoms/molecules has occurred within the polymer backbone. A semi-quantitative elemental analysis of different spots within and outside the laser modified region in PDMS was obtained using EDS as shown in figure 5.1(b). EDS spectra consist of three peaks corresponding to the characteristic k_α emission lines of carbon, oxygen and silicon at 0.28, 0.53 and 1.73 keV, respectively. The elemental analysis of unmodified PDMS was obtained by averaging the spectra recorded from different locations as shown by the black circles in figure

5.1(a). EDS spectra obtained from different regions on the rim of the modified region (identified by coloured circles in figure 5.1(a) show the carbon and oxygen concentrations to increase by 17-70% and 24-80%, respectively, relative to the unmodified regions. However, the Si concentration from the same spots remained unchanged within the measurement uncertainties.

For low density polymeric materials, the spatial resolution of the EDS probe is very high ($\sim 1\ \mu$m) at low accelerating voltages enabling to map elemental composition over the entire modified region. The colour maps illustrated in figure 5.2 show the distribution of the carbon and oxygen concentrations in and around the modified region. As the silicon concentration is nearly constant both in the modified and unmodified regions, it is used to normalize the carbon and oxygen counts. The elemental concentrations of unmodified PDMS are rescaled and used as a reference to study the concentration variations of carbon and oxygen across the modified region. Figure 5.2 shows carbon and oxygen concentrations to randomly vary across the laser modified regions. Negative (positive) numbers correspond to low (high) concentrations relative to that of the unmodified PDMS. There are regions where their concentrations are higher while they are lower in others. The results of the EDS mapping suggest clustering has resulted from laser irradiation. Since EDS is sensitive to surface topography, data was collected only from the edges of the modified region avoiding the central void like region where depth variations are significant. Data collected from several different modified regions fabricated under identical conditions show similar results.

Our EDS analysis shows carbon and oxygen concentrations to vary in tandem. In addition, the C/Si and O/Si ratios are always less than unity although carbon and oxygen concentrations have increased by up to 70-80% in some regions. This is in

contrast to the EDS and XPS analysis of surface irradiation of PDMS carried out with a Xe_2 excimer lamp at 172 nm [119], where the surface layer was found to be enriched in oxygen and depleted in carbon resulting in O/Si ratio of almost 2 corresponding to transformation of PDMS to SiO_2 like structure. In our experiments the femtosecond laser induced modification occurs in the bulk, 300 μm below the surface, whereas on the surface photochemical oxidation of PDMS can occur resulting in differences in carbon and oxygen concentrations and their ratios with respect to Si. Micromodification of elemental distribution has also been observed in doped glasses irradiated with light from a femtosecond laser [120, 121].

5.3 Photoluminescence and micro-Raman spectra

Presence of carbonaceous clusters within the laser modified region, as suggested by the EDS analysis, should lead to photoluminescence (PL) [5]. For the purpose of the photoluminescence analysis and micro-Raman spectroscopy, several closely spaced lines were fabricated in PDMS in 3D such that the cross section consisted of 20 laser modified regions within an area of 15 μm^2.

Figure 5.3(a) shows a PL spectrum obtained from laser modified PDMS excited with light at 488 nm. The PL spectrum peaks at ∼585 nm and is broad suggesting a wide distribution of cluster sizes. The measurements were made on a laser modified cross–section of ∼15 μm^2 and the PL was intense enough to be seen by the naked eye. No PL signal was observed from the pristine PDMS. Figure 5.3(b) shows the variation of PL intensity as a function of laser pulse energy used to modify PDMS. Increasing PL intensity with pulse energy is an indication of rise in the number of clusters. However, we did not observe any spectral shifts of the PL peaks with pulse energy suggesting

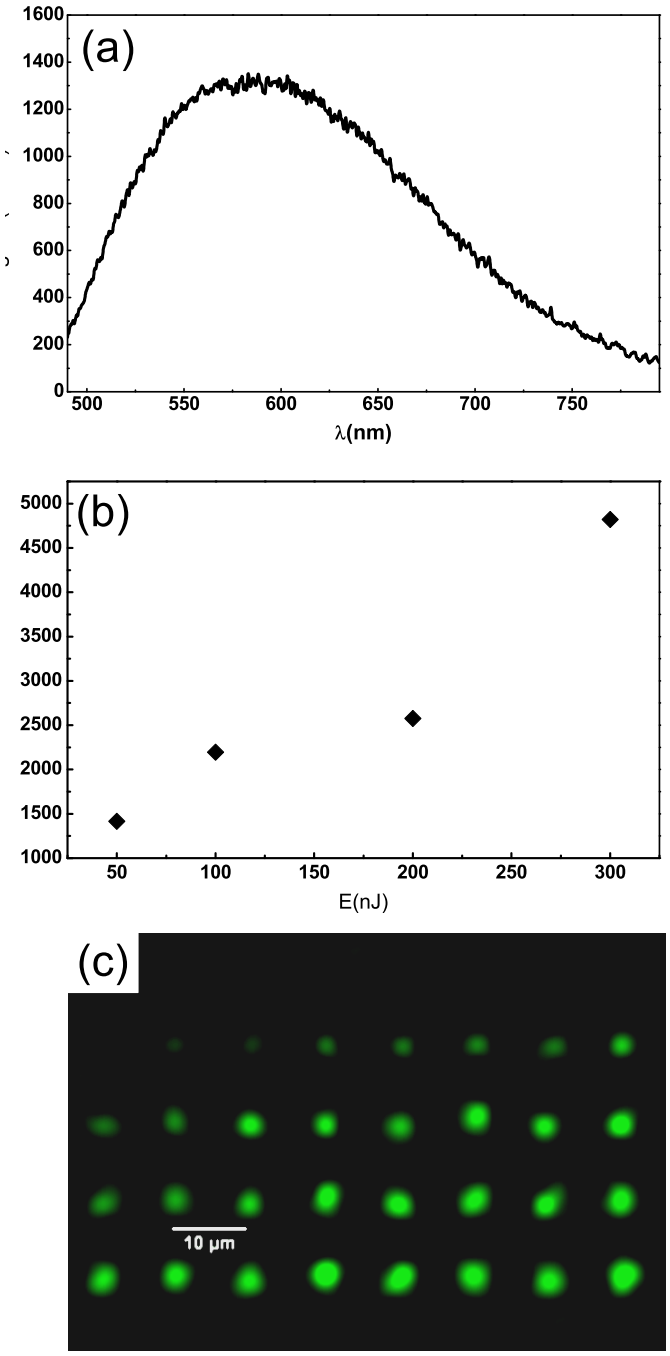

Figure 5.3: (a) Photoluminescence from the laser modified PDMS induced by coherent light at a wavelength of 488 nm. (b) shows the variation of the PL intensity with laser pulse energy. (c) Confocal microscope image, obtained at an excitation wavelength of 488 nm, of an array of laser modified spots under different irradiation conditions. See text for details.

that the cluster size distribution remained unchanged with laser pulse energy. Change in PL emission energy is known to vary with cluster size as the bandgap of the cluster materials changes [122,123]. Figure 5.3(c) shows confocal microscope image of an array of laser modified spots obtained at an excitation wavelength of 488 nm. Each row of spots is irradiated by 1, 2, 5, and 10 pulses, respectively from top to bottom with pulse energy varying from 355nJ - 430nJ in steps of 10nJ from left to right. Fluorescence signal from the laser modified spots increases with pulse energy (along the row) and with number of pulses (along the column), consistent with PL measurements.

Visible photoluminescence has been reported in Si based polymers [123–125] including PDMS [126] upon ion irradiation. PL was associated with segregation of diamond like carbon in an amorphized structure of the polymer induced by ion irradiation. PL in visible spectral range was also observed from carbon clusters embedded in SiO_2 [5,127]. The green PL is often associated with carbon clusters whereas the blue PL is associated with silicon clusters such as those formed by Si-O, Si-C and Si-O-C complexes [128]. However, the PL bands from Si are known to shift to red wavelengths with increasing cluster size [129] due to quantum confinement effect. Consequently, the green PL observed in laser modified PDMS can also be associated to silicon clusters although EDS analysis indicated no change in Si concentration.

To differentiate the contributions of carbon and silicon containing clusters, we carried out micro-Raman measurements on the laser modified and pure PDMS. Figure 5.4(a) shows the Raman spectra of pure PDMS (black) and in laser modified PDMS (red) at an excitation wavelength of 532 nm. The intense peaks in pure PDMS at 2965 cm^{-1} and 2907 cm^{-1} correspond to the stretching modes of the methyl group. The peaks at 484 and 708 cm^{-1} correspond to Si-O-Si stretching mode and Si-C symmetric stretch respectively

[130, 131]. Raman spectra of laser modified PDMS show a broad luminescence without any features with a maximum intensity at 503 cm^{-1}. Any signatures of carbonaceous clusters corresponding to graphitic [132, 133], C=C [134] and C=O modes which would appear in the range of 1300-1700 cm^{-1} of frequency modes are likely be hidden under the intense luminescence of the modified region making it difficult to observe them. Excitation at longer wavelengths such as 785 nm did not reduce the background to observe signatures of carbonaceous clusters.

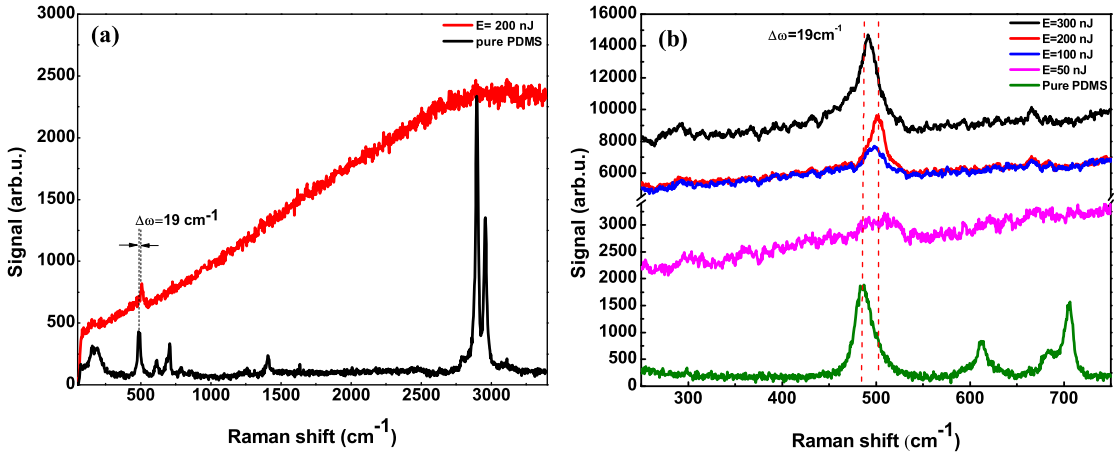

Figure 5.4: (a) Raman spectra of laser modified (red) and pristine (black) PDMS at an excitation wavelength of 532 nm. Note the strong photoluminescence superimposing the Raman scattering arising from the modified region. (b) Raman peak shift (around 484 cm^{-1}) in laser modified PDMS at different pulse energies relative to pristine PDMS with an excitation wavelength of 488 nm.

The Raman line at 503 cm^{-1} in laser modified PDMS is shifted by 19 cm^{-1} relative to the Si-O-Si stretching mode of pristine PDMS. Moreover, its position lies midway between that of crystalline Si at 520 cm^{-1} and amorphous Si at 480 cm^{-1}. This suggests structural rearrangement has occurred in PDMS upon irradiation with a femtosecond laser leading to formation of quasi-crystalline Si nanocrystals. Figure 5.4(b) shows the evolution of the Raman peak corresponding to Si nanocrystals as a function of pulse energy. For pulse energies of 50, 100, 200, and 300 nJ the observed shifts are 9, 15, 19,

and 8 cm^{-1} respectively. The peak shift to higher frequencies with laser pulse energy indicate transformation of silicon state from amorphous to quasi crystalline [135]. At higher pulse energies the clusters are probably destroyed resulting in a reduced size distribution and smaller peak shift. Such a behaviour has also been observed in PL measurements of ion irradiated polymers at higher fluences [123]. The intensity of the peak also increases with the pulse energy suggesting an increase in the number of the siliconaceous clusters.

The size of the silicon nanocrystalline clusters can be obtained from the bond polarizability model [136, 137]. In crystals with well-defined geometries and cluster sizes below 4 to 5 nm this model provides a better agreement with experimental Raman shifts compared to the well known phonon confinement models [138]. According to this model, the Raman shift in a nanocrystal with diameter D is given by

$$\Delta\omega(D) = \omega(D) - \omega_\circ = -A(a/D)^\gamma \tag{5.1}$$

where $\omega(D)$ represents the Raman frequency of the phonon in the cluster, $\omega_\circ$ is the Raman frequency for the phonon in the bulk and $a = 0.543$ nm is the lattice constant of the Si. The parameters A and γ describe the vibrational confinement due to the finite size in a nanocrystal and their values are obtained by fitting them to the calculated ones for Si spheres and columns. For spheres $A = 47.41 cm^{-1}$ and $\gamma = 1.44$ while for columns $A = 20.92 cm^{-1}$ and $\gamma = 1.08$. From the measured shifts of the Raman line of figure 5.4(b), the estimated cluster sizes are 1.7, 1.2, 1 and 1.9 nm for pulse energies of 50, 100, 200, and 300 nJ, respectively, assuming spherical shape for the clusters with 391, 133, 83, and 527 atoms /cluster.

5.4 Absorption spectroscopy

Laser induced structural changes to PDMS and the presence of carbonaceous and siliconaceous clusters alters light absorption compared to pristine PDMS, as shown in figure 5.5. The band edge of pristine PDMS is ∼240 nm corresponding to a bandgap of ∼5 eV [95, 139]. However, owing to a slight increase in absorption around 280 nm PDMS is transparent from 300 nm onwards. The absorption edge has shifted from UV - visible (at around 350 nm) under femtosecond laser irradiation resulting in a reduction in bandgap by about 30%. Such a change in bandgap upon laser irradiation has also been

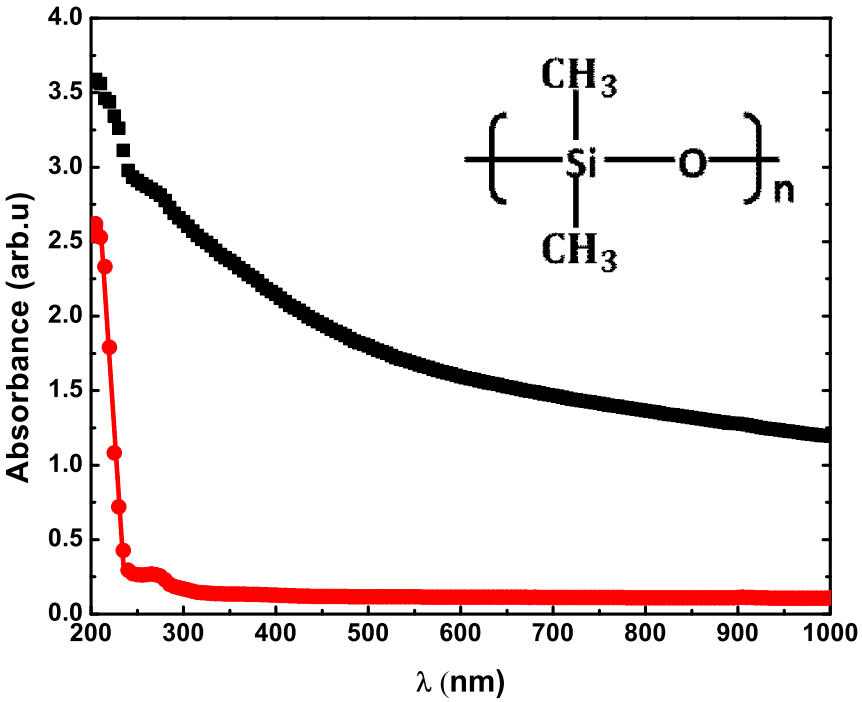

Figure 5.5: The light absorption spectrum of the pristine (red) and laser modified PDMS (black). Inset shows the repeating monomer unit of PDMS.

observed in other materials like fused silica [67]. Also, the overall absorption of laser modified PDMS has increased significantly but more so in the visible wavelength range rendering the modified region a brown-black colour. The cluster size can in principle

be estimated from the absorption edge of UV-visible spectra of irradiated polymers [75] by correlating the band gap with the number of the carbon bonds per linear or cyclic structure. We estimate 102 atoms per cluster.

5.5 Excitation and emission spectroscopy

Chemical analysis of the defects induced by the femtosecond laser in PDMS was investigated using fluorescence spectroscopy. For absorption and fluorescence spectroscopic studies a large laser modified area of 3 mm x 3 mm was fabricated 300 μm below the surface consisting of 1500 lines spaced by 2 μm. Figure 5.6(a) shows fluorescence emission spectra from modified PDMS excited at different wavelengths. Pristine PDMS is known to exhibit minimal fluorescence among plastic materials [95] and it decreases as the laser excitation wavelength is increased. In modified PDMS, emission intensity is maximum when excited with UV light at 250 nm and peaks at 400 nm with a shoulder at 445 nm. As the excitation wavelength increases the emission not only decreases in intensity but also shifts to longer wavelengths due to red-edge excitation. However, for excitation wavelength of 400 nm the emission intensity is higher than at 350 nm and then subsequently decreases with increasing excitation wavelength. Also, two new additional peaks appear at 530 nm and 608 nm when excited at 400 nm (peaks identified as b and c in figure 5.6(a). Such an emission behaviour suggests fluorescence emission from two distinct species.

Figure 5.6(b) shows the variation of the emission peaks with excitation wavelength. All three visible emission peaks (identified in figure 5.6(a) shift to longer wavelengths as the excitation wavelength is increased to the red edge of the absorption band. The linear relation between emission peaks and the excitation wavelength indicates red-edge

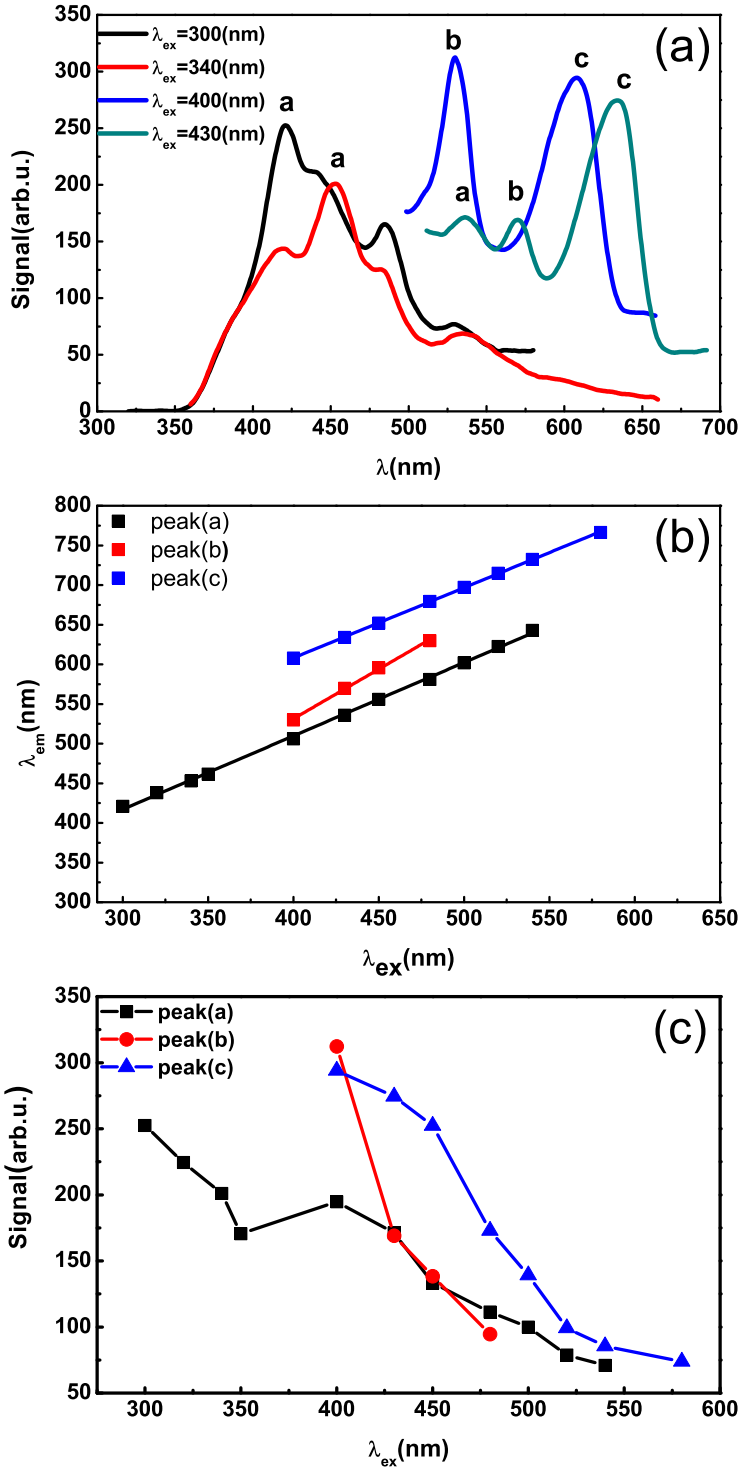

Figure 5.6: (a) Fluorescence emission spectra at different excitation wavelengths. (b) Red-edge excitation effect for the three peaks identified in (a). (c) shows variation of fluorescence intensity of the three peaks as a function of excitation wavelength.

excitation (REE) effect in PDMS. REE is related to excited state inhomogeneity due to dipole-dipole interactions between an ensemble of excited fluorophores and molecules in their surroundings [140]. It arises when the rigid matrix in which the fluorophores are embedded does not allow them to undergo relaxation on the time-scale of fluorescence decay. In condensed media, where energy of every state becomes distributed, absorption of a high energy photon causes excitation of fluorescence of all possible configurations which differ in interaction energy. When the system is excited with a lower energy photon (red edge of the absorption band) only the fluorophores constituting a part of the distribution will then be selectively excited. If there are no relaxations in the medium, then the emission energies of these fluorophores will also be lower. As a result, their emission spectra will be shifted toward longer wavelengths, compared to those excited at the band maximum. REE is most pronounced in polar solvents but has also been observed in polymer matrices [141–143].

Figure 5.6(c) shows the variation of fluorescence intensity of the three emission peaks with the excitation wavelength. The emission peak at 420 nm (peak a) in figure 5.6 is very broad and has been observed to shift up to 645 nm for excitation at 540 nm. The emission peak at 530 nm (peak b) has a narrower bandwidth and it declines fast as the excitation wavelength increases, while the peak at 608 nm (peak c) has broader bandwidth and decreases slowly.

Fluorescence excitation spectra enable to identify electronic transitions in functional groups of polymers. Transitions between occupied (one non-bonding n type and two bonding σ and π type) and unoccupied (two anti-bonding σ^* and π^* type) molecular orbitals are responsible for absorption and fluorescence [144]. Figure 5.7 shows excitation spectra measured for different emission wavelengths. We observed four distinct absorp-

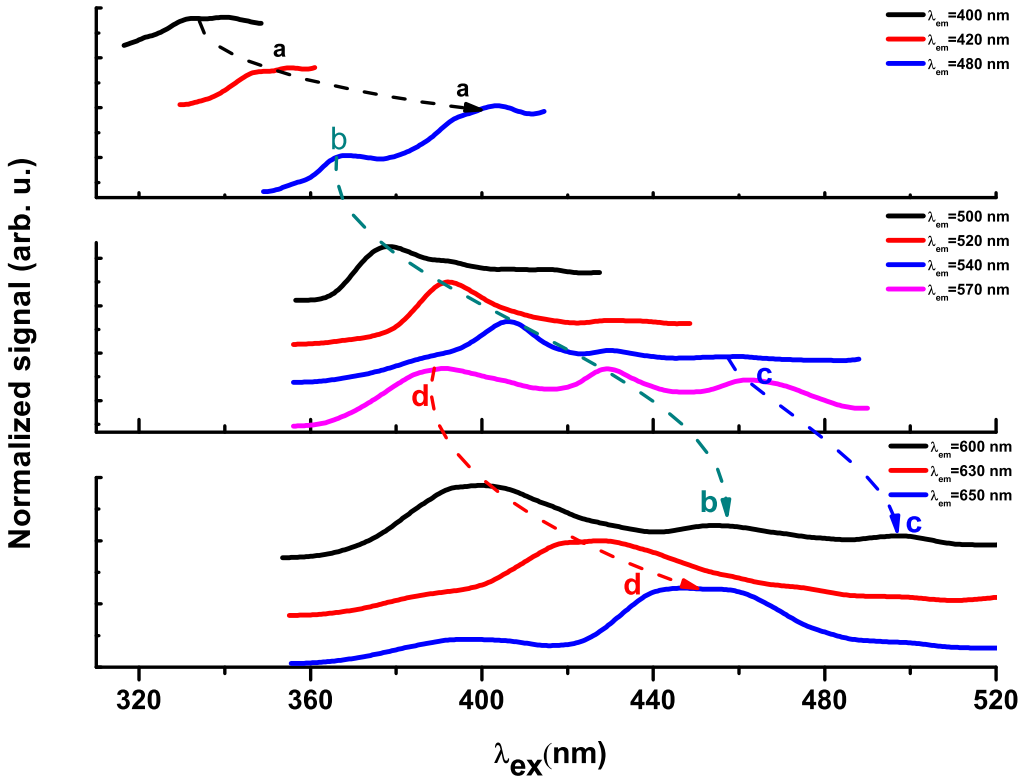

Figure 5.7: Fluorescence excitation spectra at different emission wavelengths. Dashed lines trace the red shift of absorption peaks, identified a-d, with excitation wavelength.

tion peaks that shift towards higher wavelengths with increasing emission wavelengths due to the red-edge excitation effect. The first peak, represented by a in figure 5.7, appears at 340 nm, undergoes a red shift until 415 nm and is responsible for fluorescence emission from 400 nm to 500 nm. The second peak, represented by b, starts at 370 nm and persists until 480 nm. It is responsible for fluorescence emission from 480 nm to 600 nm. The third peak, represented by c, emerges at 460nm and disappears after 560 nm. It is responsible for fluorescence emission from 540 nm to 600 nm. The fourth peak, represented by d, originates at 380 nm and ceases after 580 nm. It is responsible for fluorescence emission from 570 nm to 730 nm. Each of these absorption bands represent specific electronic transitions within a functional group of modified PDMS. They contribute to different regions of the broad photoluminescence observed in figure

5.3(b).

Origin of the peaks in the excitation spectra can be associated to the byproducts of photochemical reactions that occur when polymers are irradiated with energetic ions or photons (UV or intense infrared light). Bonds can be broken and subsequent structural rearrangement results in formation of new bonds. Although the photon energy is less than the bond energies (4.8 eV for Si-O, 3.3 eV for Si-C and 4.2 eV for C-H) multiphoton interaction of intense light with PDMS can lead to bond-breaking of the Si-O main chain or side groups Si-C and C-H. Subsequent reactions can lead to formation of carbonaceous and siliconaceous clusters.

In UV irradiation of PDMS surface in air, silanol groups were shown to form when Si and methylene radicals reacted with O forming peroxy radicals that subsequently rearranged and also when Si radical reacted with hydroxyl radical (formed by UV absorption in air) [119]. Similarly, Si-O-Si bridge was formed when oxygen radical attacked a Si-C bond [119]. Carbonyl groups were also detected in plasma modified PDMS [145]. Though the nature of interaction of light is different in bulk we anticipate similar rearrangement to occur in PDMS when irradiated with femtosecond light pulses.

Based on this we can now assign the four peaks observed in excitation spectra. The first pair of bands are associated with carbonaceous clusters involving carbonyl (C=O) or methylene groups (C=C). The first band can be ascribed to π to π^* transition of carbonyl or methylene groups while the second band can be associated with n to π^* transition of carbonyl group. This particular transition in both groups occurs at nearly the same wavelength [144]. These bands agree with the reported values in literature [146, 147]. The last pair of bands can be associated with electronic transitions in silicon clusters containing defects such as $=Si(O_2)$ and non-bridging oxygen hole center $\equiv$Si-O$\bullet$

and =Si-O-O$^{\bullet}$. The third excitation band, represented by peak c in figure 5.7, can be associated with non-bridging oxygen hole center ≡Si-O$\bullet$ or =Si-O-O$^{\bullet}$ with an absorption peak at 2.2 eV [148,149]. The fourth band, represented by d, can be associated to the formation of dioxasilirane =Si(O_2) whose excitation energy was estimated to occur at ∼3 eV [150–153].

5.6 Conclusion

This chapter demonstrated formation of embedded and localized carbonaceous and siliconaceous clusters in PDMS irradiated by femtosecond laser. These confined clusters exhibited broad photoluminescence in the visible region and contributed to the observed red-edge excitation effect. They are formed due to structural rearrangement induced by the femtosecond. The siliconaceous clusters also include quasi-crystalline Si as suggested by Raman. Spectroscopic studies suggested two distinct electronic transitions in each of these clusters that contribute to the observed luminescence. Such photoluminescent clusters embedded in a solid matrix could find applications in high density 3D data storage, display technology and cell migration studies. The formation of nanoclusters upon irradiation with fs–laser pulses is inherent feature in almost all polymers such as PMMA, Polystyrene, PC, and etc. The capability of producing fluorescence locally in the bulk of polymers was used for fabrication of 3D high density data storage in plastics, as will be discussed in the following chapter.

Chapter 6

Ultra-high density optical data storage in common transparent plastics

This chapter demonstrates high-density data storage in polymers. The ever-increasing demand for high data storage capacity has spurred research on development of innovative technologies and new storage materials. Conventional GByte optical discs (DVDs and Blu–ray) can be transformed into ultrahigh capacity storage media by encoding multi-level and multiplexed information within the three dimensional volume of a recording medium. However, in most cases the recording medium had to be photosensitive requiring doping with photochromic molecules or nanoparticles in a multilayer stack or in the bulk material. This chapter shows high-density data storage in commonly available plastics without any special material preparation. A pulsed laser was used to record data in micron-sized modified regions. Upon excitation by the read laser, each modified region emits fluorescence whose intensity represents 32 grey levels corresponding

to 5 bits. We demonstrate up to 20 layers of embedded data. Adjusting the read laser power and detector sensitivity storage capacities up to 0.2 TBytes can be achieved in a standard 120 mm disc.

6.1 Introduction

In conventional optical compact discs (CD) and Digital Versatile Discs (DVD), data storage is mostly confined to the surface of polycarbonate (PC). Data is stored in optical discs as a binary data that consist of a pit with value of 0 for no reflection and a land with value of 1 due to reflection. Data encoding in the disc is achieved either by laser or machine stamping. The data is encoded in a spiral path that starts from the innermost to outermost of the disc. The maximum data that can be stored in CD and DVD are 700 MB and 4.7 GB, respectively. The data can be read when the surface is illuminated by diode laser (650 nm), which spins the surface with high speed. Reflections detected by photodiode are registered as a bit value of 1.

Disc capacity is determined by the bit density and depends on the wavelength of light and the numerical aperture (NA) of focusing optics used to record/read the data. Development of laser sources at shorter wavelengths and high NA optics resulted in smaller bit sizes and improved disc capacities. The Blu-ray disc can store data in 2-3 layers, with a storage of 25 GB per layer. The read laser in Blu-ray technology is blue laser with wavelength of 405 nm. However, this planar technology cannot be scaled up due to the response and design of materials below 400 nm [154]. Storing information bits in a multi-layer structure using the three dimensional (3D) volume of the disc can overcome this limitation and provide ultra-high storage capacities due to the cubic dependence on the inverse of wavelength [155, 156].

3D optical data storage often relies on the nature of laser-induced chemical or optical changes in the recording medium. One such 3D technology is the Holographic Versatile Disc (HVD). Recording data in this technology starts with converting the object into binary map of ones and zeros. After that the binary is converted to a matrix of light and dark squares. The dark and light squares are programed in Spatial Light Modulator(SLM). The writing process involves splitting blue or green laser into two beams, the information beam and the reference beam. The information beam is sent to the SLM, and the pixels of the SLM block or allow the light to pass. Hence, the data is encoded in the laser beam. The reference beam interferes with the information beam and records a hologram in the medium. The data can be retrieved with one laser. In the read process, the data hologram diffracts the read laser beam according to the hologram pattern that was stored. The bounced light is directed to a photo-sensor. Holography technology is capable of producing high-density data storage, but it is still confronted by real technical challenges, related to recording medium, storing and reading data [157–159].

Another technology depends on the use of femtosecond lase pulses to induce changes in the recording medium in the form of refractive index/birefringence [155, 156], aggregation of metal nanoclusters [156] or shape alteration of metal nanorods [160, 161]. The technology relies on using ultrafast lasers to confine the changes in the medium on a micron scale [155, 156, 161–163]. Higher storage capacities could be achieved by utilizing the nonlinear nature of the fs-laser interaction with recording medium. This allows overcoming the diffraction limit of light and recording data on submicron scale. Higher storage also can be achieved by multiplexing different properties of the light-matter interaction.

3D optical storage was first demonstrated by modifying the refractive index of pho-

topolymers [164] and glass [155] locally on micron scale. Data was recorded *bit-by-bit* and retrieved by phase contrast microscopy. Recently, this technique was extended to demonstrate multilevel encoding of intensity and polarization states of light with self- assembled periodic nanostructures produced by an ultrafast laser in glass [156,165]. Data was retrieved by measuring the laser induced birefringence associated with the orientation of nanogratings. However, in both cases data retrieval is influenced by interference effects and/or low detection sensitivity limiting the number of data layers.

Data can alternatively be retrieved by fluorescence emission from the recorded bits. This has the added benefit of integrating the existing read technology. However, the recording medium had to be photosensitive, just as in the case of 3D holography. This led to a constant search for novel materials that are suitable for a recording medium [160–163, 166, 167]. Using silver doped zinc phosphate glass, 20 Gbits/cm^3 of storage capacity was demonstrated by inducing embedded silver nanoclusters using an ultrafast laser [162]. Upon excitation with a read laser the nanoclusters emit fluorescence. Even higher capacities of up to 1 Tbits/cm^3 were explored in 5D technology by utilizing the unique properties of surface plasmon resonance of gold nanorods stacked in multiple layers and using non-Gaussian laser beams to imprint the data [160, 161, 167].

In this chapter, we demonstrate high-density data storage in common inexpensive plastics. Clear plastics such as polymethylmethacrylate (PMMA), polycarbonate (PC), polydimethylsiloxane (PDMS), and polystyrene (PS) do not fluoresce in the visible spectrum. Irradiation by an ultrafast-laser pulse results in chemical changes followed by rearrangement leading to the formation of permanent defects [27,147,168]. The multiphoton nature of the laser-matter interaction confines these defects to very small volumes in the polymer matrix. These fluorescent moieties most likely derive from the polymer itself or

from the additives that are used as stabilizers, such as UV protectors and antioxidants. Upon excitation with a read laser these defects emit fluorescence and the data is read in a confocal geometry. The fact that different excitation wavelengths lead to different emission profiles implies that more than one emitting chromophore is produced upon multiphoton excitation. The simplicity of our approach enables data access with multiple excitation sources unlike other techniques. The stored data can be embedded in the bulk material and is thermally stable up to the glass transition temperature of the recording medium thereby offering a long shelf life. Our technique eliminates the need for the recording medium to be photosensitive and the multiple steps involved in their preparation.

6.2 Multi-level encoding dynamics

The multi-level encoding dynamics was studied by fabricating an array of periodic laser–modified regions. Each row corresponded to a specific energy and consisted of a set of 140 modified regions. Pulse energy was varied from 10 nJ to 920 nJ in small increments. A water immersion microscope objective (Olympus, LUMPlan F1/IR, 0.9 NA, 60X magnification, 2mm working distance) was used to focus light 100 μm below the PMMA surface. The spacing between each modified region in a row was 1.4 μm obtained by scanning the sample at a speed of 1.4 mm/s. Each successive rows (corresponding to different pulse energies) were separated 5 μm. Fluorescence from the laser-modified regions was recorded using Nikon A1RMPST confocal fluorescence microscope with a 25X objective (NA 1.1, working distance 2mm, water immersion) at two excitation wavelengths of 488 nm and 405 nm with emission windows in 500 – 550 nm and 425 – 475 nm range, respectively. The power of the CW read laser and sensitivity of the

detector for 488 nm (405 nm) excitation were 100 μW and 82 V (200 μW and 142 V), respectively. Each fluorescence image recorded 18 rows of modified regions corresponding to different pulse energies. Successive images consisted of 3 common rows of modified regions to normalize the fluorescence intensity. Image J software was used to evaluate mean and standard deviation of fluorescence by averaging 15 – 20 modified regions for each energy. The fluctuation in the fluorescence intensity was then used to divide the linear dependence of the fluorescence signal on ultrafast laser pulse energy into multiple grey levels as shown in figure 6.1(c). 5-bit images were also analyzed by Image J to obtain 3D stacks. Each reconstructed image consisted of 20 layers.

Figure 6.1(a) shows confocal fluorescence microscope image obtained with 488 nm excitation. Each column consists of a series of laser-modified regions irradiated by a single laser pulse at a specific energy with a pitch of 1.4 μm and successive columns were separated by 5 μm. The minimum energy required to induce fluorescence in PMMA with a single laser pulse was $\sim$ 25 nJ below which there was no detectable fluorescence in the emission window of 500 – 550 nm. The fluorescence intensity increased with the pulse energy of the ultrafast laser up to $\sim$ 130 nJ above which the modified regions started to overlap. Further increase in the pulse energy resulted in formation of voids with no increase in the fluorescence intensity.

Figure 6.1(b) shows the fluorescence emission spectrum in PMMA for pristine (blue and brown curves) and laser modified regions (black and red curves in figure 6.1(b)) at two different excitation wavelengths. Pristine PMMA does not fluoresce in the visible spectrum. The fluorescence moieties induced by the femtosecond laser exhibit different emission profiles upon excitation at different wavelengths. The fluorescence signal intensity from the ultrafast laser irradiated regions within the material varied with the

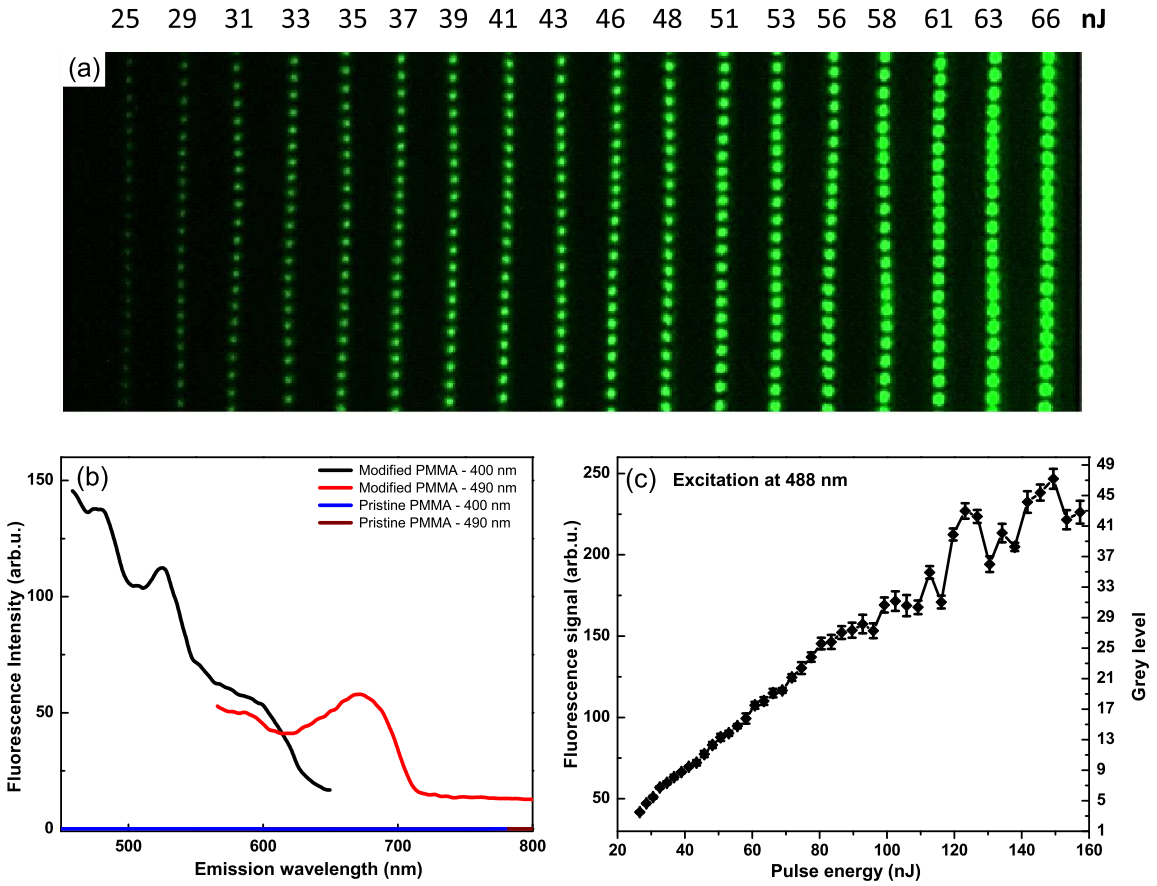

Figure 6.1: Fluorescence in PMMA from laser irradiated regions. (a). Confocal fluorescence microscope image of ultra-fast laser modified regions. Excitation wavelength was 488 nm and emission was recorded in the wavelength range of window 500 – 550 nm. Each column shows fluorescence from a periodic array of modified regions irradiated with a single laser pulse of specific energy. (b). Fluorescence (emission) spectra from pristine and modified PMMA at 400, and 490 nm excitations obtained with a conventional fluorescence spectrometer. (c). Evolution of fluorescence signal with the energy of a single fs pulse obtained from (a). Based on the fluctuation of the fluorescence signal grey level was assigned to fluorescence as shown on the right ordinate. Error bars indicate the standard deviation of data

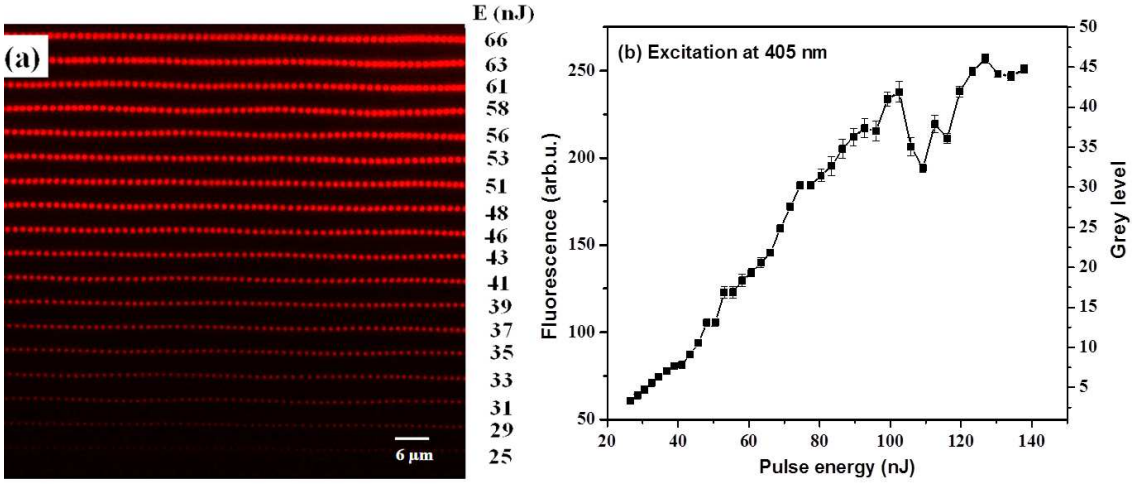

Figure 6.2: 5-bit encoding dynamics. (a). Confocal fluorescence microscope image of ultra-fast laser modified regions fabricated using 60X (0.9 NA) water immersion microscope objective and recorded at 405 nm wavelength (emission window 425- 475 nm) with 25X (NA 1.1, working distance 2 mm) Nikon water immersion microscope objective. Energy of each series of modifications is shown on right panel. (b). Plot of evolution of fluorescence signal with pulse energy. Grey level assigned to fluorescence is shown on the right ordinate.

pulse energy used to induce the emissive centres.

The evolution of fluorescence signal with the energy of the recording laser was used to assign different grey levels. This unique feature enables to represent each modified region with several bits of data, increasing the storage capacity. Figure 6.1(c) shows the division of the fluorescence signal into different grey levels associated with different pulse energies of the recording laser. The absence of fluorescence signal below 25 nJ represented level 0. The linearity of the fluorescence signal with pulse energy enabled us to assign 32 levels corresponding to 5 bits of data. Similar results were obtained with a different read/excitation laser as shown in figure 6.2, and in different materials PDMS, PS and PC as shown in figure 6.3. This flexibility offers the data to be stored in commonly available plastics and be accessed at any excitation within the visible spectrum.

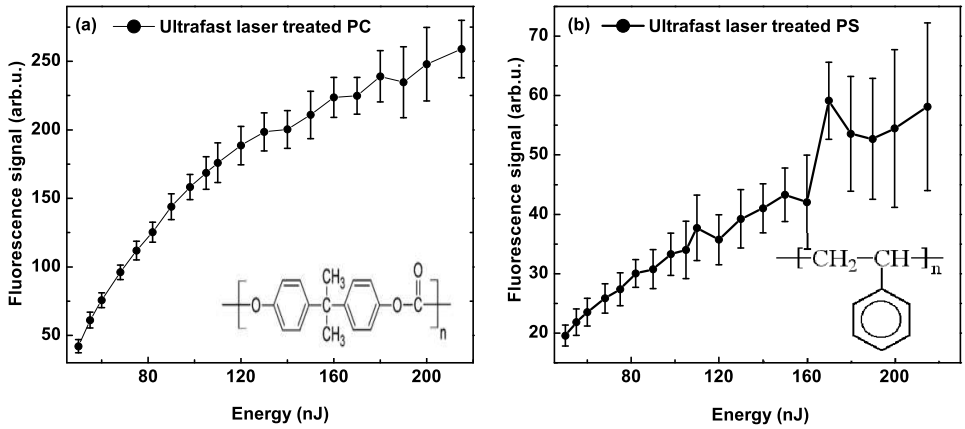

Figure 6.3: Generic feature of fs-laser induced Fluorescence in all plastics. Evolution of signal with the pulse energy of ultrafast laser in PC (a) and PS (b). Chemical structures are shown in inset. The laser-modified regions were excited with 488 nm light.

5-bit encoding dynamics was also investigated with 405 nm excitation. Blu-ray technology utilizes 400 nm light to read the data on a disc instead of 488 nm that was used in our experiments. To demonstrate the adaptability of our technique with the existing technology we studied the feasibility of multi-level encoding with 405 nm excitation of the read laser. Figure 6.2(a) shows the fluorescence emitted by these modified regions in the window 425 – 475 nm. The fluorescence signal was recorded and analyzed over 15 – 20 modified regions for each specific energy using Image J. Figure 6.2(b) shows the evolution of fluorescence signal with the pulse energy of the write laser. The linear variation of the fluorescence signal enables division into different grey levels shown along the right ordinate of figure 6.2(b). The behaviour of fluorescence signal at 405 nm laser excitation is similar to that obtained at 488 nm write laser. Both excitations enabled us to assign 32 levels of grey corresponding to 5 bits of data.

Studies were extended to other transparent plastics to test the generic and ubiquitous feature of laser induced photosensitization in plastics. Series of fluorescent dots were fabricated with 0.55 NA (40X) microscope objective in 5 mm thick (area of 10 mm x

20 mm) Polycarbonate sheet (PC–Goodfellow UK) and Polystyrene (PS–Fisherbrand petridish) in the energy range of 50 – 520 nJ, 100 μm below the surface with 2 μm pitch between two successive dots. Each series was fabricated at a specific energy and two successive series of dots were separated by 5 μm. These fluorescent dots were read using confocal fluorescence microscope at 488 nm (500 – 550 nm emission window; sensitivity of 157 V and 100 μW of excitation power) and 405 nm light (425 – 475 nm emission window; sensitivity of 100V and 328 μW of excitation power). Fluorescence signal was recorded from multiple optical sections of the modified region and stacked for analysis using Image J by averaging over 10–15 dots for each laser energy at the excitation of 488 nm.

Figures 6.3(a), and figure 6.3(b) show the evolution of fluorescence signal with laser energy in PC and PS at 488 nm laser excitation, respectively. The insets show their chemical structures. Both show linear variation of the fluorescence signal with write laser pulse energy. However, the fluorescence signal in modified PS was small compared with PC. As a result, the possible number of grey levels would be small in PS compared to PC or PMMA. Both PC and PS contain aromatic (benzene) rings. We believe that upon ultrafast laser irradiation these polymer chains break up and form loose aromatic double bond structures that give rise to fluorescence emission. Earlier research on UV exposure of PS showed formation of three possible double bonded aromatic structures namely trans–stilbene, diphenylbutadiene (DPBD), and diphenylhexatriene (DPHT), all of them exhibited fluorescence emission in the 330 – 520 nm range with absorption bands in 280 – 460 nm [169]. It is therefore possible that multiphoton excitation at 800 nm wavelength in our case can cause similar dynamics. Fluorescence from irradiated plastics is not unique to ultrafast lasers. It has been observed when plastics were exposed to

UV, gamma and electron beams [169–171]. However, the unique capability of ultrafast lasers to localize the emission to micron volumes enables high-density data storage.

6.3 Recording and retrieving 5–bit images in 3D

The image fabrication was carried out by spatially filtering the raw image initially to remove any artifacts. Pixels of similar value were then clustered before the image was re-sampled to a printable resolution. Following histogram equalization, the image was subdivided into the desired number of grey levels as determined by its intensity distribution. To speed up the printing process and minimize wear on the translation stages, pixels of identical value were grouped into particles for which an individual map of coordinates were generated. Once a focal plane was determined, printing of an image was done by scaling the energy range of the laser to the corresponding grey level and by sending the scaled pixel coordinates of particles, one by one, to the motion stage controller, while triggering the laser for each pixel.

The usefulness of inexpensive plastics for data storage applications is demonstrated in figure 6.4 where a black and white 5–bit image (32 grey levels) of Richard Feynman was recorded inside PMMA with an ultrafast laser (figure 6.4(a), (b)). Using a 488 nm CW laser in conjunction with a confocal microscope the fluorescence from the recorded image was retrieved and decoded (figure 6.4(c), (d)). The size of the original image was 105 x 147 pixels (figure 6.4(a)). Assigning the 32 grey levels to the pulse energies in the range of 25 – 130 nJ resulted in the processed image, Figure 6.4(b), which was used to record the image. The pixel spacing of the recorded image was 1.4 μm with a pixel size that varied with pulse energy up to a maximum of 1.1 μm (figure 6.5). The pixel spacing was chosen to minimize the cross talk between two adjacent pixels

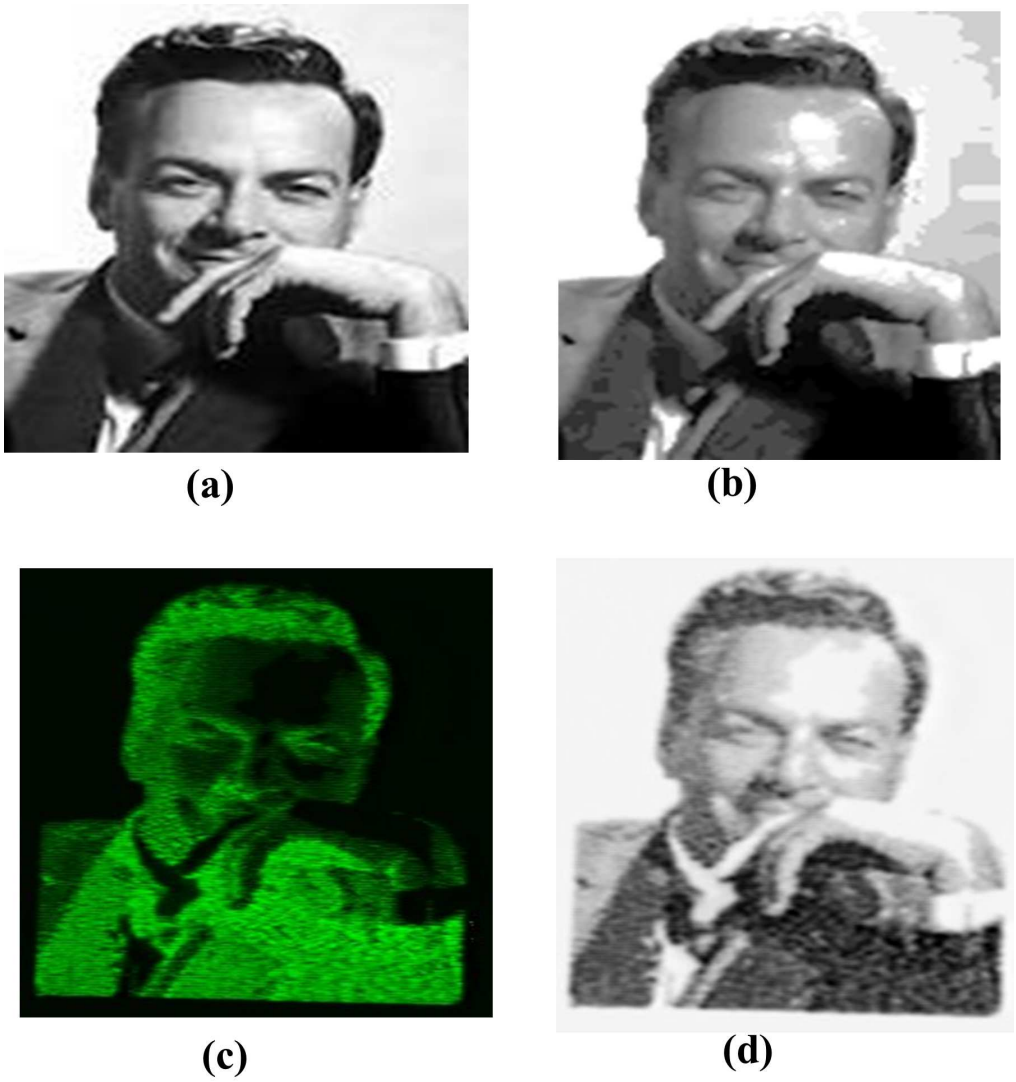

Figure 6.4: 5–bit (32 grey-level) image fabrication. (a). Multi-grey image of Richard Feynman (105 pixels × 147 pixels) (Nobel laureate in Physics in 1965). (b) Processed image after assigning 32 grey levels corresponding to write laser pulse energy range of 25 – 130 nJ. (c). Confocal fluorescence microscope image of b obtained by a CW, 488 nm read laser at 100 μW of power. (d). Reconstructed negative image of (c). This figure is not covered by the CC BY license [Credits to The Canadian Press]. All rights reserved, used with permission.

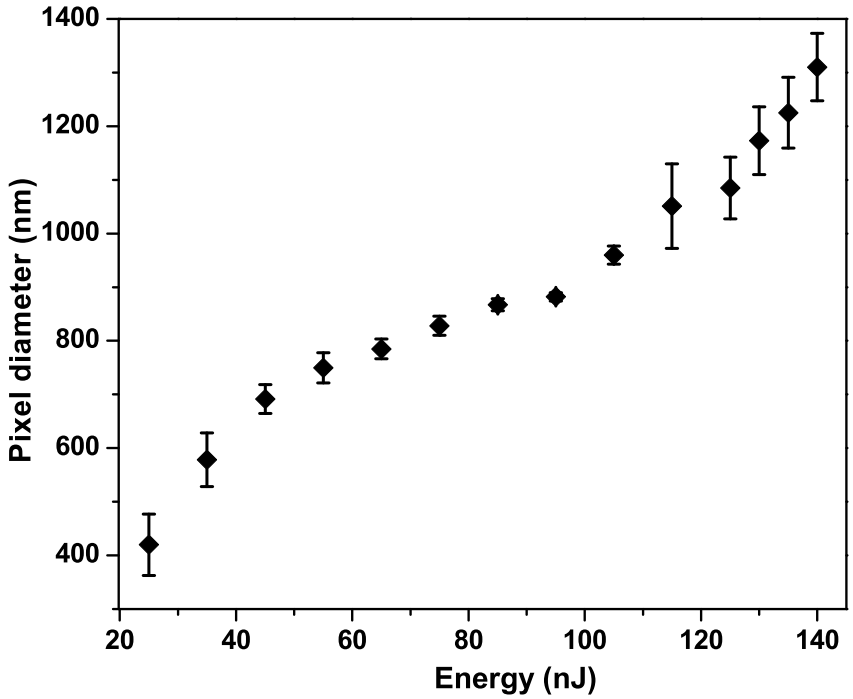

Figure 6.5: Variation of pixel size with laser pulse energy.

representing the highest grey level. High laser pulse energies are required to record such pixels resulting in large pixel size. Fluorescence from each pixel, when excited by the read laser, represents a particular grey level (figure 6.4(c)). A negative of the retrieved fluorescence image reproduced the recorded data (figure 6.4(d)).

The packing density provides information on the number of images that can be stacked without loss of information during the retrieval process and was obtained by measuring the variation of the normalized fluorescence signal with depth. 3-bit embedded images of Albert Einstein (80 pixels $\times$ 103 pixels) and a maple leaf (100 pixels x 100 pixels) were fabricated at different depths alternately separated by 40 μm, using 0.9 NA, 60X microscope objective with laser pulse energy range 25 – 130 nJ. Confocal fluorescence microscope images were recorded with 488nm excitation (power 100 μW, sensitivity 82V). An integrated fluorescence signal from each image was obtained using Image J and normalized to the image fabricated closest to the surface.

Packing density is governed by the pixel and layer spacing. The optimal spacing is determined by the requirement of minimal cross-talk between adjacent pixels and image layers. Pixels fabricated at different laser pulse energies varied in size as shown in figure 6.5. The pixel sizes were determined by imaging the fluorescence using a confocal microscope. A bit spacing of 1.4 μm used in the experiments was determined primarily by the maximum pulse energy at which (a) the fluorescence signal variation was still linear (as in figure 6.1(c)), and two adjacent bits did not overlap. We used maximum pulse energy of 130 nJ corresponding to a bit size of 1.2 μm. Therefore, a spacing of 1.4 μm ensures no physical overlap between two bits representing the highest grey level.

The 3D data storage capability of our technique is demonstrated in figure 6.6(a) where a stack of three images of Canada goose, Albert Einstein and Gerhard Herzberg, respectively, were embedded 200 μm below the surface of PMMA with a 20 μm layer separation. In all cases the original images were downsized to reduce the fabrication time and were assigned grey levels (left column). The decoded images, obtained by optical sectioning of the modified region and stacking the fluorescence signal, were shown in the right column. A 40 μm^3 volume (with a pixel spacing 1.4 μm, 20 μm layer separation) represents 5 bits of data leading to a maximum storage capacity of 127 Gbits/cm^3. Practical storage capacity that can be achieved will be lower as discussed below. The lateral view of the 3D stack of 6.6(b) shows no crosstalk between the layers. Each fluorescent bit had a depth of nearly 8 μm due to confocal parameter of focusing optics (0.9 NA). It is therefore possible to reduce the layer spacing further to 10 μm and subsequently increase the maximum storage capacity to 0.25 Tbits/cm^3 (figure 6.7).

To estimate the maximum feasible package density and hence the disc storage capacity, we fabricated embedded images (300 μm below surface) of 32-grey of Albert

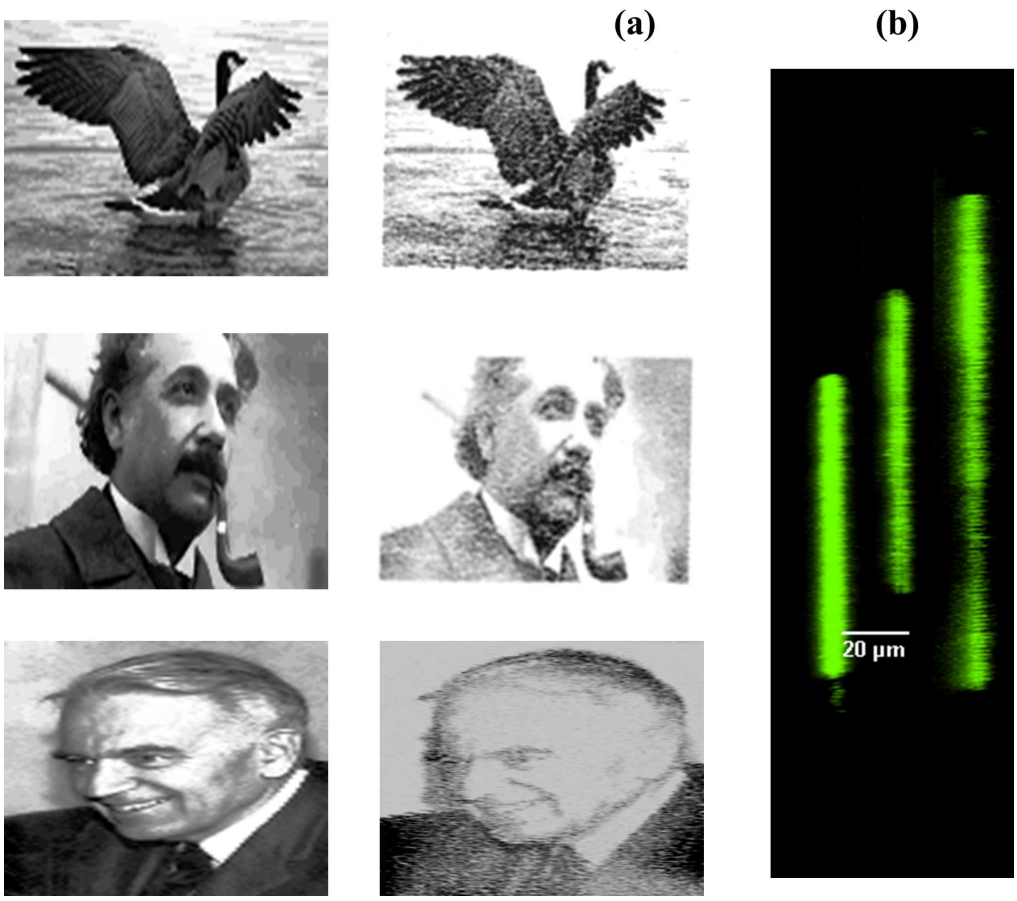

Figure 6.6: 3D stacked 5–bit images. (a) Set of three 32 grey level images of a Canada goose (113 pixels × 75 pixels), Albert Einstein–Nobel laureate in Physics in 1921 (145 pixels × 87 pixels), and Gerhard berg – Nobel laureate in Chemistry in 1971 (81 pixels × 113 pixels) stacked on top of each other with a spacing of 20 μm. The left column shows the individual processed images and the right one shows the images recovered by confocal fluorescence microscopy at an excitation wavelength of 488nm. (b) Lateral view of 3D stack of confocal fluorescence microscopy images shown in (a). Image of Canada goose is covered by the CC BY licence. [Credits to the Nature mapping foundation for usage of this image [172, 173], License to use the image is released under [174]. The image for Albert Einstein is not covered by CC BY license. [Credits to Getty Images for Albert Einstein]. All rights reserved, used with permission. The image of Gerhard Herzberg is not covered by CC BY license. [Credits to Mary Evans Picture Library/The Canadian Press]. All rights reserved, used with permission.

Einstein, Richard Feynman, and maple leaf with a 10 μm separation in PMMA using 0.9 NA (60X) water immersion microscope objective as shown in figure 6.7. The images were downsized to reduce fabrication time. We observed a slight signal overlap between adjacent layers from lateral cross-section of the stack shown in bottom of figure 6.7.

Optical sectioning and stacking can be time consuming but is not critical. A single intense central plane can be sufficient to retrieve the recorded images without loss of information and therefore reduce the read time. Figure 6.8 shows 5–bit images of Einstein; (a) was used to record the image, (b) was retrieved by stacking different layers while (c) was obtained from a single plane.

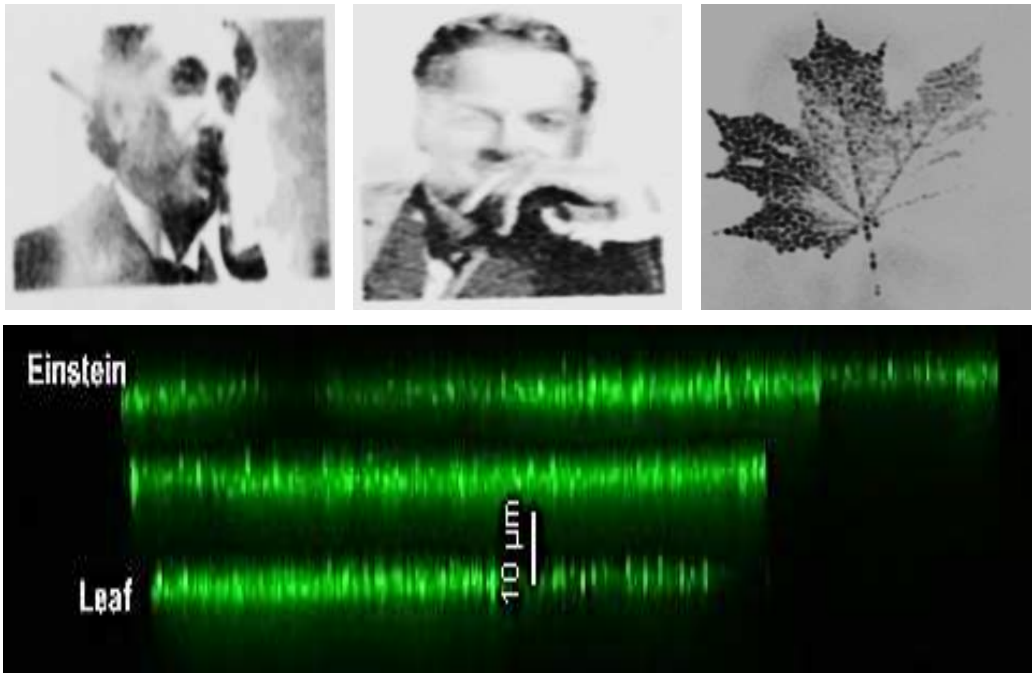

Figure 6.7: Package density. 32-grey level embedded images of Albert Einstein (145 pixels × 87 pixels) (Image Courtesy:Getty images) and Richard Feynman (87pixels × 122 pixels) (Image Courtesy: The Canadian Press) (shown in top row), and maple leaf (115 pixels × 110 pixels) (shown in bottom left) (Image Courtesy: Gettyimages). These images were fabricated with 15 μm separation as shown in lateral cross-section image of the stack in bottom left. Images were obtained from single intense planes of the optically sectioned stacks.

(a) (b) (c)

Figure 6.8: Faster image retrieval – 3D stack vs single section Decoded 32-grey level images of Nobel laureate Albert Einstein after 3D-stacking all the sections (middle panel), and from the single intense plane of the stack (right panel). Image on left was used to fabricate inside PMMA. Recorded images were read using confocal fluorescence microscope at 488 nm excitation (500 – 550 nm emission). This figure is not covered by the CC BY licence [Credits to Getty Images]. All rights reserved, used with permission.

The multiphoton nature of the interaction of ultrafast lasers with transparent dielectrics is known to enable recording multiple layers of data. However, retrieving the data can be affected by the transmission of the read laser through different layers of the modified material. Figure 6.9(a) shows the variation of the integrated fluorescence signal obtained from individual images embedded at different depths in PMMA, which were normalized to the image closest to the surface. 3-bit images (8-grey levels) of Albert Einstein and a maple leaf were fabricated at different depths alternately, and were separated by 40 μm. The images were retrieved using confocal microscope with 488 nm read laser at the same power and detector sensitivity. The reduction in the normalized fluorescence signal can be attributed to losses in transmission of the read laser and scattering of the fluorescence from layers above.

In optical data storage technology, the number of layers of data that can be retrieved without loss of information is one of the factors that plays a major role in disc capacity. The reduction of fluorescence signal observed in figure 6.9(a) can lead to loss of informa-

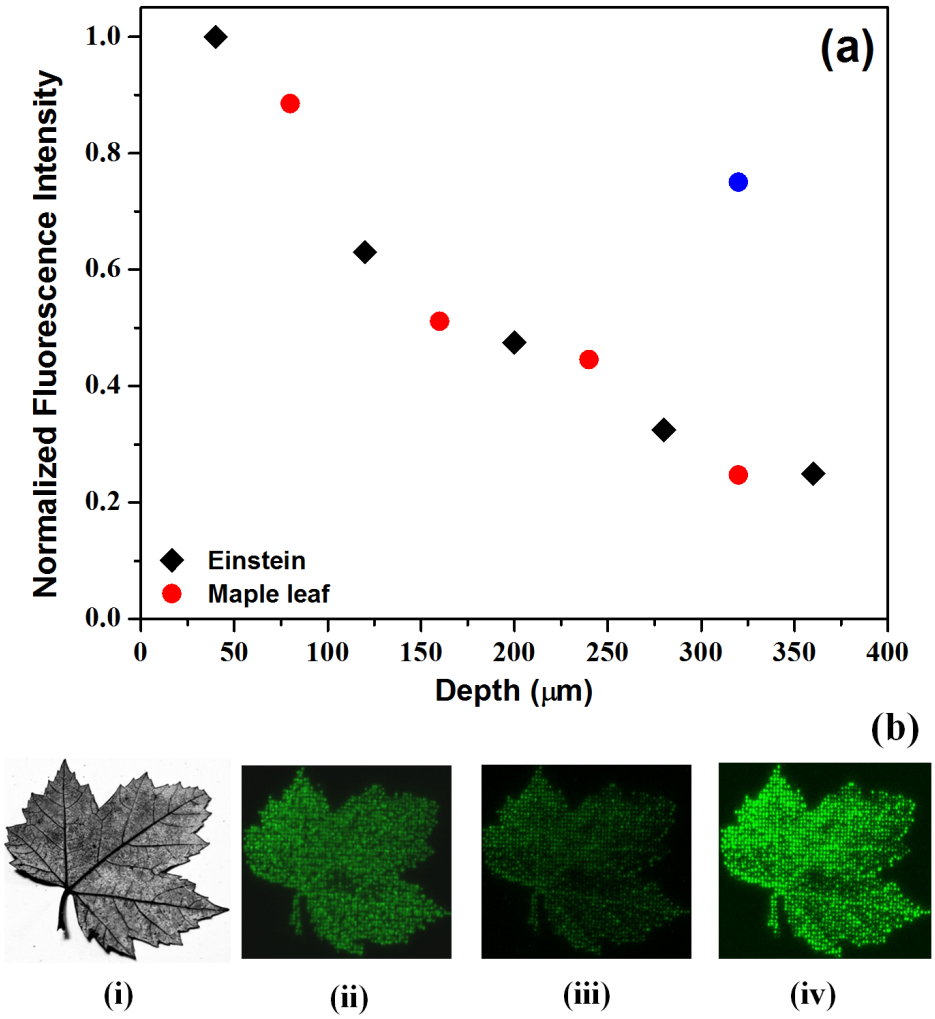

Figure 6.9: a. Variation of integrated fluorescence signal with the number of stacked images. The integrated fluorescence signal from the embedded layers of 3-bit images of Albert Einstein (black squares) and a maple leaf (red circles) decreased with the number of layers. The layer spacing was 40 μm. Read laser wavelength was 488 nm and the power was 100 μW. The blue data point corresponds to a read laser power of 340 μW. Fluorescence optimization (i.) Grey image (8 levels) of maple leaf (shown in left) used for fabrication at different depths in PMMA. (ii, iii.) Fluorescence images of maple leaf at 200, and 360 μm below the surface, respectively, obtained using 488 nm light at 100 μW of power, and the detector sensitivity of 82 V. (iv) The reduced fluorescence signal of image c at a depth of 360 μm could be recovered by increasing the read laser power to 340 μW. The image of maple leaf is not covered by the CC BY licence [Credits to Marc P. Bergen]

.

tion but could be easily recovered either by increasing the detector sensitivity and/or the read laser power. Figure 6.9(b) (i) shows the image of maple leaf (8-grey levels) used for recording at different depths. For a fixed power of the read laser (100 μW of 488 nm light) and the detector sensitivity (82V), figure 6.9(b)(ii) and (b)(iii) show the retrieved fluorescence images at 200 μm and 360 μm below the surface, respectively. The decrease in fluorescence signal for the maple leaf at 360 μm (figure 6.9(b)(iii)) was due to light scattering from the seven embedded images above it. Upon increasing the read laser power to 360 μW, the fluorescence signal could be recovered as shown in figure 6.9(b)(iv) with a three–fold increase in intensity (figure 6.9(a)).

6.4 Recovery and thermal stability of recorded images

Higher powers of the read laser raise concerns of photo-recovery of the polymer during multiple read cycles. The photo–recovery of the fluorescence signal from the laser–modified region after prolonged exposure to the excitation laser was studied by repeatedly turning on and off the laser with a specific duty cycle. The duty cycle consisted of an *on* time of 30s to record fluorescence from the 3D stack followed by an *off* time of either 1 or 3 minutes. The variation of fluorescence signal recorded during each *on* cycle enabled us to study photo-recovery of the modified polymer. For this study, an array of periodic laser–modified regions was fabricated with each row corresponding to a specific energy in the range of 40 – 200 nJ. The row spacing was 3 μm and the spacing between modified regions in a row was 2.5 μm. A 0.55 NA microscope objective (40X magnification) was used to focus light 300 μm below the PMMA surface. Statistical analysis was

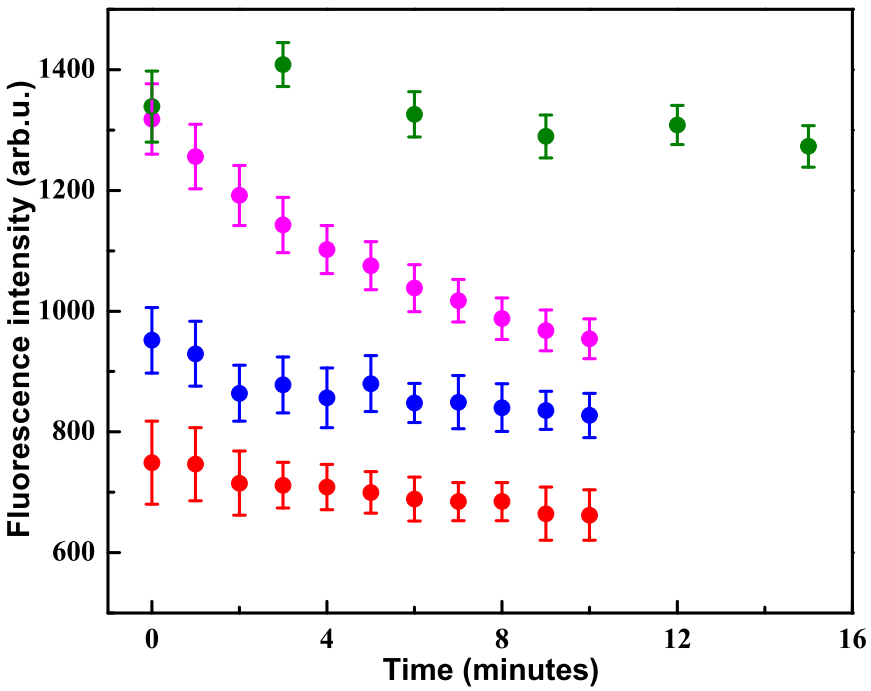

Figure 6.10: Photo-recovery and thermal stability of embedded data. Recovery of fluorescence signal from fs laser-modified polymer using different *on-off* duty cycles of the 488 nm read laser at different powers and detector's sensitivity. The *on* time was fixed at 30s. For fixed *off* time of 1 minute and a sensitivity of 100 V the fluorescence signal was high at 200 μW of read laser power (blue) compared to 100 μW (red) and no degradation with time was observed. However, at high power (340 μW power and sensitivity of 90 V) the fluorescence signal does not recover sufficiently (pink). The recovery is better when the *off* time was increased to 3 minutes (green).

carried by choosing a row of 20 modified regions with a specific energy of 80 nJ. Similar results were obtained at different pulse energies. Recovery of the fluorescence signal from the defects induced by the write laser for different *on-off* duty cycles of the read laser is shown in figure 6.10(a). All measurements were made on the top image layer with different incident powers. In contrast, in figure 6.9 the power delivered to images at different depths is not the same as the incident power due to losses. In all cases the read laser was *on* for 30 seconds. At low powers (100 – 200 μW) there is no appreciable change in the fluorescence signal when the read laser was *off* for a minute. At a higher power of $\sim$ 340 μW and an *off*-time of 1 min there is a decay of the fluorescence signal

with multiple read cycles. Increasing the *off* time to 3 min improved the photo-recovery. The florescence signal did not diminish when the data were read after several days and weeks.

6.5 Thermal degradation

The thermal degradation of the recorded images was performed by annealing the PMMA sample for an hour at a specific temperature in a Barnstead Thermolyne-1400 Furnace. The fluorescence was recorded with the confocal microscope after the annealed sample was cooled to room temperature over several hours. For this study we used an embedded 3-bit image of Albert Einstein fabricated 250 μm below the surface with a 0.9 NA water immersion objective. The laser pulse energy was varied in the range of 25–130 nJ to record the image. From the recorded images, an integrated fluorescence signal was obtained at each temperature and normalized with that of the room temperature. Pearson correlation of the room temperature image with those at other temperatures was obtained using the co-localization tool in Image J. Correlation coefficient of unity corresponds to two identical images while a value of zero corresponds to no overlap between the two images. Environmental effects influence the long-term stability and shelf life of any data storage system. Specifically, thermal stability is crucial for practical implementation [175–178]. Polymer properties are known to thermally degrade and therefore can alter the fluorescence emitted by the ultrafast laser irradiated regions. Figure 6.11(a) shows the correlation coefficient of fluorescence images obtained at different temperatures with respect to that at room temperature. In the temperature range of -80°C to 115°C, the correlation coefficient is close to unity suggesting the images are spatially correlated with similar pixel intensities. Also, shown are fluorescence images

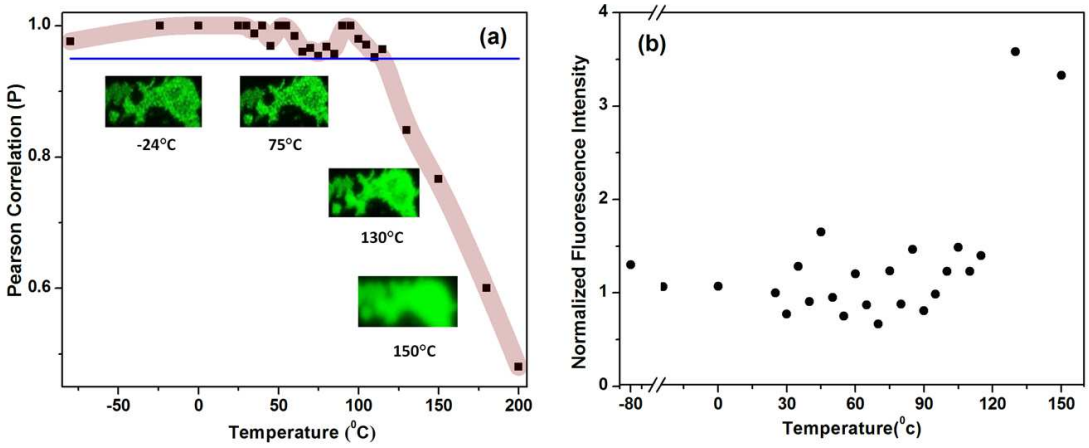

Figure 6.11: (a). Plot of Pearson correlation of images of random pattern at different temperatures relative to the image at room temperature(25°C). (b). shows the variation of integrated fluorescence signal at different temperatures normalized to the image obtained at room temperature.

at different temperatures. Beyond 130°C the image quality degraded with poor spatial resolution even though the fluorescence intensity increased significantly (figure 6.11(a)). In the temperature range of -80°C to 115°C the normalized fluorescence signal, shown in figure 6.11(b), does not vary significantly suggesting the stored data is stable up to the glass transition temperature of PMMA [179]. At temperatures beyond 200° C, close to the melting point, the images are blurred as the modified regions coalesce together. However, the fluorescence does not disappear. So, unlike in some glasses the stored data cannot be erased and rewritten by raising the temperature to glass transition.

6.6 Spectral analysis

The spectral analysis of fluorescence from small volume of the laser-modified region ($\sim$ 10 μm^3) is difficult. We therefore fabricated a grating like structure in PMMA 300 μm below the surface, as described in chapter 3. To comprehend the nature of laser-induced

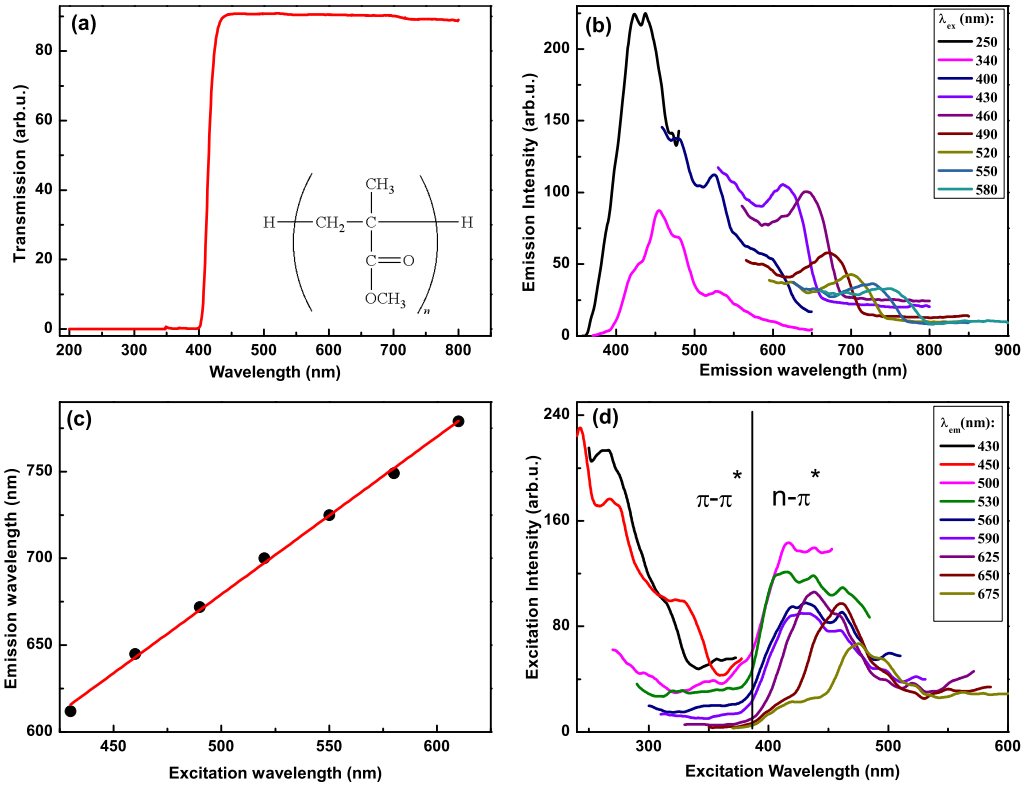

Figure 6.12: Spectral analysis. (a). Transmission spectrum of pristine PMMA (chemical structure shown in inset). (b). Fluorescence (emission) spectra recorded for ultra-fast laser modified PMMA at different excitations covering the entire visible spectrum. (c). the linear red shift of the fluorescence peak (as indicated in b) observed from 400 nm onwards with different excitation wavelengths (d). Excitation spectra of the laser modified PMMA recorded at different fluorescence emission windows. Regions of possible $(n - \pi^*)$, and $(\pi - \pi^*)$ transitions are indicated in the figure, demarcated by a line around 380 nm.

fluorescence and its origin we recorded the transmission, emission and excitation spectra using conventional transmission and fluorescence spectroscopy. The commercially obtained pristine PMMA sample was tested for its spectral purity using a Cary 100 UV-vis absorption spectrometer. Figure 6.12(a) shows the UV-visible absorption spectrum of pristine PMMA (chemical structure is shown in inset of figure 6.12(a)) recorded in transmission mode. No light is transmitted below 400 nm (3 eV photon energy) suggesting additives have been added to the polymer to provide UV protection (note: the bangap of

pure PMMA is 4.58 eV [180, 181]). The embedded UV absorbers/stabilizers, although not disclosed by the manufacturer, typically contain aromatic moieties, carbonyl groups and phenols (specifically, quinone and benzophenone families as well as propionate and benzotriazole derivatives [182–185]. Upon 2-photon excitation these groups lend themselves to photochemical transformations leading to fluorescent molecules that emit light upon excitation. Very low transmittance below 400 nm as observed in the spectrum of unmodified PMMA samples indicates the potential use of more than one type of UV absorbers.

Pristine PMMA does not exhibit fluorescence in the visible spectral range (figure 6.12(a)), while laser-modified PMMA does emit fluorescence. Figure 6.12(b) shows fluorescence emission spectra from laser modified PMMA. Fluorescence emission could be attributed to either the formation of nanoclusters of different sizes [27] or rearrangement of different aromatic moieties upon two-photon absorption that leads to the formation of fluorophores confined in a rigid polymer matrix. The fluorescence intensity not only decreased with increasing excitation wavelength but also shifted to the red-edge of the excitation spectrum.

The previous assumption of the existence of more than one type of stabilizers can be supported by the broad lifetime distribution obtained by Fluorescent Lifetime Imaging Microscope (FLIM) as shown in figure 6.13. One would normally expect that emission from a single compound be independent of the excitation wavelength, following Kasha's rule [186, 187]. Here the marked dependence of emission on the excitation wavelength (red shift shown in figure 6.12(c) is a clear indicator that multiple (single) chromophores (of varying sizes) are involved likely due to the use of UV stabilizers and the formation of diverse emissive products upon high intensity laser excitation. The measured lifetime

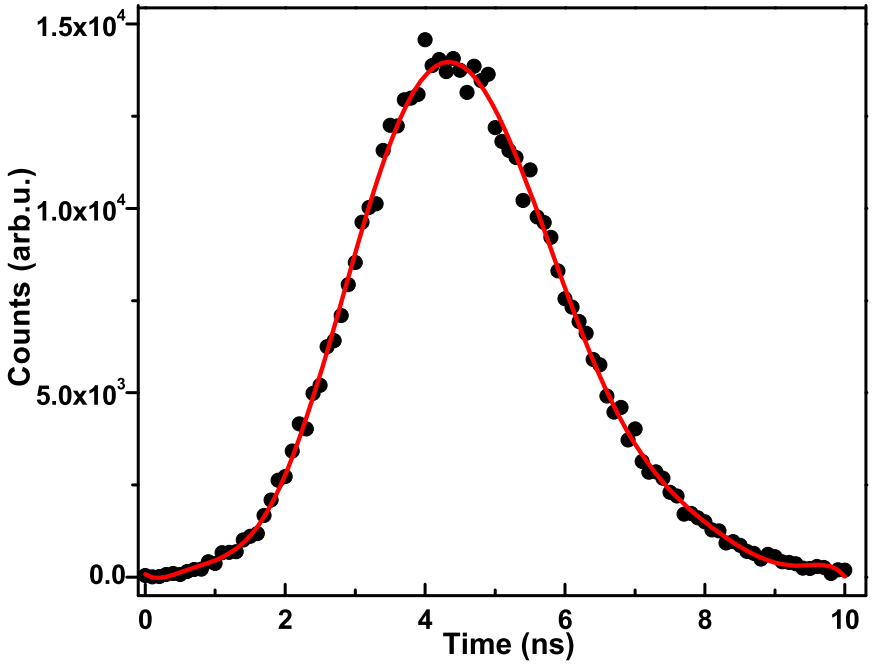

Figure 6.13: Fluorescence lifetime measurement from the ultrafast-laser modified region.

distribution was centered at 4.2 ns with a FWHM of 3.4 ns, too broad to be attributed to a single emitter. The evidence that laser excitation causes similar effects independently of the diverse nature of the polymers is consistent with the photo-degradation of the UV stabilizers, as these molecules are widely employed in the polymer industry. The broad lifetime of the fluorescence signal obtained using FLIM technique also rules out the possibility of Raman scattering.

Figure 6.12(d) shows the excitation spectra recorded for laser modified PMMA. From the fluorescence spectra obtained in figure 6.10(b), we recorded the excitation (absorption) spectrum for each emission. First, two distinct excitation bands could be observed below and above approximately 380 nm. The origin of these bands could be attributed to (n-π^*) and ($\pi - \pi^*$) transitions of fluorophores in aromatic molecules [27, 94, 144, 147]. In literature, maximum excitation around 400 nm was ascribed to the absorption of some

unsaturated aldehyde or ketone groups, that undergo (n-π^*) transition [94,144,147,188]. The energy associated with (n-π^*) transition is lower compared to ($\pi - \pi^*$) transition that typically corresponds to UV absorption below 380 nm [144]. Second, the (n-π^*) bands were found to be shifting with emission from 380 nm onwards as shown in the legend of figure 6.12(d). This feature enables us to use a broad range of read laser wavelengths to retrieve the recorded data. To conclude, laser treated plastics result in the formation of aromatic compounds (fluorophores) that undergo (n-π^*) and ($\pi - \pi^*$) transitions upon suitable excitation.

Standard optical discs (CD and DVD) are made of 1.2 mm thick polycarbonate with a recording area of $\sim$ 100 cm^2. With a 1.4 μm pixel spacing, a single layer of data in the disc holds 25 Gbits with 5-bit encoding. When data is embedded 150 μm below the surfaces the effective thickness available for recording is 900 μm. By tailoring the read laser power and detector sensitivity the number of layers that can be imaged without loss of information can be extended up to 30. Reading the data on both sides of the disc allows one to stack 60 layers with a spacing of 15 μm (each fluorescent bit had a depth of 8 μm due to confocal parameter, (figure 6.6(b)) providing a storage capacity of 0.2 TBytes/disc. Using high NA microscope objective, pixel spacing can be reduced further to 1 μm and with a layer spacing of 10 μm data storage of 0.5 TBytes/disc is feasible.

6.7 Conclusion

Our data storage technique has key advantages. (1) The material need not contain photosensitive molecules to start with – the write laser induces them. (2) Cost effectiveness – commonly available plastics can be used. (3) No special sample preparatory steps

are required compared to other techniques and large discs can be readily available. (4) Adaptable with existing DVD and Blu-ray technology. The power of the read/excitation laser (both 405 and 488 nm) used in our measurements is in the range of 100 μW–1 mW comparable to DVD/Blu–ray. So the read laser requirements are minimal and only the detection mechanism needs to be modified to the confocal configuration. (5) Possesses unique capability of data retrieval with any excitation source in the visible spectrum. (6) The storage discs have long shelf life with operable temperatures in the range of -80°C to 115°C. (7) Since the data is embedded, it is unaffected by humidity. Data storage works in uncontrolled temperature and humidity conditions. Tailoring the glass transition temperature of the polymers by general doping or controlling the residual solvent in polymer can further extend this range. The main drawback of our technique is that the discs are read only.

Chapter 7

Selective cell adhesion on femtosecond laser microstructured PDMS

In this chapter, we show that femtosecond laser irradiation of polydimethylsiloxane enables selective and patterned cell growth by altering the wetting properties of the surface associated with chemical and/or topographical changes. In the low pulse energy regime, the surface becomes less hydrophobic and exhibits a low water contact angle compared to the pristine material. X-ray photoelectron spectroscopy (XPS) also reveals an increased oxygen content in the irradiated regions, to which the C2C12 cells and Rabbit Anti Mouse protein were found to attach preferentially. In the high pulse energy regime, the laser modified regions exhibit super-hydrophobicity and were found to inhibit cell adhesion, whereas, cells were found to attach to the surrounding regions due to the presence of nanoscale debris generated by the ablation process.

7.1 Introduction

Altering the surface properties of biomaterials on the micron scale enables selective and patterned cell growth which plays a crucial role in tissue engineering and biomedical applications such as disease diagnostics, biosensors, and implant union. Often, cell adhesion is strongly influenced by physicochemical properties of substrates. A variety of techniques are used to change the surface properties of a material that are based on altering the surface topography and/or chemistry. Some of these techniques enable controlled and patterned growth of cells. Chemical techniques often involve covalently attaching peptides containing the cell recognition motif, Arginyl-glycyl-aspartic (RGD), to the material via functional groups on the surface that are introduced, among other methods, by physical or chemical treatment [189]. Photolithography, soft lithography [190], self assembled monolayers [191, 192], and micro-contact printing [193, 194] are also used to anchor peptides.

In photolithography technique, a substrate is coated with a photoresist material that has the feature of being modified when it is irradiated with light. The photoresist is exposed to light through a mask to make the desirable pattern. After that, a solvent is used to remove the photoresist. In soft lithography, the photolithography technique is used to make a pattern on soft, elastic material, usually PDMS. This pattern is used later on as a mold to pattern another substrate. In micro-printing technique, a computer-programed pattern is printed on a substrate using cell adhesive liquid droplet [195].

Cell adhesion by surface topography modification alone relies on altering the wettability of a material making it hydrophilic or hydrophobic. More generally, surface modification alters both topographical and chemical properties of the surface. Micro

and nanostructured surfaces with controlled feature dimensions have been mostly fabricated by combining photolithography with wet chemical etching [196, 197] or with dry reactive ion etching [198,199]. Other widely used techniques are plasma treatment [200]. In plasma treatment technique, a high voltage is applied between two anodes, and the resultant plasm by ionizing the gas consists of energetic electrons or ions that can etch the surface of a material.

Most of the previous techniques require clean room, vacuum chamber, and a photoresist material. Direct writing techniques that do not require masks such as ion beam processing [201] and laser ablation [202, 203] have also been used to fabricate micro- and nano-patterns on surfaces. These are clean techniques with no residual chemical components remaining on the material surfaces.

Femtosecond laser ablation has emerged as a promising tool for self-organized and direct fabrication of nano and microstructures on the surface of any material. Unlike excimer laser ablation that is widely used in the majority of biological applications, femtosecond laser processing of materials has unique advantages. Femtosecond lasers concentrate energy in such a short pulse duration that heat cannot be transferred to the surrounding material [14]. Such localized energy deposition causes the material to sublimate into plasma reducing melting, heat-affected, and resolidification regions. This cold ablation process therefore substantially reduces thermal debris and post-processing, and minimizes collateral damage to the surrounding regions. In transparent materials, plasma is initiated by multiphoton absorption thereby enabling deeper penetration into the materials and controlled modification of material properties in 3D [15]. Such an athermal interaction of ultrashort light pulses leads to high precision and repeatable features down to sub-micron dimensions in any transparent dielectric material. The ad-

vantages of femtosecond laser ablation have been exploited in subcellular dissection [204], refractive surgery [205, 206], and all-optical histology of brain tissue [207].

Several studies used femtosecond lasers for microstructuring and patterning of metals, [208] semiconductors [209, 210], and plastic surfaces [208, 211] to investigate cell adhesion and directed cell growth. Structures such as periodic grooves, and arrays of holes and pillars have been fabricated to control cell behaviour (spreading, elongation, localization, and orientation) [212]. However, fewer efforts have been exerted on soft materials. Femtosecond lasers have been used to fabricate 3D micro-patterns in collagen scaffolds [213], enhance cell infiltration in 3D electrospun scaffolds [214], align cells in micro-channels fabricated in biodegradable polymer films [215], and influence cell morphology and growth induced by microspikes in silicone elastomer [216].

We studied the influence of femtosecond laser irradiation on the wetting properties of polydimethylsiloxane (PDMS) surfaces. PDMS is a biocompatible polymer with excellent physical and chemical properties, flexibility, low cost, and ease of fabrication [217]. Biocompatible polymers are widely used in the medical field for orthopedic applications, reconstructive implants [218], intraluminal grafts, stent like devices, catheters, temporary vascular grafts, temporary conduits for peripheral nerve regeneration, and scaffolds. In general, PDMS is a hydrophobic material due to the presence of methyl groups that give the surface a low interfacial free energy [219]. So, cell adhesion is negligible on PDMS surfaces unless surface properties are altered significantly to make it hydrophilic.

In this chapter, we show that at laser pulse energies close to the ablation threshold changes to the surface topography on the micron scale and the chemistry lead to reduced hydrophobicity and preferential cell adhesion in the laser modified regions. Specifically,

we found that adhesion of C2C12 mouse myoblast cells was enhanced by a factor of ∼3 relative to the pristine material. Moreover, this enhancement is more than a factor of 10 when the PDMS surface was initially treated with amphiphilic Pluronic copolymer. However, we found that at laser pulse energies greater than ∼300 nJ (7 J/cm^2), the laser modified regions exhibit superhydrophobicity and cell adhesion is inhibited in the ablation zone. Therefore, our studies suggest two distinct routes to selective and patterned cell growth on a PDMS surface via laser ablation.

7.2 Surface topography

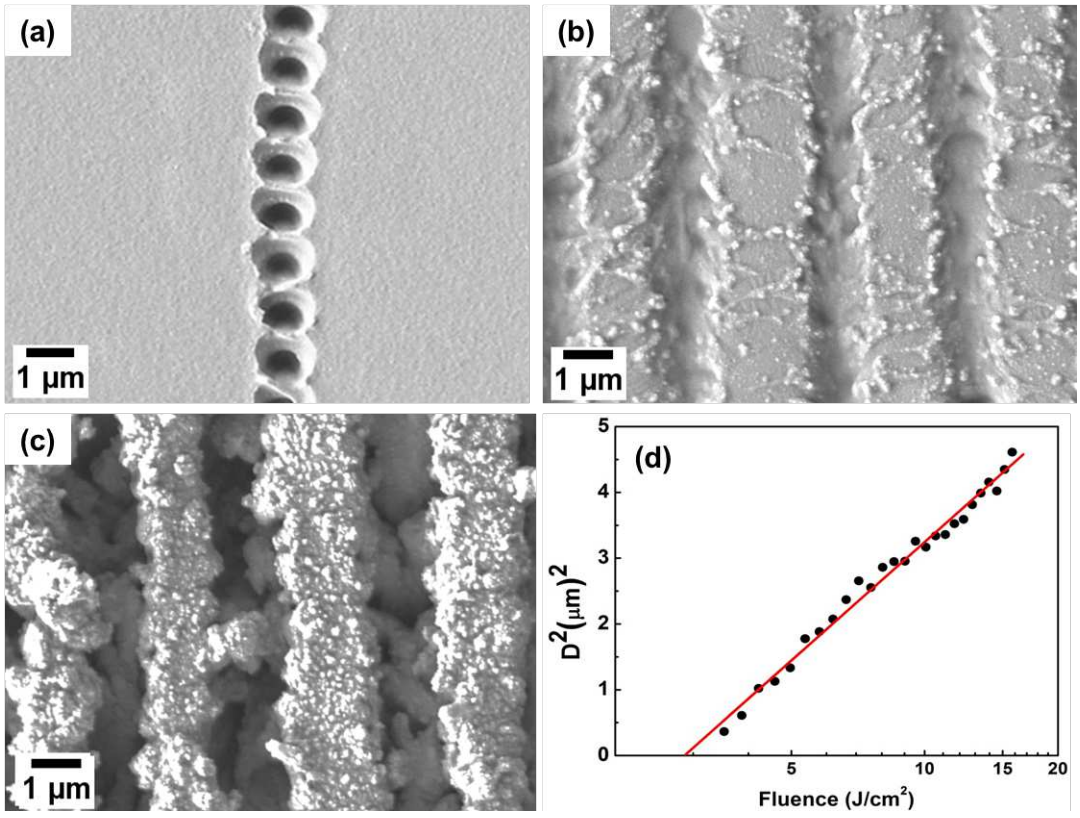

Figure 7.1: (a-c) SEM images of laser modified regions with pulses energy of 110 (2.6 J/cm^2) nJ, 125 nJ (2.9 J/cm^2), and 190 nJ (4.5 J/cm^2), respectively, and spacing of 3 μm. (d) Variation of the size of the laser damaged spot in a single shot ablation with laser fluence.

A pristine PDMS surface is not ideal for cell attachment due to its hydrophobicity [220]. The surface topography and its wetting properties can be altered by irradiating it with a femtosecond laser. The morphology of the laser modified regions is shown

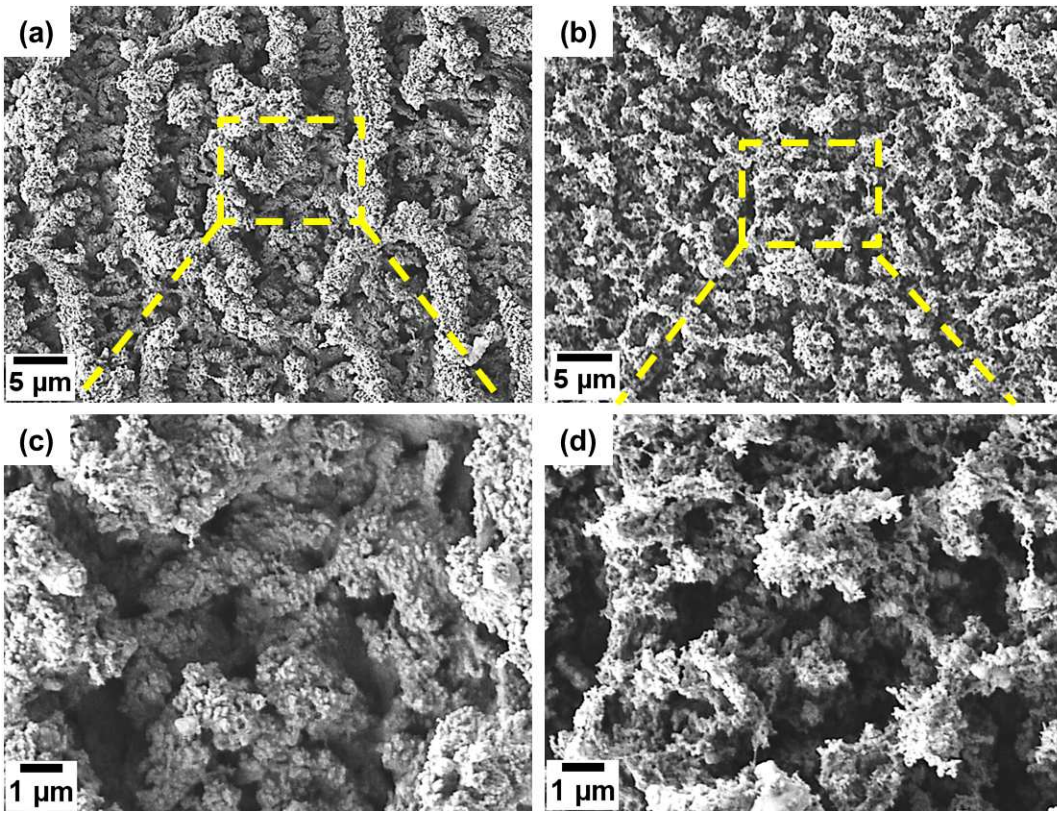

Figure 7.2: SEM of images of laser modified lines on PDMS with a spacing of 3 μm at two different pulse energies 270 nJ (6.3 J/cm^2) (a) and 430 nJ (10 J/cm^2) (b). (c) and (d) are magnified images of (a) and (b), respectively. Laser scan speed was 1 mm/s.

in figure 7.1 and 7.2 for different pulse energies. At low energies close to the ablation threshold (110 nJ corresponding to a fluence of 2.6 J/cm^2), the modified region consists of single file, shallow, sub-micron sized holes/pits with no debris in the surrounding regions (figure 7.1(a). The spacing between the holes is determined by the repetition rate of the laser and the speed with which the sample is moved, and can be changed accurately by varying the latter.

Figure 7.1(b) shows the surface morphology when 125 nJ (2.9 J/cm^2) pulses were

used to ablate periodic lines/grooves with a 3 μm spacing. The grooves are no longer made up of holes when compared with figure 7.1(a) but are rough both at the bottom and the edges. In addition, nanoscale debris are deposited on the nearby unmodified regions. When the pulse energy is further increased to 190 nJ (4.5 J/cm^2) the modified regions become porous figure 7.1(c). The peak laser fluence required to initiate material removal from the irradiated area in PDMS with a single laser pulse is determined by measuring the diameter of the damaged area and plotting its square as a function of the fluence in a semi-logarithmic plot as shown in figure 7.1(d). The intercept of a linear fit to the data with x-axis gives the single-shot ablation threshold of 2.8 J/cm^2 for PDMS, in agreement with the published data in the literature [221]. The ablation threshold decreases with the number of laser pulses due to the incubation effect [38]. In our experiment, all the ablation lines were fabricated by moving the sample at a speed of 1 mm/s. As a result, 3 laser pulses irradiated the sample within the laser focus reducing the ablation threshold to $\sim$ 1.6 J/cm^2.

Figure 7.2 shows SEM images of the laser modified regions at two different high pulse energies. In general, the width of the laser ablated region increases with pulse energy. So, at 270 nJ (6.3 J/cm^2) (left column) the width is increased to an extent that the unmodified region between the periodic lines is deformed figure 7.2(a) and the modified regions start to exhibit porosity figure 7.2(c). The surface consisted of micro and nanometer–sized aggregates. As the pulse energy is further increased to 430 nJ (10 J/cm^2) (right column), the entire surface becomes porous consisting of sub-micron sized aggregates. Such a surface should lead to increased hydrophobicity due to the presence of air trapped inside the nanopores that significantly reduces the contact area of a water droplet and hence the surface energy at the interface – the lotus effect.

In the lotus effect, the surface of the louts leaf is highly-water-repellent (superhydrophobic). A falling water droplet on such a surface rolls down or bounces off as a result of the high contact angle between the droplet and the surface, usually ¿ 140° degree. The high contact angle is due to the roughness of the superhydrophobic surface, which consists of a combination of micro and nanostructures. Such a microscopic structures result in low surface energy, leading to a sphere formation of the water droplet and minimizing the contact area between the droplet and surface [216, 222].

7.3 Contact angle measurements

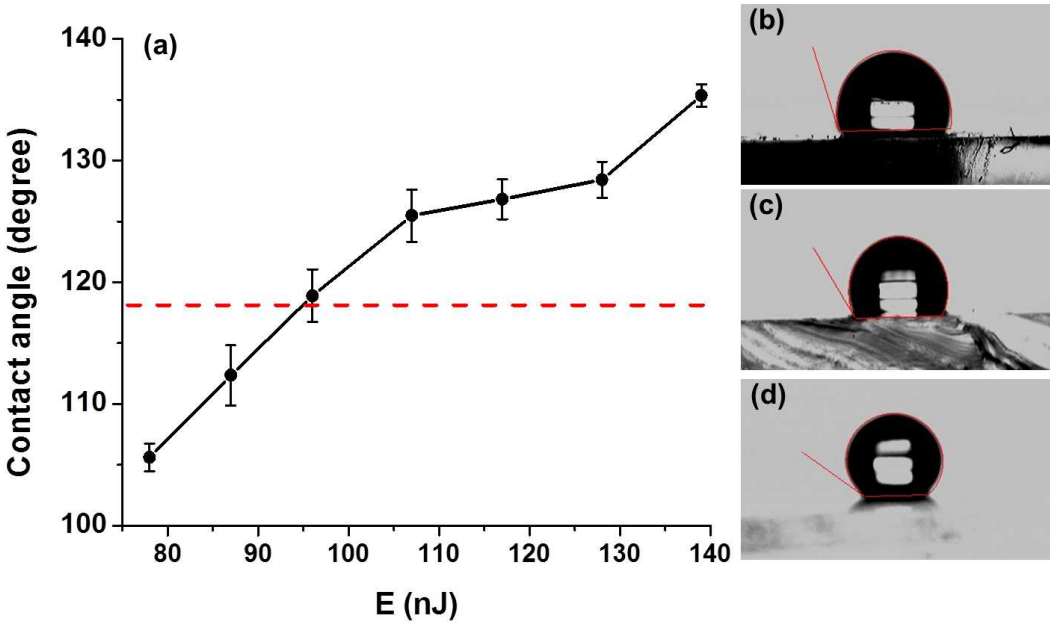

Figure 7.3: Contact angle measurements. (a) Contact angle as a function of laser energy. (b), (c), and (d) Water drop images for: 78 nJ (1.8 J/cm^2), unmodified PDMS, and 140 nJ (3.2 J/cm^2), from the top to the bottom, respectively. The red dashed line in (a) is the contact angle for pure PDMS.

Wettability of the laser modified regions was studied by contact angle measurement using VCA-optima system. Large areas of 1.5 mm × 1.5 mm were fabricated on the

PDMS surface under identical conditions used to study cell adhesion. The water contact angle was measured on pristine and laser modified regions 5 seconds after releasing 0.2 μl droplet from the syringe. A high resolution camera captured the image and was analyzed using the image analysis software associated with the system. The measurements were repeated three times for each modified region.

Wettability of the laser modified surface was studied by measuring the contact angle as shown in figures 7.3(a,b,c, and d) for different laser pulse energies. The dashed line in figure 7.3(a) represents the contact angle of the unmodified PDMS surface; the corresponding water drop image is shown in figure 7.3(c). The contact angle increases with the pulse energy [223]. It is lower than the unmodified PDMS at pulse energies close to the ablation threshold resulting in increased wettability as indicated in figure 7.3(b). For pulse energies greater than $\sim$ 100 (2.4 J/cm^2) nJ, the laser modified surface becomes more hydrophobic reaching that of a lotus leaf by about 150 nJ (3.5 J/cm^2) as indicated in figure 7.3(d). As the energy was increased further, the surface became superhydrophic; the contact angle measurements were not feasible because the water droplet repelled from the surface. Superhydrophobicity of femtosecond laser fabricated surfaces has also been demonstrated in metals [224–227], semiconductors, [228, 229] and polymers [230–232].

7.4 Chemical changes to modified PDMS

In addition to topographical changes to the surface, any chemical changes induced by the laser will also influence the wetting properties of the material. Laser ablation can alter the chemical nature of an irradiated surface as it involves breaking of chemical bonds and forming new ones. The surface chemistry of laser irradiated PDMS, investigated

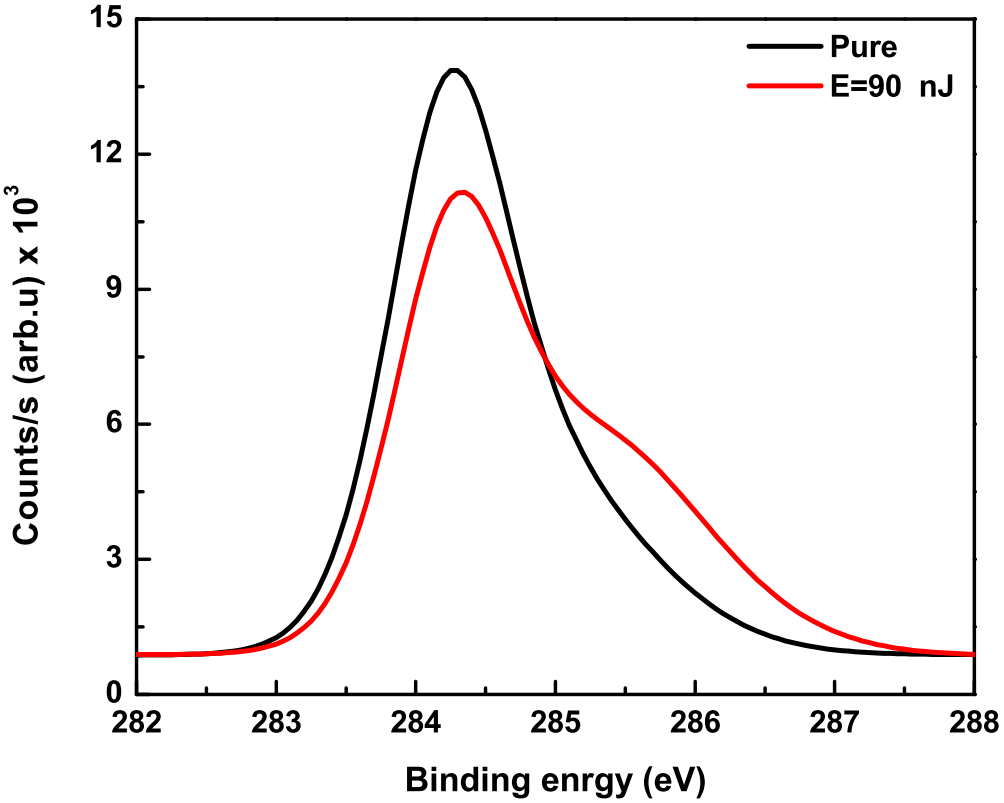

Figure 7.4: XPS measurement of a pure PDMS (black) and laser modified region (red) (90 nJ (2.1 J/cm^2)) as a function of binding energies. Line spacing and laser writing speed were 3 μm and 1mm/s, respectively.

by XPS spectroscopy, is shown in figure 7.4, where the intensity of carbon 1s peak is plotted as a function of the binding energy for pristine PDMS (black), and laser modified regions irradiated (in an air environment) by pulse energies of 90 nJ (2.1 J/cm^2) (red). To compensate for charging effect the energy scale was corrected by adjusting the oxygen 1s component to 532 eV. A least square fitting routine with mixed Gaussian/Lorentizain was used for the components along with a linear background. The atomic concentration of carbon in pristine PDMS was found to be 46% ±2% compared to the theoretical value of 50%. The peak energy of C 1s is at 284.3 eV, in good agreement with the literature [233]. We observed a weak high-energy tail in the C 1s peak. A two-component fitting

resulted in peaks at 284.3 and 285.1 eV with 63.5 % and 36.5% area respectively.

For the laser modified regions, we observed a decrease in C 1s concentration with laser pulse energy while oxygen (O 1s) concentration increased. Moreover, both C and Si peaks (not shown) broadened towards higher binding energies as the laser pulse energy was increased. Compared to pristine PDMS, the C 1s peak of a 90 nJ (2.1 J/cm^2) laser-modified region exhibited a decrease (increase) in the concentration of the peak at 284.3 eV (285.4 eV) from 63.5% to 48.5% (36.5% to 51.5%). As the laser pulse energy was increased, the concentration of the C 1s peak at 284.3 eV continued to decrease while the high energy tail was extended further. Three-component fitting resulted in peaks at 284.6, 286, and 288.4 eV, respectively. In the literature, the peak at 288.4 eV is associated with the formation of C=O bond. This is also in agreement with our recent observations of excitation and EDS spectra [27]. As a result, the surface layer is enriched in oxygen due to the unpaired bonds leading to a more hydrophilic surface. This effect is similar to plasma treatment [234,235] and UV irradiation [119] of surfaces. Therefore, we can conclude from our results that the change in wetting properties of femtosecond laser irradiated PDMS at pulse energies close to the ablation threshold is due to a combination of topographical and chemical changes induced on the surface.

7.5 Protein adhesion

The influence of laser pulse energy on the adsorption of rabbit anti mouse secondary antibody protein to the microstructured PDMS surface is shown in the confocal image of figure 7.5(a), taken 30 minutes after protein seeding. A set of 100 lines were fabricated with a spacing of 10 μm and the pulse energy was increased gradually between successive lines in steps of 6 nJ from left to right. Protein adsorption on the untreated PDMS was

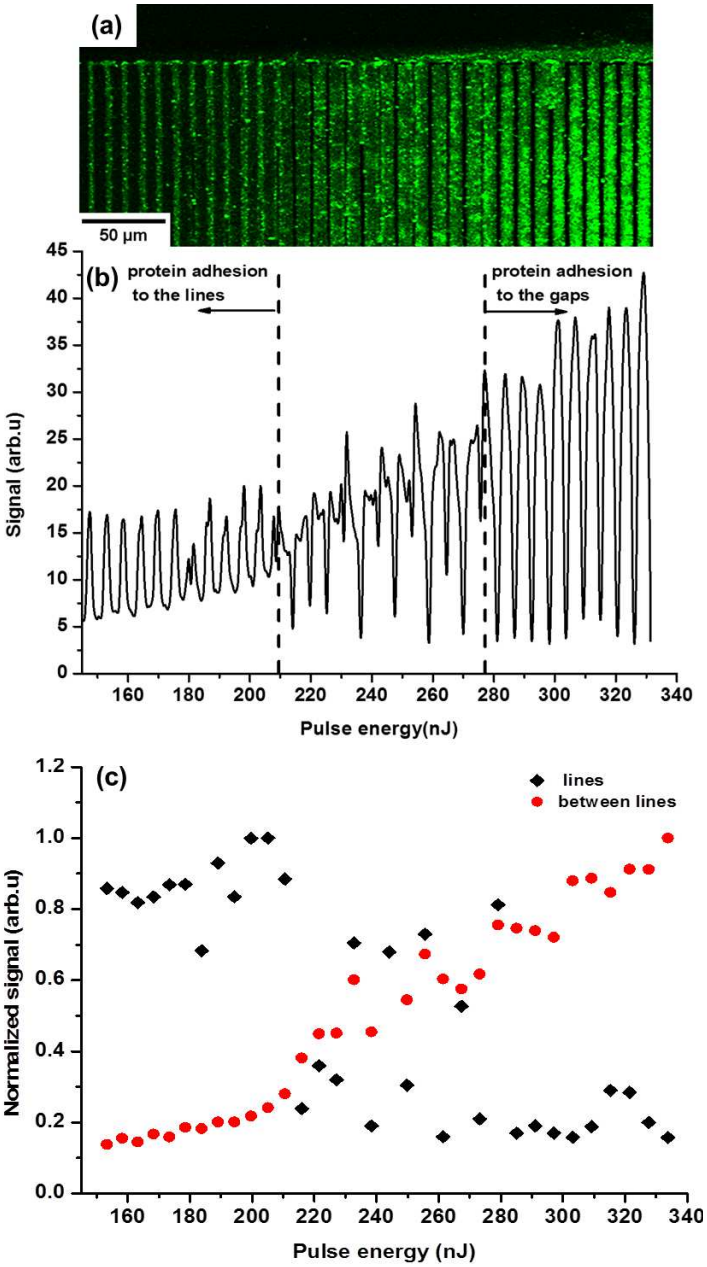

Figure 7.5: (a) Confocal fluorescence image of rabbit anti mouse secondary antibody protein on an array of lines fabricated with increasing pulse energy from the left to the right. Line spacing is 10 μm, and writing speed is 1 mm/s. Energy variation between successive lines is 6 nJ. Lowest (highest) energy to the left (right) is 170 nJ (2.6 J/cm^2) (330 nJ (7.7 J/cm^2). (b) Intensity scan corresponds to the lines and area between lines in (a). (c) Normalized intensity change of the fluorescence signal from lines (black) and area between lines (red) as a function of pulse energy.

negligible due to its hydrophobic nature (top region of the image). In the energy range of 78 – 220 nJ ((1.8 – 5.1)J/cm^2), protein adsorption to the laser-modified regions was enhanced (left region of the image) due to topographical and chemical changes discussed above. Similar enhancement of protein binding has been recently observed on femtosecond laser ablated PMMA surfaces [211]. We also found that there is an apparent energy threshold of $\sim$ 78 (1.8 J/cm^2) nJ below which florescence signal was not observed, suggesting there is no morphological or chemical changes to the surface to increase protein binding at sufficiently low pulse energies (not shown).

For energies higher than 280 nJ (6.6 J/cm^2), protein adsorption is inhibited on the laser modified regions due to superhydrophobicity. However, presence of nanoscale debris in the gap between the laser modified lines enhances surface adsorption of the protein (right region of the image). This can be seen in the line scan of the fluorescence signal from left to right in figure 7.5(b). This suggests adhesion can be controlled by adjusting the relative area fraction of laser structured and non–structured domains, as was demonstrated recently in PDMS [236]. Moreover, there exists a narrow intermediate energy range, approximately between 220 and 280 nJ ((5.1 - 6.6) J/cm^2), where the protein was adsorbed on both the modified ablation lines and the intervening unmodified gap regions (due to nanoscale debris generated by the ablation process), as shown in the central portion of the image in figure 7.5(a,b).

The protein attachment in different parts of the laser modified region is summarized in figure 7.5(c), which shows the fluorescence intensity from the modified (unmodified) regions as black diamonds (red circles). At low energies the normalized fluorescence signal from the protein on the modified regions is significantly higher than in the unmodified region. This behaviour is reversed when the pulse energy is increased beyond

280 nJ (6.6 J/cm^2). Hence, two distinct protein adsorption regimes can be identified - an affinity to the laser modified regions at low pulse energies and an aversion at high pulse energies.

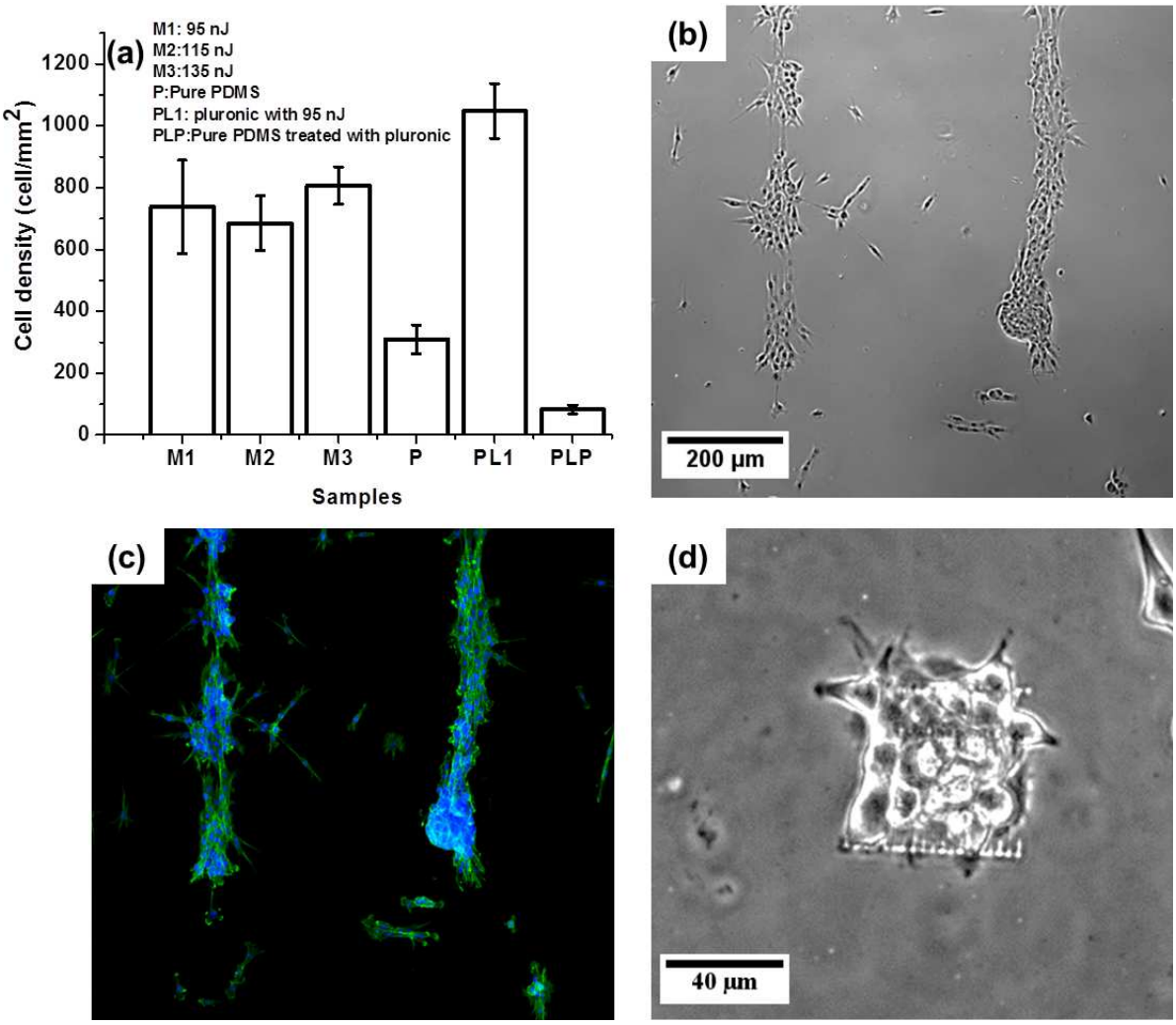

Figure 7.6: Selective growth of C2C12 mouse myoblasts cells on laser patterned PDMS surface. (a) Cell density on the pure and modified regions at three energies, 95 nJ(2.2 J/cm^2), 115 nJ (2.7 J/cm^2), and 135 nJ (3.1 J/cm^2). PLP and PL1 indicate a pure pluronic treated PDMS and modified with pulse energy of 95 nJ (2.2 J/cm^2). (b), (c) phase-contrast and epifluorescence images of cells attached to two thin strips of laser modified regions of width 60 μm, separated by 500 μm, respectively. (d) Phase-contrast image of cells on 60 $\times$ 60 μm^2 square modified region. Pulse energy was 110 nJ (2.6 J/cm^2) and the laser was raster scanned at a speed of 1mm/s and spacing of 3 μm.

7.6 Cell adhesion

We used these two regimes to study adhesion of C2C12 mouse myoblast cells on femtosecond laser modified PDMS. One-way ANOVA followed by Tukey post-hoc analysis was applied to compare the cell density on the modified and unmodified regions for three samples that were patterned under identical conditions. After 72 hrs the number of cells on the modified regions were counted using ImageJ software. All statistical results are presented in average values ± Standard Error (SE) and they were considered significant with a P-value below 0.05.

Figure 7.6(a) shows the cell density studies on three PDMS samples modified with energies of 95 (2.2 J/cm^2), 115 (2.7 J/cm^2), and 135 nJ (3.1 J/cm^2) (labelled M1, M2, and M3 respectively), as well as on pristine PDMS (labelled P). Statistical analysis reveals that the cell density on the modified regions was enhanced by a factor of ∼3 relative to pure PDMS surface with a P-value below 0.05. Also shown is the cell density on PDMS treated with Pluronic copolymers and then modified with an energy of 95 nJ (labelled PL1). In this case, the relative enhancement of cell adhesion between laser modified and unmodified Pluronic treated PDMS (labelled PLP) is greater than a factor of 10 with a P-value below 0.05. We use these rather large differences in cell attachments to achieve selective and patterned cell growth, as shown in figure 7.6(b-d), 72 hours after the cells were seeded. Several thin stripes of laser modified regions were fabricated with a pulse energy of 110 nJ (2.6 J/cm^2). Each region consisted of 20 lines, each resembling figure 7.1(a), with a spacing of 3 μm. Figures 7.6(b,c) show a phase-contrast and epifluorescence images of selective cell attachment, respectively. Figure 7.6(d) shows a phase-contrast image of selective cell attachment to a square shaped modified region with an area of 60 × 60 μm^2.

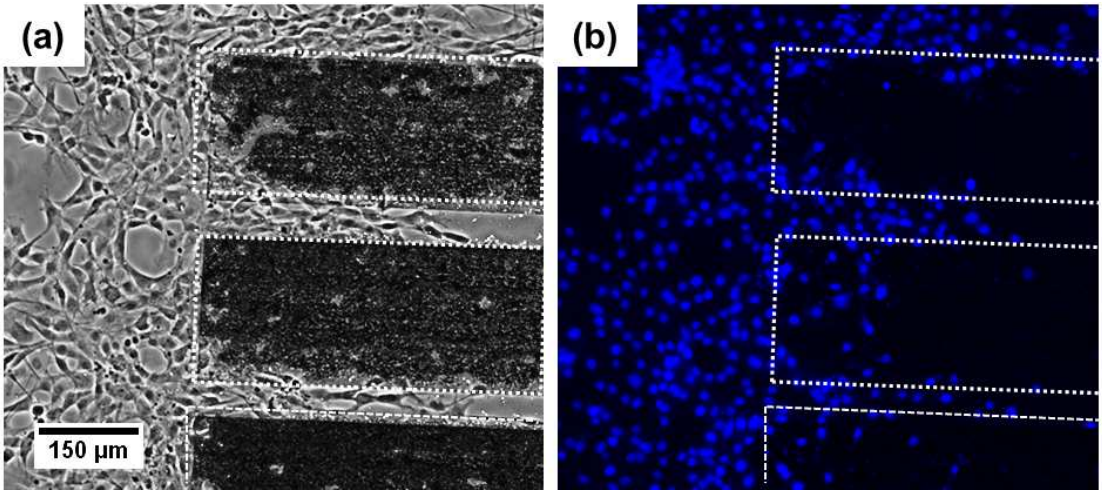

Figure 7.7: Cell response on superhydrophobic and surrounding regions on PDMS. Superhydrophobic regions were fabricated with a pulse energy of 430 nJ (10 J/cm^2). (a) Phase contrast image. (b) Epifluorescence image.

Figure 7.7 shows cell response to superhydrophobic ablated and surrounding non–ablated regions on PDMS. Three 250 × 1000 μm^2 rectangular superhydrophobic regions were fabricated by raster scanning the PDMS sample with a speed of 1 mm/s and line spacing of 3 μm. The laser pulse energy was fixed at 430 nJ (10 J/cm^2). Cells were seeded uniformly on the surface and after 72 hours cell attachment was found to be inhibited on the superhydrophobic regions. The white dashed lines in figure 7.7 define the boundary of the superhydrophobic regions. Cell attachment on the surrounding unmodified regions was found to be enhanced, likely due to the presence of debris from the ablation process that alters the topography of the pristine PDMS. Laser induced super-hydrophobicity therefore provides a second alternative to achieve selective and controlled cell growth.

A specific pattern can be achieved by laser treating the rest of the surface with high pulse energies to induce superhydrophobicity so that cell attachment occurs only on the non–ablated regions, due to the presence of nanoscale debris from the ablation process-

ing of the superhydrophobic regions. Similar superhydrophobic surfaces were fabricated on silicon by femtosecond laser ablation to create spikes that suppressed proliferation of fibroblasts but not neuroblastma cells [209, 237]. Bacterial retention on femtosecond laser fabricated titanium surfaces was also recently investigated wherein spherical *S. aureus* cells were found to successfully colonize the superhydrophobic surfaces, while rod shaped *p. aeriginosa* cells did not attach to the surfaces [238]. Chemically modified superhydrophobic surfaces on polystyrene and PDMS showed similar results, wherein certain types of cells were found not to proliferate, [239], while others such as intermediate size embryonic stem cells demonstrated enhanced proliferation [240].

7.7 Conclusion

Most existing procedures for patterned cell growth usually require special techniques such as plasma etching and photolithography and/or elaborate chemical modification [241, 242]. In contrast, our results demonstrate the versatility of femtosecond laser processing of biomaterials as a direct write technique that does not require any post-processing, to achieve spatially selective patterned cell growth. The two distinct regimes of selective cell growth offered by our technique provides the flexibility to control interfacial properties. By integrating with the 3D capability of femtosecond laser structuring of transparent materials, active guiding of cell growth in complex 3D scaffolds to promote cell infiltration and differentiation in spatially controlled volumes within the scaffold may be possible in the near future.

Chapter 8

Conclusion and future outlook

8.1 Summary

Complete understanding of the fs-pulse interaction with dielectrics enables researchers to achieve material modification in a controlled fashion. The manipulation of material properties on the micro and nanoscale using fs-laser pulses is a promising technology in integrated optics, nanophotonics, biomedicine, and quantum optics. Despite the effort that has been made since the advent of fs–laser technology, there is still much to investigate. For example, the mechanism responsible for the optical breakdown in the transparent dielectric is not completely understood.

In this thesis, we have presented our contributions to the field of micro and nanostructuring of polymer properties by fs–laser pulses. We have focused on the interaction of fs–laser pulses with polymers and its applications in the technology of data storage devices and selective cell growth on the surface of biocompatible polymeric materials such as PDMS. This effort has led to several publications on the optical breakdown of polymers, localized nanoclusters formation, and their applications. This chapter offers

a review of the key points presented in this thesis and suggestions for new experiments that can be taken into account for future research in this field.

Optical breakdown of PDMS and PMMA when exposed to fs–laser pulses was investigated using transmission measurements. It was found that at the optical breakdown threshold the transmission abruptly plummets and clamps at a value of 20%. This behaviour is the opposite of that for glass. It was also found that the optical breakdown depends on the pulse energy as well as the number of pulses. A late probe pulse with very low energy was sent through the modified regions, and it was shown that the transmission is dropped by $\sim 60\%$, indicating that the material exposed to fs-laser pulses was becoming absorptive. Those modified regions were carbonized, and they exhibited a $\sim$ 40% reduction in the optical band gap as it was revealed by the absorption spectroscopy. Such a reduction in the optical band gap indicated the formation of nanoclusters within the modified regions, less than 1 KHz.

In this thesis, we also show that carbonaceous and siliconaceous clusters were formed locally and confined to the modified region on a micron scale, when PDMS was irradiated by intense fs-laser pulses. Micro-Raman studies also indicated the formation of quasi-crystalline silicon nanoclusters, which vary in size based on the incident laser fluence. The modified region exhibited broad photoluminescence with an intensity that increases with laser fluence. A red-edge excitation effect in PDMS was observed, wherein the fluorescence from the laser–modified regions shifted to longer wavelengths as the excitation wavelength was increased to the red edge of the absorption band. Excitation spectra revealed four distinct absorption bands that contributed to the emission from the laser-modified region; two of each absorption bands were ascribed to each of the carbonaceous and siliconaceous clusters.

The nanoclusters have unique fluorescence properties and are confined to the micron–scale regions. The presence of such low dimension material was utilized to demonstrate a novel, simple, and inexpensive method to store data in 3D in commonly available plastics. This work was based on the utilization of the fs-laser pulses to induce fluorescence centers in a localized region, representing a bit. Upon excitation by a read laser, each bit emitted fluorescence with intensity that varied linearly with the energy of the laser pulse used to record the bit. By assigning different grey levels to the fluorescence signal, intensity multi-level data was encoded in each bit. This technique has the capability to transform the standard DVD/Blu–ray disc made of polycarbonate into a high-density storage disc with capacities as high as 0.5 TBytes. The only limitation of this technique is that the fluorescence signal is decreased with the depth at which the data were encoded. However, this limitation can be eliminated by increasing the sensitivity of the detector used in the read system.

In this thesis, we also show that when the fs-laser pulse is focused on the surface of the polymeric materials such as PDMS, the wetting properties are to change. Using this quality, a single-step process was carried out to achieve patterned cell growth on a biocompatible surface of PDMS by altering chemical and topographical properties of the surface using a femtosecond laser. Selective and patterned growth of C2C12 mouse myoblast cells was achieved by nano/microstructuring the surface in two different ways. At low laser pulse energies, cells attached to the laser-modified regions because the modified regions became more hydrophilic than the pure ones. However, at high pulse energies, the laser irradiated regions exhibited super-hydrophobicity and cell attachment was inhibited. Enhanced cell adhesion was increased by a factor of 12 relative to the pristine material when the PDMS surface was initially treated with pluronic.

8.2 Future outlook

In the whole work related to this thesis, there are still open questions that need to be addressed. For the nonlinear absorption in chapter 4, although the step–function like behaviour of the transmission seems to be a characteristic feature of all polymers, a similar study could be conducted using other polymeric materials such as PC, PEEK, polyimide and so on. Also, to understand what mechanism is responsible for the abrupt drop in the transmission, time-resolved measurements should be carried out. The time scale at which the sudden drop takes place can be determined by the pump and probe technique. Knowledge of abrupt fall time helps in understanding the mechanism behind it. For instance, fast change in the transmission of the probe pulse could be attributed to fast phenomena, such as bond breaking and chemical reactions, which occur in the picosecond time scale. However, if the drop in the probe transmission is because of the formation of a new phase of a material, it will appear at a longer time(ns).

In the work related to nanocluster formation in chapter 5, we have reported that the fluorescence peak of the modified region shifts according to the excitation wavelengths. This could be due to the variation of cluster sizes within the modified region. So, the effect of the laser parameters such as fluence, pulse duration on the size and shape of the cluster is worthy of consideration. The effect of those parameters on the position of the emission peak would be useful information in this field. Such studies can be conducted by studying the shift in the florescence peak using a confocal microscope. Such a study would help in the control of the size and shape of the nanoclusters so that they can be used in applications.

In the work related to the data storage device, the future focus is to increase the capacity of 3D data storage using our technique. This will be fulfilled by looking for the

right material and choosing the right laser parameters. We have tested some polymers, such as PMMA, PC, PDMS, and PS. We were able to assign 32 grey levels from the fluorescence signal, which corresponds to 5 bits. Looking for a material that has a wide florescence dynamic range will increase the grey levels, allowing more data to be stored. In addition, using shorter wavelengths for the writing process, such as 400 nm, would minimize the size of the pixel. For example, a pixel size of 500 nm gives us the ability to store 2 TBit/cm^3. Our technique could also be repeated with a structured beam, such as the Bessel beam. The Bessel beam is a diffraction free beam for which the spot size is smaller than that of the Gaussian beam. This enables us to minimize the pixel size more, allowing to store much more data. Furthermore, an advance in technology and a new era in data storage could be born by merging our technique with that of 3D holography. By replacing continuous lasers that are used currently in the holography technique with fs-laser, we could increase data storage to tens or hundreds of Tera Bytes.

The future focus in the selective cell growth work, presented in chapter7, is to control the cell attachment such that we have a patterned cell growth. Though femtosecond laser pulses are capable of modifying the wetting properties of the surface to be hydrophilic or superhydrophobic, the experiment needs more control. We have reported that the debris ejected from the ablated area affects the cell adhesion. This is a drawback that makes the experiment uncontrollable. One way to avoid that is to modify the bottom surface of a material. In this experiment, the beam goes through the sample, and it is focused on the bottom surface. By doing so, the material will be ejected in forward directions, eliminating the debris effect. The other experiments that could be pursued in this field would be to study the mechanism responsible for the change of the wetting properties of the modified regions, especially the mechanism responsible for the superhydrophobicity

exhibited by the modified region with higher pulse energies. One way to do this is to coat the surface with a suitable material that eliminates any effect of the surface chemistry.

The research presented in this thesis focuses on the micro and nanostructuring of polymers by fs–laser pulses. It contributes to our knowledge of the optical breakdown of polymers, the nature of the new phase of a material formed with the modified regions, and the applications related to the new localized change in the material properties. The study of interaction of fs–laser pulses with polymers is a field with the potential for much discovery in the near future. The physics of optical breakdown, modification, and ablation of dielectrics is still unresolved. Furthermore, new applications, especially in photonics and biomedicine, will no doubt lead to new research in this field.

Bibliography

[1] P. Gangopadhyay, R. Kesavamoorthy, K. G. M. Nair, and R. Dhandapani, "Raman scattering studies on silver nanoclusters in a silica matrix formed by ion-beam mixing," *J. Appl. Phys.*, vol. 88, no. 9, p. 4975, 2000.

[2] J. Wang, F. Zhu, B. Zhang, H. Liu, G. Jia, and C. Liu, "Photoluminescence and reflectivity of polymethylmethacrylate implanted by low-energy carbon ions at high fluences," *Appl. Surf. Sci.*, vol. 261, pp. 653–658, Nov. 2012.

[3] Z. Mbhele, M. Salemane, C. Van Sittert, J. Nedeljkovic, V. Djokovic, and A. Luyt, "Fabrication and characterization of silver-polyvinyl alcohol nanocomposites," *Chemistry of Materials*, vol. 15, no. 26, pp. 5019–5024, 2003.

[4] A. Heilmann, *Polymer films with embedded metal nanoparticles*, vol. 52. Springer Science & Business Media, 2013.

[5] S. Hayashi, "Photoluminescence spectra of carbon clusters embedded in SiO_2," *Jpn. J. Appl. Phys.*, vol. 32, pp. L274–L276, 1993.

[6] I. Antonova, A. Cherkov, V. Skuratov, M. Kagan, J. Jedrzejewski, and I. Balberg, "Low-dimensional effects in a three-dimensional system of Si quantum dots modified by high-energy ion irradiation.," *Nanotechnology*, vol. 20, no. 18, p. 185401, 2009.

[7] L. Khriachtchev, M. Räsänen, and S. Novikov, "Laser-controlled stress of Si nanocrystals in a free-standing Si/SiO_2 superlattice," *Applied physics letters*, vol. 88, no. 1, 2006.

[8] M. Epifani, C. Giannini, L. Tapfer, and L. Vasanelli, "Sol–gel synthesis and characterization of Ag and Au nanoparticles in SiO_2, TiO_2, and ZrO_2 thin films," *Journal of the American Ceramic Society*, vol. 83, no. 10, pp. 2385–2393, 2000.

[9] H. Ou, T. P. Rørdam, K. Rottwitt, F. Grumsen, A. Horsewell, and R. W. Berg, "Ge nanoclusters in PECVD-deposited glass after heat treatment and electron-beam irradiation," *Applied Physics B*, vol. 87, no. 2, pp. 327–331, 2007.

[10] H. Ou, T. P. Rørdam, K. Rottwitt, F. Grumsen, A. Horsewell, R. W. Berg, and P. Shi, "Ge nanoclusters in PECVD-deposited glass caused only by heat treatment," *Applied Physics B*, vol. 91, no. 1, pp. 177–181, 2008.

[11] G. Rizza, P. E. Coulon, V. Khomenkov, C. Dufour, I. Monnet, M. Toulemonde, S. Perruchas, T. Gacoin, D. Mailly, X. Lafosse, C. Ulysse, and E. a. Dawi, "Rational description of the ion-beam shaping mechanism," *Phys. Rev. B*, vol. 86, p. 035450, July 2012.

[12] K. M. Davis, K. Miura, N. Sugimoto, and K. Hirao, "Writing waveguides in glass with a femtosecond laser," *Optics letters*, vol. 21, no. 21, pp. 1729–1731, 1996.

[13] A. M. Alshehri, S. Hadjiantoniou, R. J. Hickey, Z. Al-Rekabi, J. L. Harden, A. E. Pelling, and V. R. Bhardwaj, "Selective cell adhesion on femtosecond laser-microstructured polydimethylsiloxane," *Biomedical Materials*, vol. 11, no. 1, p. 015014, 2016.

[14] B. C. Stuart, M. D. Feit, S. Herman, A. M. Rubenchik, B. W.Shore, M. D. Perry, "Nanosecond-to-femtosecond laser-induced breakdown in dielectrics," *Phys. Rev. B*, vol. 53, pp. 1749–1761, Jan 1996.

[15] C. B. Schaffer, A. Brodeur, and E. Mazur, "Laser-induced breakdown and damage in bulk transparent materials induced by tightly focused femtosecond laser pulses," *Measurement Science and Technology*, vol. 12, no. 11, p. 1784, 2001.

[16] D. Du, X. Liu, G. Korn, J. Squier, and G. Mourou, "Laser-induced breakdown by impact ionization in SiO_2 with pulse widths from 7 ns to 150 fs," *Applied physics letters*, vol. 64, no. 23, pp. 3071–3073, 1994.

[17] L. Jiang and H.-L. Tsai, "A plasma model combined with an improved two-temperature equation for ultrafast laser ablation of dielectrics," *Journal of Applied Physics*, vol. 104, no. 9, p. 093101, 2008.

[18] J. Chen, D. Tzou, and J. Beraun, "A semiclassical two-temperature model for ultrafast laser heating," *International Journal of Heat and Mass Transfer*, vol. 49, no. 1, pp. 307–316, 2006.

[19] R. Thomson, C. Leburn, and D. Reid, *Ultrafast Nonlinear Optics*. Springer, 2013.

[20] B. Ellis and R. Smith, *Polymers: a property database*. CRC Press, 2008.

[21] B. E. Saleh and M. C. Teich, *Fundamentals of photonics*, vol. 22. Wiley New York, 1991.

[22] S. Mao, F. Quéré, S. Guizard, X. Mao, R. Russo, G. Petite, and P. Martin, "Dynamics of femtosecond laser interactions with dielectrics," *Applied Physics A*, vol. 79, no. 7, pp. 1695–1709, 2004.

[23] J. Reif, "Basic physics of femtosecond laser ablation," in *Laser-Surface Interactions for New Materials Production*, pp. 19–41, Springer, 2010.

[24] M. Feit, A. Komashko, and A. Rubenchik, "Ultra–short pulse laser interaction with transparent dielectrics," *Applied Physics A*, vol. 79, no. 7, pp. 1657–1661, 2004.

[25] M. Lenzner, J. Krüger, S. Sartania, Z. Cheng, C. Spielmann, G. Mourou, W. Kautek, and F. Krausz, "Femtosecond optical breakdown in dielectrics," *Physical Review Letters*, vol. 80, no. 18, p. 4076, 1998.

[26] J. Krüger and W. Kautek, "Ultrashort pulse laser interaction with dielectrics and polymers," in *polymers and light*, pp. 247–290, Springer, 2004.

[27] A. Alshehri, K. Deepak, D. Marquez, S. Desgreniers, and V. Bhardwaj, "Localized nanoclusters formation in PDMS upon irradiation with femtosecond laser," *Optical Materials Express*, vol. 5, no. 4, pp. 858–869, 2015.

[28] A. Baum, P. J. Scully, W. Perrie, M. Sharp, K. G. Watkins, D. Jones, R. Issac, and D. A. Jaroszynski, "NUV and NIR femtosecond laser modification of PMMA," *Proc. of LPM2007, University of Vienna*, 2007.

[29] H. Shin, M. N. O'Sullivan-Hale, H. J. Chang, and R. W. Boyd, "Sub-Rayleigh Lithography Using a Multiphoton Absorber," in *International Conference on Quantum Information*, p. JWC33, Optical Society of America, 2007.

[30] L. Keldysh, "Ionization in the field of a strong electromagnetic wave," *Zh. Eksperim. i Teor. Fiz.*, vol. 47, 1964.

[31] E. G. Gamaly, "The physics of ultra-short laser interaction with solids at non-relativistic intensities," *Physics Reports*, vol. 508, no. 4, pp. 91–243, 2011.

[32] C. B. Schaffer, *Interaction of femtosecond laser pulses with transparent materials*. PhD thesis, Harvard University, 2001.

[33] J. Chen and J. Beraun, "Numerical study of ultrashort laser pulse interactions with metal films," *Numerical Heat Transfer: Part A: Applications*, vol. 40, no. 1, pp. 1–20, 2001.

[34] A. Zoubir, C. Lopez, M. Richardson, and K. Richardson, "Femtosecond laser fabrication of tubular waveguides in poly (methyl methacrylate)," *Optics letters*, vol. 29, no. 16, pp. 1840–1842, 2004.

[35] S. Hirono, M. Kasuya, K. Matsuda, Y. Ozeki, K. Itoh, H. Mochizuki, and W. Watanabe, "Increasing diffraction efficiency by heating phase gratings formed by femtosecond laser irradiation in poly (methyl methacrylate)," *Applied Physics Letters*, vol. 94, no. 24, p. 241122, 2009.

[36] V. R. Bhardwaj, E. Simova, P. P. Rajeev, C. Hnatovsky, R. S. Taylor, D. M. Rayner, and P. B. Corkum, "Optically produced arrays of planar nanostructures inside fused silica," *Phys. Rev. Lett.*, vol. 96, p. 057404, Feb 2006.

[37] K. Tanabe, "Field enhancement around metal nanoparticles and nanoshells: a systematic investigation," *The Journal of Physical Chemistry C*, vol. 112, no. 40, pp. 15721–15728, 2008.

[38] J. Guay, A. Villafranca, F. Baset, K. Popov, L. Ramunno, and V. Bhardwaj, "Polarization-dependent femtosecond laser ablation of poly-methyl methacrylate," *New Journal of Physics*, vol. 14, no. 8, p. 085010, 2012.

[39] S. Juodkazis, K. Nishimura, S. Tanaka, H. Misawa, E. G. Gamaly, B. Luther-Davies, L. Hallo, P. Nicolai, and V. T. Tikhonchuk, "Laser-induced microexplosion confined in the bulk of a sapphire crystal: evidence of multimegabar pressures," *Physical review letters*, vol. 96, no. 16, p. 166101, 2006.

[40] S. S. Harilal, J. R. Freeman, P. K. Diwakar, and A. Hassanein, "Femtosecond laser ablation: Fundamentals and applications," in *Laser-Induced Breakdown Spectroscopy*, pp. 143–166, Springer, 2014.

[41] M. Henyk and J. Reif, "Negative ion emission from ionic crystals upon ultra short laser pulse irradiation," *Applied Surface Science*, vol. 208, pp. 71–76, 2003.

[42] S. Amoruso, X. Wang, C. Altucci, C. De Lisio, M. Armenante, R. Bruzzese, N. Spinelli, and R. Velotta, "Double-peak distribution of electron and ion emission profile during femtosecond laser ablation of metals," *Applied surface science*, vol. 186, no. 1, pp. 358–363, 2002.

[43] A. Royon, Y. Petit, G. Papon, M. Richardson, and L. Canioni, "Femtosecond laser induced photochemistry in materials tailored with photosensitive agents [invited]," *Optical Materials Express*, vol. 1, no. 5, pp. 866–882, 2011.

[44] W. Demtröder, "Laser spectroscopy 2," *Experimental techniques*, 2008.

[45] A. Ben-Yakar and R. L. Byer, "Femtosecond laser ablation properties of borosilicate glass," *Journal of applied physics*, vol. 96, no. 9, pp. 5316–5323, 2004.

[46] F. Di Niso, C. Gaudiuso, T. Sibillano, F. P. Mezzapesa, A. Ancona, and P. M. Lugarà, "Role of heat accumulation on the incubation effect in multi-shot laser ablation of stainless steel at high repetition rates," *Optics express*, vol. 22, no. 10, pp. 12200–12210, 2014.

[47] R. W. Boyd, *Nonlinear optics*. Academic press, 2003.

[48] D. Rayner, A. Naumov, and P. Corkum, "Ultrashort pulse non-linear optical absorption in transparent media," *Optics express*, vol. 13, no. 9, pp. 3208–3217, 2005.

[49] A. E. Pelling, F. S. Veraitch, C. P.-K. Chu, C. Mason, and M. A. Horton, "Mechanical dynamics of single cells during early apoptosis," *Cell motility and the cytoskeleton*, vol. 66, no. 7, pp. 409–422, 2009.

[50] C. Rulliere *et al.*, *Femtosecond laser pulses*. Springer, 2005.

[51] M. N. Polyanskiy, "Refractive index database." http://refractiveindex.info. Accessed june. 10, 2016.

[52] M. A. de Araújo, R. Silva, E. de Lima, D. P. Pereira, and P. C. de Oliveira, "Measurement of Gaussian laser beam radius using the knife-edge technique: improvement on data analysis," *Applied optics*, vol. 48, no. 2, pp. 393–396, 2009.

[53] A. Yoshida and T. Asakura, "A simple technique for quickly measuring the spot size of gaussian laser beams," *Optics & Laser Technology*, vol. 8, no. 6, pp. 273–274, 1976.

[54] P. D. Ngo, "Energy dispersive spectroscopy," in *Failure Analysis of Integrated Circuits*, pp. 205–215, Springer, 1999.

[55] P. Van der Heide, *X-ray photoelectron spectroscopy: an introduction to principles and practices*. John Wiley & Sons, 2011.

[56] T.-L. Wee, L. C. Schmidt, and J. C. Scaiano, "Photooxidation of 9-anthraldehyde catalyzed by gold nanoparticles: solution and single nanoparticle studies using fluorescence lifetime imaging," *The Journal of Physical Chemistry C*, vol. 116, no. 45, pp. 24373–24379, 2012.

[57] A. M. Streltsov and N. F. Borrelli, "Study of femtosecond-laser-written waveguides in glasses," *JOSA B*, vol. 19, no. 10, pp. 2496–2504, 2002.

[58] S. Sowa, W. Watanabe, T. Tamaki, J. Nishii, and K. Itoh, "Symmetric waveguides in poly (methyl methacrylate) fabricated by femtosecond laser pulses," *Optics Express*, vol. 14, no. 1, pp. 291–297, 2006.

[59] V. Bhardwaj, E. Simova, P. Rajeev, C. Hnatovsky, R. Taylor, D. Rayner, and P. Corkum, "Optically produced arrays of planar nanostructures inside fused silica," *Physical review letters*, vol. 96, no. 5, p. 057404, 2006.

[60] J.-K. Park and S.-H. Cho, "Flexible gratings fabricated in polymeric plate using femtosecond laser irradiation," *Optics and Lasers in Engineering*, vol. 49, no. 5, pp. 589–593, 2011.

[61] P. Scully, D. Jones, and D. Jaroszynski, "Femtosecond laser irradiation of polymethylmethacrylate for refractive index gratings," *Journal of Optics A: Pure and Applied Optics*, vol. 5, no. 4, p. S92, 2003.

[62] A. Marcinkevičius, S. Juodkazis, M. Watanabe, M. Miwa, S. Matsuo, H. Misawa, and J. Nishii, "Femtosecond laser-assisted three-dimensional microfabrication in silica," *Optics Letters*, vol. 26, no. 5, pp. 277–279, 2001.

[63] C. Hnatovsky, R. Taylor, E. Simova, P. Rajeev, D. Rayner, V. Bhardwaj, and P. Corkum, "Fabrication of microchannels in glass using focused femtosecond laser radiation and selective chemical etching," *Applied Physics A*, vol. 84, no. 1-2, pp. 47–61, 2006.

[64] R. S. Taylor, C. Hnatovsky, E. Simova, D. M. Rayner, V. Bhardwaj, and P. B. Corkum, "Femtosecond laser fabrication of nanostructures in silica glass," *Optics letters*, vol. 28, no. 12, pp. 1043–1045, 2003.

[65] Y.-H. Zhai, C. Goulart, J. E. Sharping, H. Wei, S. Chen, W. Tong, M. N. Slipchenko, D. Zhang, and J.-X. Cheng, "Multimodal coherent anti-Stokes Raman spectroscopic imaging with a fiber optical parametric oscillator," *Applied physics letters*, vol. 98, no. 19, p. 191106, 2011.

[66] M. F. Yanik, H. Cinar, H. N. Cinar, A. D. Chisholm, Y. Jin, and A. Ben-Yakar, "Neurosurgery: functional regeneration after laser axotomy," *Nature*, vol. 432, no. 7019, pp. 822–822, 2004.

[67] P. P. Rajeev, M. Gertsvolf, E. Simova, C. Hnatovsky, R. S. Taylor, V. R. Bhardwaj, D. M. Rayner, and P. B. Corkum, "Memory in nonlinear ionization of transparent solids," *Phys. Rev. Lett.*, vol. 97, p. 253001, Dec 2006.

[68] J. Peng, D. Grojo, D. M. Rayner, and P. B. Corkum, "Control of energy deposition in femtosecond laser dielectric interactions," *Applied Physics Letters*, vol. 102, no. 16, p. 161105, 2013.

[69] J. W. Chan, T. Huser, S. Risbud, and D. Krol, "Structural changes in fused silica after exposure to focused femtosecond laser pulses," *Optics letters*, vol. 26, no. 21, pp. 1726–1728, 2001.

[70] Y. Teng, J. Zhou, K. Sharafudeen, S. Zhou, K. Miura, and J. Qiu, "Space-selective crystallization of glass induced by femtosecond laser irradiation," *Journal of Non-Crystalline Solids*, vol. 383, pp. 91 – 96, 2014.

[71] Y. Izawa, S. Tokita, M. Fujita, M. Nakai, T. Norimatsu, and Y. Izawa, "Ultrathin amorphization of single-crystal silicon by ultraviolet femtosecond laser pulse irradiation," *Journal of Applied Physics*, vol. 105, no. 6, p. 064909, 2009.

[72] M. Shimizu, Y. Shimotsuma, M. Sakakura, T. Yuasa, H. Homma, Y. Minowa, K. Tanaka, K. Miura, and K. Hirao, "Periodic metallo-dielectric structure in diamond," *Optics express*, vol. 17, no. 1, pp. 46–54, 2009.

[73] S. F. Ahmed, G.-H. Rho, K.-R. Lee, A. Vaziri, and M.-W. Moon, "High aspect ratio wrinkles on a soft polymer," *Soft Matter*, vol. 6, no. 22, pp. 5709–5714, 2010.

[74] R. Kumar, S. A. Ali, A. Mahur, H. Virk, F. Singh, S. Khan, D. Avasthi, and R. Prasad, "Study of optical band gap and carbonaceous clusters in swift heavy ion

irradiated polymers with UV–Vis spectroscopy," *Nuclear Instruments and Methods In Physics Research Section B: Beam Interactions With Materials And Atoms*, vol. 266, no. 8, pp. 1788–1792, 2008.

[75] D. Fink, W. Chung, R. Klett, A. Schmoldt, J. Cardoso, R. Montiel, M. Vazquez, L. Wang, F. Hosoi, H. Omichi, *et al.*, "Carbonaceous clusters in irradiated polymers as revealed by UV-Vis spectrometry," *Radiation effects and defects in solids*, vol. 133, no. 3, pp. 193–208, 1995.

[76] V. Resta, G. Quarta, M. Lomascolo, L. Maruccio, and L. Calcagnile, "Raman and Photoluminescence spectroscopy of polycarbonate matrices irradiated with different energy 28 Si+ ions," *Vacuum*, vol. 116, pp. 82–89, 2015.

[77] R. Suriano, A. Kuznetsov, S. M. Eaton, R. Kiyan, G. Cerullo, R. Osellame, B. N. Chichkov, M. Levi, and S. Turri, "Femtosecond laser ablation of polymeric substrates for the fabrication of microfluidic channels," *Applied Surface Science*, vol. 257, no. 14, pp. 6243–6250, 2011.

[78] N. Morita, Y. Shimotsuma, M. Nishi, M. Sakakura, K. Miura, and K. Hirao, "Direct micro-carbonization inside polymer using focused femtosecond laser pulses," *Applied Physics Letters*, vol. 105, no. 20, p. 201104, 2014.

[79] S. Gupta, D. Choudhary, and A. Sarma, "Study of carbonaceous clusters in irradiated polycarbonate with UV–vis spectroscopy," *Journal of Polymer Science Part B: Polymer Physics*, vol. 38, no. 12, pp. 1589–1594, 2000.

[80] D. Fink, K. Ibel, P. Goppelt, J. Biersack, L. Wang, and M. Behar, "Ion beam induced carbon clusters in polymers," *Nuclear Instruments and Methods in Physics Research Section B: Beam Interactions with Materials and Atoms*, vol. 46, no. 1, pp. 342–346, 1990.

[81] A. V. Kiryanov *et al.*, "Electron-irradiation and photo-excitation darkening and bleaching of Yb doped silica fibers: Comparison," *Optics and Photonics Journal*, vol. 1, no. 04, p. 155, 2011.

[82] L. W. Tutt and T. F. Boggess, "A review of optical limiting mechanisms and devices using organics, fullerenes, semiconductors and other materials," *Progress in Quantum Electronics*, vol. 17, no. 4, pp. 299 – 338, 1993.

[83] J.-P. Lang, Z.-R. Sun, Q.-F. Xu, H. Yu, and K. Tatsumi, "Optical limiting properties of two organometallic half-open cubane-like cluster compounds $[(\eta^5\text{-}C_5Me_5)WS_3Cu_3Br_2(EPh_3)_2]$ (E= As, P)," *Materials chemistry and physics*, vol. 82, no. 2, pp. 493–498, 2003.

[84] P. Wang, H. Ming, J.-Y. Zhang, Z.-C. Liang, Y.-H. Lu, Q.-J. Zhang, J.-P. Xie, and Y.-P. Tian, "Nonlinear optical and optical-limiting properties of azobenzene liquid crystal polymer," *Optics Communications*, vol. 203, no. 12, pp. 159 – 162, 2002.

[85] V. Shukla, C. Singh, A. Srivastava, and K. Bindra, "Studies on Optical Limiting Characteristics of Silicon Nanoparticles Synthesized by Laser Ablation," *Journal of nanoscience and nanotechnology*, vol. 12, no. 6, pp. 4644–4649, 2012.

[86] M. Feng, H. Zhan, and Y. Chen, "Nonlinear optical and optical limiting properties of graphene families," *Applied Physics Letters*, vol. 96, no. 3, p. 033107, 2010.

[87] M. Frare, V. Weber, R. Signorini, and R. Bozio, "Gold nanoparticles in a polycarbonate matrix for optical limiting against a CW laser," *Laser Physics*, vol. 24, no. 10, p. 105901, 2014.

[88] T. Lippert, T. Nakamura, H. Niino, and A. Yabe, "Laser induced chemical and physical modifications of polymer films: dependence on the irradiation wavelength," *Applied surface science*, vol. 109, pp. 227–231, 1997.

[89] F. Raimondi, S. Abolhassani, R. Brütsch, F. Geiger, T. Lippert, J. Wambach, J. Wei, and A. Wokaun, "Quantification of polyimide carbonization after laser ablation," *Journal of Applied Physics*, vol. 88, no. 6, pp. 3659–3666, 2000.

[90] C. Wochnowski, Y. Cheng, Y. Hanada, K. Meteva, S. Metev, K. Sugioka, G. Sepold, F. Vollertsen, and K. Midorikawa, "Fs-laser-induced Fabrication of Polymeric Optical and Fluidic Microstructures," *Journal of Laser Micro Nanoengineering*, vol. 1, pp. 195–200, 2006.

[91] T. Lippert, "Laser application of polymers," in *Polymers and Light*, pp. 51–246, Springer, 2004.

[92] J. Tauc, R. Grigorovici, and A. Vancu, "Optical properties and electronic structure of amorphous germanium," *physica status solidi (b)*, vol. 15, no. 2, pp. 627–637, 1966.

[93] K. Shimakawa, J. Singh, and S. O′Leary, "Optical properties of disordered condensed matter," *Optical Properties of Condensed Matter and Applications*, pp. 47–62, 2006.

[94] V. Švorčík, O. Lyutakov, and I. Huttel, "Thickness dependence of refractive index and optical gap of PMMA layers prepared under electrical field," *Journal of Materials Science: Materials in Electronics*, vol. 19, no. 4, pp. 363–367, 2008.

[95] A. Piruska, I. Nikcevic, S. H. Lee, C. Ahn, W. R. Heineman, P. A. Limbach, and C. J. Seliskar, "The autofluorescence of plastic materials and chips measured under laser irradiation," *Lab on a Chip*, vol. 5, no. 12, pp. 1348–1354, 2005.

[96] S. Tiwari, F. Rana, H. Hanafi, A. Hartstein, E. F. Crabbe, and K. Chan, "A silicon nanocrystals based memory," *Appl. Phys. Lett.*, vol. 68, no. 10, p. 1377, 1996.

[97] H. B. Liao, R. F. Xiao, J. S. Fu, P. Yu, G. K. L. Wong, and P. Sheng, "Large third-order optical nonlinearity in Au:SiO_2 composite films near the percolation threshold," *Appl. Phys. Lett.*, vol. 70, no. 1, p. 1, 1997.

[98] D. M. Schaadt, E. T. Yu, S. Sankar, and A. E. Berkowitz, "Charge storage in Co nanoclusters embedded in SiO_2 by scanning force microscopy," *Appl. Phys. Lett.*, vol. 74, no. 3, p. 472, 1999.

[99] J. Fu, G. Li, X. Mao, and K. Fang, "Nanoscale Cementite Precipitates and Comprehensive Strengthening Mechanism of Steel," *Metall. Mater. Trans. A*, vol. 42, pp. 3797–3812, Aug. 2011.

[100] P. N. Hai, M. Yokoyama, S. Ohya, and M. Tanaka, "Spin polarized tunneling in III–V-based heterostructures with a ferromagnetic MnAs thin film and GaAs: MnAs nanoclusters," *Physica E: Low-dimensional Systems and Nanostructures*, vol. 32, no. 1, pp. 416–418, 2006.

[101] L. Shang, S. Dong, and G. U. Nienhaus, "Ultra-small fluorescent metal nanoclusters: Synthesis and biological applications," *Nano Today*, vol. 6, pp. 401–418, Aug. 2011.

[102] H. Al Dosari and A. I. Ayesh, "Nanocluster production for solar cell applications," *J. Appl. Phys.*, vol. 114, no. 5, p. 054305, 2013.

[103] S. Dhamodaran, A. Pathak, D. Avasthi, T. Srinivasan, R. Muralidharan, and D. Emfietzoglou, "Surface modification of InGaAs/GaAs heterostructures by swift heavy ion irradiation," *Nucl. Instruments Methods Phys. Res. Sect. B Beam Interact. with Mater. Atoms*, vol. 257, pp. 301–306, Apr. 2007.

[104] G. Marchi, F. Caccavale, F. Gonella, G. Mattei, P. Mazzoldi, G. Battaglin, and A. Quaranta, "Silver nanoclusters formation in ion-exchanged waveguides by annealing in hydrogen atmosphere," *Appl. Phys. A Mater. Sci. Process.*, vol. 63, pp. 403–407, Oct. 1996.

[105] F. Hanus, K. Kolev, A. Jadin, and L. Laude, "Excimer laser-induced copper nanocluster formation in mixed PMMA/copper acetylacetonate films," *Appl. Surf. Sci.*, vol. 154-155, pp. 320–323, Feb. 2000.

[106] K. Miura, J. Qiu, T. Mitsuyu, and K. Hirao, "Space-selective growth of frequency-conversion crystals in glasses with ultrashort infrared laser pulses," *Opt. Lett.*, vol. 25, p. 408, Mar. 2000.

[107] Y. Dai, B. Zhu, J. Qiu, H. Ma, B. Lu, S. Cao, and B. Yu, "Direct writing three-dimensional $Ba_2TiSi_2O_2$ crystalline pattern in glass with ultrashort pulse laser," *Appl. Phys. Lett.*, vol. 90, no. 18, p. 181109, 2007.

[108] S. Qu, J. Qiu, C. Zhao, X. Jiang, H. Zeng, C. Zhu, and K. Hirao, "Metal nanoparticle precipitation in periodic arrays in Au_2O-doped glass by two interfered femtosecond laser pulses," *Appl. Phys. Lett.*, vol. 84, no. 12, p. 2046, 2004.

[109] X. Hu, Q. Zhao, X. Jiang, C. Zhu, and J. Qiu, "Space-selective co-precipitation of silver and gold nanoparticles in femtosecond laser pulses irradiated Ag+, Au3+ co-doped silicate glass," *Solid State Commun.*, vol. 138, pp. 43–46, Apr. 2006.

[110] T. Gleitsmann, T. Bernhardt, and L. Wöste, "Luminescence properties of femtosecond-laser-activated silver oxide nanoparticles embedded in a biopolymer matrix," *Appl. Phys. A*, vol. 82, pp. 125–130, Sept. 2006.

[111] V. Volodin, T. Korchagina, J. Koch, and B. Chichkov, "Femtosecond laser induced formation of Si nanocrystals and amorphous Si clusters in silicon-rich nitride films," *Phys. E Low-dimensional Syst. Nanostructures*, vol. 42, pp. 1820–1823, Apr. 2010.

[112] A. Unal, A. Stalmashonak, G. Seifert, and H. Graener, "Ultrafast dynamics of silver nanoparticle shape transformation studied by femtosecond pulse-pair irradiation," *Phys. Rev. B*, vol. 79, p. 115411, Mar. 2009.

[113] A. Stalmashonak, H. Graener, and G. Seifert, "Transformation of silver nanospheres embedded in glass to nanodisks using circularly polarized femtosecond pulses," *Appl. Phys. Lett.*, vol. 94, no. 19, p. 193111, 2009.

[114] W. R. Creasy and J. T. Brenna, "Formation of high mass carbon cluster ions from laser ablation of polymers and thin carbon films," *J. Chem. Phys.*, vol. 92, no. 4, p. 2269, 1990.

[115] K. Shibagaki, N. Takada, K. Sasaki, and K. Kadota, "Synthetic characteristics of large carbon cluster ions by laser ablation of polymers in vacuum," *J. Appl. Phys.*, vol. 93, no. 1, p. 655, 2003.

[116] A. Bulgakov, I. Ozerov, and W. Marine, "Silicon clusters produced by femtosecond laser ablation: non-thermal emission and gas-phase condensation," *Appl. Phys. A*, vol. 79, pp. 1591–1594, July 2004.

[117] D. W. Bäuerle, *Laser processing and chemistry*, vol. 40. Springer, 2001.

[118] D. Fink, R. Klett, L. Chadderton, J. Cardoso, R. Montiel, H. Vazquez, and A. Karanovich, "Carbonaceous clusters in irradiated polymers as revealed by small angle X-ray scattering and ESR," *Nucl. Instrum. Methods Phys. Res., Sect. B*, vol. 111, pp. 303–314, May 1996.

[119] V.-M. Graubner, R. Jordan, O. Nuyken, B. Schnyder, T. Lippert, R. Kötz, and A. Wokaun, "Photochemical Modification of Cross-Linked Poly(dimethylsiloxane) by Irradiation at 172 nm," *Macromolecules*, vol. 37, pp. 5936–5943, Aug. 2004.

[120] Y. Liu, M. Shimizu, B. Zhu, Y. Dai, and B. Qian, "Micromodification of element distribution in glass using femtosecond laser irradiation," *Opt. Lett.*, vol. 34, no. 2, pp. 136–138, 2009.

[121] Y. Dai, G. Yu, M. He, H. Ma, X. Yan, and G. Ma, "High repetition rate femtosecond laser irradiation-induced elements redistribution in Ag-doped glass," *Appl. Phys. B*, vol. 103, pp. 663–667, Nov. 2011.

[122] G. Ledoux, O. Guillois, D. Porterat, C. Reynaud, F. Huisken, B. Kohn, and V. Paillard, "Photoluminescence properties of silicon nanocrystals as a function of their size," *Phys. Rev. B*, vol. 62, pp. 15942–15951, Dec. 2000.

[123] A. Kumar, F. Singh, J. Pivin, and D. Avasthi, "Photoluminescence studies of carbon clusters formed by irradiation of Si-based polymer," *Radiat. Meas.*, vol. 40, pp. 785–788, Nov. 2005.

[124] J. Pivin, M. Sendova-Vassileva, P. Colombo, and A. Martucci, "Photoluminescence of composite ceramics derived from polysiloxanes and polycarbosilanes by ion irradiation," *Mater. Sci. Eng. B*, vol. 69-70, pp. 574–577, Jan. 2000.

[125] J. C. Pivin, P. Colombo, and G. D. Sorarù, "Comparison of Ion Irradiation Effects in Silicon-Based Preceramic Thin Films," *J. Am. Ceram. Soc.*, vol. 83, no. 4, pp. 713–720, 2000.

[126] "Effect of proton irradiation on photoluminescent properties of PDMS-nanodiamond composites.," *Nanotechnology*, vol. 19, p. 455701, Nov. 2008.

[127] M. Sendova-Vassileva, N. Tzenov, D. Dimova-Malinovska, T. Marinova, and V. Krastev, "Visible luminescence from C-containing silicon oxide films," *Thin Solid Films*, vol. 276, pp. 318–322, Apr. 1996.

[128] H. He, Y. Wang, and H. Tang, "Intense ultraviolet and green photoluminescence from sol gel derived silica containing hydrogenated carbon," *J. Phys. Condens. Matter*, vol. 14, pp. 11867–11874, Nov. 2002.

[129] L. Patrone, D. Nelson, V. I. Safarov, M. Sentis, W. Marine, and S. Giorgio, "Photoluminescence of silicon nanoclusters with reduced size dispersion produced by laser ablation," *J. Appl. Phys.*, vol. 87, no. 8, p. 3829, 2000.

[130] S. C. Bae, H. Lee, Z. Lin, and S. Granick, "Chemical imaging in a surface forces apparatus: confocal raman spectroscopy of confined poly(dimethylsiloxane).," *Langmuir*, vol. 21, pp. 5685–8, June 2005.

[131] D. Cai, A. Neyer, and R "Raman, mid-infrared, near-infrared and ultraviolet–visible spectroscopy of PDMS silicone rubber for characterization of polymer optical waveguide materials," *Journal of Molecular Structure*, vol. 976, no. 1–3, pp. 274–281, 2010.

[132] A. Ferrari and J. Robertson, "Interpretation of Raman spectra of disordered and amorphous carbon," *Phys. Rev. B*, vol. 61, pp. 14095–14107, May 2000.

[133] S. C. Ray, A. Saha, N. R. Jana, and R. Sarkar, "Fluorescent Carbon Nanoparticles: Synthesis, Characterization, and Bioimaging Application," *J. Phys. Chem. C*, vol. 113, pp. 18546–18551, Oct. 2009.

[134] M. A. Gauthier, I. Stangel, T. H. Ellis, and X. X. Zhu, "A new method for quantifying the intensity of the C=C band of dimethacrylate dental monomers in their FTIR and Raman spectra.," *Biomaterials*, vol. 26, pp. 6440–8, Nov. 2005.

[135] Z. Iqbal and S. Veprek, "Raman scattering from hydrogenated microcrystalline and amorphous silicon," *J. Phys. C Solid State Phys.*, vol. 15, no. 2, p. 377, 1982.

[136] G. Viera, S. Huet, and L. Boufendi, "Crystal size and temperature measurements in nanostructured silicon using Raman spectroscopy," *J. Appl. Phys.*, vol. 90, no. 8, p. 4175, 2001.

[137] J. Zi, H. Buscher, C. Falter, W. Ludwig, K. Zhang, and X. Xie, "Raman shifts in Si nanocrystals," *Appl. Phys. Lett.*, vol. 69, no. 2, p. 200, 1996.

[138] G. Gouadec and P. Colomban, "Raman Spectroscopy of nanomaterials: How spectra relate to disorder, particle size and mechanical properties," *Prog. Cryst. Growth Charact. Mater.*, vol. 53, pp. 1–56, Mar. 2007.

[139] M. D. Borysiak, K. S. Bielawski, N. J. Sniadecki, C. F. Jenkel, B. D. Vogt, and J. D. Posner, "Simple replica micromolding of biocompatible styrenic elastomers," *Lab on a Chip*, vol. 13, no. 14, pp. 2773–2784, 2013.

[140] A. P. Demchenko, "The red-edge effects: 30 years of exploration," *Luminescence*, vol. 17, no. 1, pp. 19–42, 2002.

[141] K. A. Al-Hassan and M. A. El-Bayoumi, "Large edge-excitation red shift for a merocyanine dye in poly(vinyl alcohol) polymer matrix," *Journal of Polymer Science Part B: Polymer Physics*, vol. 25, no. 3, pp. 495–500, 1987.

[142] K. A. Al-Hassan and T. Azumi, "The red edge effect as a tool for investigating the origin of the anomalous fluorescence band of 9,9–bianthryl in rigid polar polymer matrices ," *Chemical Physics Letters*, vol. 150, no. 3–4, pp. 344–348, 1988.

[143] C. M. Rao, S. C. Rao, and P. B. Rao, "Red edge excitation effect in intact eye lens," *Photochemistry and Photobiology*, vol. 50, no. 3, pp. 399–402, 1989.

[144] C. N. Banwell, E. M. McCash, *et al.*, *Fundamentals of molecular spectroscopy*. McGraw-Hill London, 1972.

[145] S. R. Gaboury and M. W. Urban, "Microwave plasma reactions of solid monomers with silicone elastomer surfaces: a spectroscopic study," *Langmuir*, vol. 9, no. 11, pp. 3225–3233, 1993.

[146] D. Cai, A. Neyer, R. Kuckuk, and H. Heise, "Optical absorption in transparent PDMS materials applied for multimode waveguides fabrication," *Optical materials*, vol. 30, no. 7, pp. 1157–1161, 2008.

[147] Z. Nie, H. Lee, H. Yoo, Y. Lee, Y. Kim, K.-S. Lim, and M. Lee, "Multilayered optical bit memory with a high signal-to-noise ratio in fluorescent polymethylmethacrylate," *Applied Physics Letters*, vol. 94, no. 11, p. 111912, 2009.

[148] G. Pacchioni and G. Ierańo, "Ab initio theory of optical transitions of point defects in SiO_2 ," *Phys. Rev. B*, vol. 57, no. 2, pp. 818–832, 1998.

[149] K. Raghavachari, D. Ricci, and G. Pacchioni, "Optical properties of point defects in SiO_2 from time-dependent density functional theory," *J. Chem. Phys.*, vol. 116, no. 2, p. 825, 2002.

[150] T. Uchino, N. Kurumoto, and N. Sagawa, "Structure and formation mechanism of blue-light-emitting centers in silicon and silica-based nanostructured materials," *Phys. Rev. B*, vol. 73, p. 233203, June 2006.

[151] A. S. Zyubin, A. M. Mebel, S. H. Lin, and Y. D. Glinka, "Photoluminescence of silanone and dioxasilyrane groups in silicon oxides: A theoretical study," *J. Chem. Phys.*, vol. 116, no. 22, p. 9889, 2002.

[152] A. Nishimura, N. Sagawa, and T. Uchino, "Structural Origin of Visible Luminescence from Silica Based Organic–Inorganic Hybrid Materials," *The Journal of Physical Chemistry C*, vol. 113, no. 11, pp. 4260–4262, 2009.

[153] A. Nishimura, S. Harada, and T. Uchino, "Effect of Cross-Linking and Organic Groups on the Visible Photoluminescence Characteristics of n-Octadecylsiloxanes," *The Journal of Physical Chemistry C*, vol. 114, no. 18, pp. 8568–8574, 2010.

[154] S. Wan, Q. Cao, and C. Xie, "Optical storage: an emerging option in long-term digital preservation," *Frontiers of Optoelectronics*, vol. 7, no. 4, pp. 486–492, 2014.

[155] J. Zhang, M. Gecevičius, M. Beresna, and P. G. Kazansky, "Seemingly unlimited lifetime data storage in nanostructured glass," *Physical review letters*, vol. 112, no. 3, p. 033901, 2014.

[156] E. Glezer, M. Milosavljevic, L. Huang, R. Finlay, T.-H. Her, J. P. Callan, and E. Mazur, "Three-dimensional optical storage inside transparent materials," *Optics Letters*, vol. 21, no. 24, pp. 2023–2025, 1996.

[157] H. Ruan, "Recent advances in holographic data storage," *Frontiers of Optoelectronics*, vol. 7, no. 4, pp. 450–466, 2014.

[158] L. Huang, X. Chen, H. Mühlenbernd, H. Zhang, S. Chen, B. Bai, Q. Tan, G. Jin, K.-W. Cheah, C.-W. Qiu, *et al.*, "Three-dimensional optical holography using a plasmonic metasurface," *Nature communications*, vol. 4, 2013.

[159] Y. Shao, H. Wang, Q. Zhang, and Y. Li, "Fabrication of large-area and high-crystallinity photoreduced graphene oxide films via reconstructed two-dimensional multilayer structures," *NPG Asia Materials*, vol. 6, no. 8, p. e119, 2014.

[160] P. Zijlstra, J. W. Chon, and M. Gu, "Five-dimensional optical recording mediated by surface plasmons in gold nanorods," *Nature*, vol. 459, no. 7245, pp. 410–413, 2009.

[161] Z. Gan, Y. Cao, R. A. Evans, and M. Gu, "Three-dimensional deep sub-diffraction optical beam lithography with 9 nm feature size," *Nature communications*, vol. 4, 2013.

[162] A. Royon, K. Bourhis, M. Bellec, G. Papon, B. Bousquet, Y. Deshayes, T. Cardinal, and L. Canioni, "Silver clusters embedded in glass as a perennial high capacity optical recording medium," *Advanced materials*, vol. 22, no. 46, pp. 5282–5286, 2010.

[163] B. H. Cumpston, S. P. Ananthavel, S. Barlow, D. L. Dyer, J. E. Ehrlich, L. L. Erskine, A. A. Heikal, S. M. Kuebler, I.-Y. S. Lee, D. McCord-Maughon, *et al.*, "Two-photon polymerization initiators for three-dimensional optical data storage and microfabrication," *Nature*, vol. 398, no. 6722, pp. 51–54, 1999.

[164] J. H. Strickler and W. W. Webb, "Three-dimensional optical data storage in refractive media by two-photon point excitation," *Optics Letters*, vol. 16, no. 22, pp. 1780–1782, 1991.

[165] M. Beresna, M. Gecevičius, P. G. Kazansky, T. Taylor, and A. V. Kavokin, "Exciton mediated self-organization in glass driven by ultrashort light pulses," *Applied Physics Letters*, vol. 101, no. 5, p. 053120, 2012.

[166] H. Sun, S. Liu, W. Lin, K. Y. Zhang, W. Lv, X. Huang, F. Huo, H. Yang, G. Jenkins, Q. Zhao, *et al.*, "Smart responsive phosphorescent materials for data recording and security protection," *Nature communications*, vol. 5, 2014.

[167] M. Gu, X. Li, and Y. Cao, "Optical storage arrays: a perspective for future big data storage," *Light: Science & Applications*, vol. 3, no. 5, p. e177, 2014.

[168] K. Deepak, R. Kuladeep, S. V. Rao, and D. N. Rao, "Luminescent microstructures in bulk and thin films of PMMA, PDMS, PVA, and PS fabricated using femtosecond direct writing technique," *Chemical Physics Letters*, vol. 503, no. 1, pp. 57–60, 2011.

[169] R. Nurmukhametov, L. Volkova, and S. Kabanov, "Fluorescence and absorption of polystyrene exposed to UV laser radiation," *Journal of Applied Spectroscopy*, vol. 73, no. 1, pp. 55–60, 2006.

[170] Z. Liu, W. Xue, Z. Cai, G. Zhang, and D. Zhang, "A facile and convenient fluorescence detection of gamma-ray radiation based on the aggregation-induced emission," *Journal of Materials Chemistry*, vol. 21, no. 38, pp. 14487–14491, 2011.

[171] C. Barrios, S. Carrasco, V. Canalejas-Tejero, D. López-Romero, F. Navarro-Villoslada, M. Moreno-Bondi, J. Fierro, and M. Capel-Sánchez, "Fabrication of luminescent nanostructures by electron-beam direct writing of PMMA resist," *Materials Letters*, vol. 88, pp. 93–96, 2012.

[172] http://naturemappingfoundation.org/natmap/facts/canada_goose_k6.html,.

[173] http://www.naturespicsonline.com/.

[174] http://creativecommons.org/licenses/by-sa/3.0/.

[175] I. Goldfarb, R. McHenry, and E. Penski, "Thermal degradation of polymers. I. Aspects of polytetrafluoroethylene degradation," *Journal of Polymer Science*, vol. 58, no. 166, pp. 1283–1291, 1962.

[176] R. Al-Itry, K. Lamnawar, and A. Maazouz, "Improvement of thermal stability, rheological and mechanical properties of PLA, PBAT and their blends by reactive extrusion with functionalized epoxy," *Polymer Degradation and Stability*, vol. 97, no. 10, pp. 1898–1914, 2012.

[177] M. Ferriol, A. Gentilhomme, M. Cochez, N. Oget, and J. Mieloszynski, "Thermal degradation of poly (methyl methacrylate)(PMMA): modelling of DTG and TG curves," *Polymer degradation and stability*, vol. 79, no. 2, pp. 271–281, 2003.

[178] S. I. Stoliarov, P. R. Westmoreland, M. R. Nyden, and G. P. Forney, "A reactive molecular dynamics model of thermal decomposition in polymers: I. Poly (methyl methacrylate)," *Polymer*, vol. 44, no. 3, pp. 883–894, 2003.

[179] C. Lu, M. M.-C. Cheng, A. Benatar, and L. J. Lee, "Embossing of high-aspect-ratio-microstructures using sacrificial templates and fast surface heating," *Polymer Engineering & Science*, vol. 47, no. 6, pp. 830–840, 2007.

[180] A. Baum, P. J. Scully, W. Perrie, D. Jones, R. Issac, and D. A. Jaroszynski, "Pulse-duration dependency of femtosecond laser refractive index modification in poly (methyl methacrylate)," *Optics letters*, vol. 33, no. 7, pp. 651–653, 2008.

[181] A. Baum, P. J. Scully, M. Basanta, C. P. Thomas, P. R. Fielden, N. J. Goddard, W. Perrie, and P. R. Chalker, "Photochemistry of refractive index structures in poly (methyl methacrylate) by femtosecond laser irradiation," *Optics letters*, vol. 32, no. 2, pp. 190–192, 2007.

[182] http://www.sigmaaldrich.com/materials-science/material-science-products.html. Accessed Jan. 08, 2016.

[183] https://www.dispersions-pigments.basf.com. Accessed Jan. 08, 2016.

[184] http://www.mpi-chemie.com/category/uv-absorbers.html. Accessed Jan. 08, 2016.

[185] J. Rieker, E. Lemmert-Schmitt, G. Goeller, M. Roessler, G. J. Stueber, H. Schettler, H. E. Kramer, J. J. Stezowski, and H. Hoier, "Ultraviolet stabilizers of the 2-(hydroxyphenyl) benzotriazole class: influence of substituents on structure and spectra," *The Journal of Physical Chemistry*, vol. 96, no. 25, pp. 10225–10234, 1992.

[186] A. P. Demchenko, "The red-edge effects: 30 years of exploration," *Luminescence*, vol. 17, no. 1, pp. 19–42, 2002.

[187] C. Rao, S. C. Rao, P. B. Rao, *et al.*, "Red edge excitation effect in intact eye lens," *Photochemistry and photobiology*, vol. 50, no. 3, pp. 399–402, 1989.

[188] B. Dickens, J. Martin, and D. Waksman, "Thermal and photolytic degradation of plates of poly (methyl methacrylate) containing monomer," *Polymer*, vol. 25, no. 5, pp. 706–715, 1984.

[189] U. Hersel, C. Dahmen, and H. Kessler, "modified polymers: biomaterials for stimulated cell adhesion and beyond," *Biomaterials*, vol. 24, no. 24, pp. 4385 – 4415, 2003.

[190] R. S. Kane, S. Takayama, E. Ostuni, D. E. Ingber, and G. M. Whitesides, "Patterning proteins and cells using soft lithography," *Biomaterials*, vol. 20, no. 23–24, pp. 2363–2376, 1999.

[191] C. A. Scotchford, E. Cooper, G. J. Leggett, and S. Downes, "Growth of human osteoblast-like cells on alkanethiol on gold self-assembled monolayers: The effect of surface chemistry," *Journal of Biomedical Materials Research*, vol. 41, no. 3, 1998.

[192] E. Ostuni, L. Yan, and G. M. Whitesides, "The interaction of proteins and cells with self-assembled monolayers of alkanethiolates on gold and silver," *Colloids and Surfaces B: Biointerfaces*, vol. 15, no. 1, pp. 3 – 30, 1999.

[193] S. Saneinejad and M. S. Shoichet, "Patterned glass surfaces direct cell adhesion and process outgrowth of primary neurons of the central nervous system," *Journal of Biomedical Materials Research*, vol. 42, no. 1, pp. 13–19, 1998.

[194] D. V. Nicolau, T. Taguchi, H. Taniguchi, H. Tanigawa, and S. Yoshikawa, "Patterning neuronal and glia cells on light-assisted functionalised photoresists," *Biosensors and Bioelectronics*, vol. 14, no. 3, pp. 317 – 325, 1999.

[195] C. A. Goubko, *Development of a Dynamic Cell Patterning Strategy on a Hyaluronic Acid Hydrogel*. PhD thesis, Université d'Ottawa/University of Ottawa, 2014.

[196] J. Meyle, K. Gültig, and W. Nisch, "Variation in contact guidance by human cells on a microstructured surface," *Journal of biomedical materials research*, vol. 29, no. 1, pp. 81–88, 1995.

[197] C. Oakley and D. M. Brunette, "The sequence of alignment of microtubules, focal contacts and actin filaments in fibroblasts spreading on smooth and grooved titanium substrata.," *Journal of cell science*, vol. 106 (Pt 1), pp. 343–354, 1993.

[198] A. I. Teixeira, G. A. Abrams, P. J. Bertics, C. J. Murphy, and P. F. Nealey, "Epithelial contact guidance on well-defined micro-and nanostructured substrates," *Journal of cell science*, vol. 116, no. 10, pp. 1881–1892, 2003.

[199] B. Wójciak-Stothard, A. Curtis, W. Monaghan, K. Macdonald, and C. Wilkinson, "Guidance and activation of murine macrophages by nanometric scale topography," *Experimental cell research*, vol. 223, no. 2, pp. 426–435, 1996.

[200] D. Fuard, T. Tzvetkova-Chevolleau, S. Decossas, P. Tracqui, and P. Schiavone, "Optimization of poly-di-methyl-siloxane (PDMS) substrates for studying cellular adhesion and motility," *Microelectronic Engineering*, vol. 85, no. 5, pp. 1289–1293, 2008.

[201] D. Xie, B. Ngoi, Y. Fu, A. Ong, and B. Lim, "Etching characteristics of TiNi thin film by focused ion beam," *Applied Surface Science*, vol. 225, no. 14, pp. 54 – 58, 2004.

[202] H. Thissen, J. P. Hayes, P. Kingshott, G. Johnson, E. C. Harvey, and H. J. Griesser, "Nanometer thickness laser ablation for spatial control of cell attachment," *Smart Materials and Structures*, vol. 11, no. 5, p. 792, 2002.

[203] Y. Nakayama and T. Matsuda, "Surface microarchitectural design in biomedical applications: Preparation of microporous polymer surfaces by an excimer laser ablation technique," *Journal of Biomedical Materials Research*, vol. 29, no. 10, pp. 1295–1301, 1995.

[204] A. Heisterkamp, I. Z. Maxwell, E. Mazur, J. M. Underwood, J. A. Nickerson, S. Kumar, and D. E. Ingber, "Pulse energy dependence of subcellular dissection by femtosecond laser pulses," *Opt. Express*, vol. 13, pp. 3690–3696, May 2005.

[205] H. Lubatschowski, G. Maatz, A. Heisterkamp, U. Hetzel, W. Drommer, H. Welling, and W. Ertmer, "Application of ultrashort laser pulses for intrastromal refractive surgery," *Graefe's Archive for Clinical and Experimental Ophthalmology*, vol. 238, no. 1, pp. 33–39, 2000.

[206] S. H. Chung and E. Mazur, "Surgical applications of femtosecond lasers," *Journal of Biophotonics*, vol. 2, no. 10, pp. 557–572, 2009.

[207] P. S. Tsai, B. Friedman, A. I. Ifarraguerri, B. D. Thompson, V. Lev-Ram, C. B. Schaffer, Q. Xiong, R. Y. Tsien, J. A. Squier, and D. Kleinfeld, "All-Optical Histology Using Ultrashort Laser Pulses," *Neuron*, vol. 39, no. 1, pp. 27 – 41, 2003.

[208] T. Nuutinen, M. Silvennoinen, K. Päiväsaari, and P. Vahimaa, "Control of cultured human cells with femtosecond laser ablated patterns on steel and plastic surfaces," *Biomedical microdevices*, vol. 15, no. 2, pp. 279–288, 2013.

[209] A. Ranella, M. Barberoglou, S. Bakogianni, C. Fotakis, and E. Stratakis, "Tuning cell adhesion by controlling the roughness and wettability of 3D micro/nano silicon structures," *Acta Biomaterialia*, vol. 6, no. 7, pp. 2711 – 2720, 2010.

[210] Ulmeanu, M. and E. Sima, L. and Ursescu, D. and Enculescu, M. and Bazan, X. and Quintana, I., "Cell adhesion response on femtosecond laser initiated liquid assisted silicon surface," *Current Topics in Medicinal Chemistry*, vol. 14, no. 5, pp. 624–629, 2014.

[211] X. Ma, H. Huo, M. Wei, L. Wang, M. Shen, C. Barry, and J. Mead, "Enhanced protein binding on femtosecond laser ablated poly (methyl methacrylate) surfaces," *Applied Physics Letters*, vol. 98, no. 17, p. 171101, 2011.

[212] U. Reich, P. P. Mueller, E. Fadeeva, B. N. Chichkov, T. Stoever, T. Fabian, T. Lenarz, and G. Reuter, "Differential fine-tuning of cochlear implant material–cell interactions by femtosecond laser microstructuring," *Journal of Biomedical Materials Research Part B: Applied Biomaterials*, vol. 87, no. 1, pp. 146–153, 2008.

[213] Y. Liu, S. Sun, S. Singha, M. R. Cho, and R. J. Gordon, "3D femtosecond laser patterning of collagen for directed cell attachment," *Biomaterials*, vol. 26, no. 22, pp. 4597 – 4605, 2005.

[214] B. L.-P. Lee, H. Jeon, A. Wang, Z. Yan, J. Yu, C. Grigoropoulos, and S. Li, "Femtosecond laser ablation enhances cell infiltration into three-dimensional electrospun scaffolds," *Acta Biomaterialia*, vol. 8, no. 7, pp. 2648 – 2658, 2012.

[215] W. Y. Yeong, H. Yu, K. P. Lim, K. L. G. Ng, Y. C. F. Boey, V. S. Subbu, and L. P. Tan, "Multiscale topological guidance for cell alignment via direct laser writing on biodegradable polymer.," *Tissue engineering. Part C, Methods*, vol. 16, no. 5, pp. 1011–1021, 2010.

[216] S. Schlie, E. Fadeeva, J. Koch, A. Ngezahayo, and B. N. Chichkov, "Femtosecond laser fabricated spike structures for selective control of cellular behavior.," *Journal of biomaterials applications*, vol. 25, no. 3, pp. 217–233, 2010.

[217] B. D. Ratner, *Biomaterials science: an introduction to materials in medicine*. Academic press, 2004.

[218] G. MJ, B. A, C. WJ, G. RA, and D. RS, "Long-term efficacy of biomodeled polymethyl methacrylate implants for orbitofacial defects," *Archives of Facial Plastic Surgery*, vol. 8, no. 6, pp. 381–389, 2006.

[219] L. Wang, B. Sun, K. S. Ziemer, G. A. Barabino, and R. L. Carrier, "Chemical and physical modifications to poly(dimethylsiloxane) surfaces affect adhesion of Caco-2 cells," *Journal of Biomedical Materials Research Part A*, vol. 93A, no. 4, pp. 1260–1271, 2010.

[220] S. Kidambi, N. Udpa, S. A. Schroeder, R. Findlan, I. Lee, and C. Chan, "Cell adhesion on polyelectrolyte multilayer coated polydimethylsiloxane surfaces with varying topographies," *Tissue engineering*, vol. 13, no. 8, pp. 2105–2117, 2007.

[221] S. Darvishi, T. Cubaud, and J. P. Longtin, "Ultrafast laser machining of tapered microchannels in glass and PDMS," *Optics and Lasers in Engineering*, vol. 50, no. 2, pp. 210–214, 2012.

[222] A. Lafuma and D. Quéré, "Superhydrophobic states," *Nature materials*, vol. 2, no. 7, pp. 457–460, 2003.

[223] T. O. Yoon, H. J. Shin, S. C. Jeoung, and Y.-I. Park, "Formation of superhydrophobic poly (dimethysiloxane) by ultrafast laser-induced surface modification," *Optics express*, vol. 16, no. 17, pp. 12715–12725, 2008.

[224] A. M. Kietzig, S. G. Hatzikiriakos, and P. Englezos, "Patterned superhydrophobic metallic surfaces," *Langmuir*, vol. 25, no. 8, pp. 4821–4827, 2009.

[225] B. Wu, M. Zhou, J. Li, X. Ye, G. Li, and L. Cai, "Superhydrophobic surfaces fabricated by microstructuring of stainless steel using a femtosecond laser," *Applied Surface Science*, vol. 256, no. 1, pp. 61 – 66, 2009.

[226] S. Moradi, S. Kamal, P. Englezos, and S. G. Hatzikiriakos, "Femtosecond laser irradiation of metallic surfaces: effects of laser parameters on superhydrophobicity," *Nanotechnology*, vol. 24, no. 41, p. 415302, 2013.

[227] A. Vorobyev and C. Guo, "Femtosecond laser modification of material wetting properties: a brief review," *Science of Advanced Materials*, vol. 4, no. 3-4, pp. 432–438, 2012.

[228] T. Baldacchini, J. E. Carey, M. Zhou, and E. Mazur, "Superhydrophobic Surfaces Prepared by Microstructuring of Silicon Using a Femtosecond Laser," *Langmuir*, vol. 22, no. 11, pp. 4917–4919, 2006.

[229] D. Zhang, F. Chen, Q. Yang, J. Yong, H. Bian, Y. Ou, J. Si, X. Meng, and X. Hou, "A simple way to achieve pattern-dependent tunable adhesion in superhydrophobic surfaces by a femtosecond laser," *ACS applied materials & interfaces*, vol. 4, no. 9, pp. 4905–4912, 2012.

[230] M. Cardoso, V. Tribuzi, D. Balogh, L. Misoguti, and C. Mendonça, "Laser microstructuring for fabricating superhydrophobic polymeric surfaces," *Applied Surface Science*, vol. 257, no. 8, pp. 3281–3284, 2011.

[231] H. Pazokian, A. Selimis, J. Barzin, S. Jelvani, M. Mollabashi, C. Fotakis, and E. Stratakis, "Tailoring the wetting properties of polymers from highly hydrophilic to superhydrophobic using UV laser pulses," *Journal of Micromechanics and Microengineering*, vol. 22, no. 3, p. 035001, 2012.

[232] C. De Marco, S. M. Eaton, R. Suriano, S. Turri, M. Levi, R. Ramponi, G. Cerullo, and R. Osellame, "Surface properties of femtosecond laser ablated PMMA," *ACS applied materials & interfaces*, vol. 2, no. 8, pp. 2377–2384, 2010.

[233] P. Louette, F. Bodino, and J.-J. Pireaux, "Poly(dimethyl siloxane) (PDMS) XPS Reference Core Level and Energy Loss Spectra," *Surface Science Spectra*, vol. 12, no. 1, 2005.

[234] J. Zhou, A. V. Ellis, and N. H. Voelcker, "Recent developments in PDMS surface modification for microfluidic devices," *Electrophoresis*, vol. 31, no. 1, pp. 2–16, 2010.

[235] C. M. Weikart and H. K. Yasuda, "Modification, degradation, and stability of polymeric surfaces treated with reactive plasmas," *Journal of Polymer Science Part A: Polymer Chemistry*, vol. 38, no. 17, pp. 3028–3042, 2000.

[236] J. Yong, F. Chen, Q. Yang, D. Zhang, G. Du, J. Si, F. Yun, and X. Hou, "Femtosecond Laser Weaving Superhydrophobic Patterned PDMS Surfaces with Tunable Adhesion," *The Journal of Physical Chemistry C*, vol. 117, no. 47, pp. 24907–24912, 2013.

[237] E. Fadeeva, S. Schlie, J. Koch, A. Ngezahayo, and B. N. Chichkov, "The hydrophobic properties of femtosecond laser fabricated spike structures and their effects on cell proliferation," *physica status solidi (a)*, vol. 206, no. 6, pp. 1348–1351, 2009.

[238] E. Fadeeva, V. K. Truong, M. Stiesch, B. N. Chichkov, R. J. Crawford, J. Wang, and E. P. Ivanova, "Bacterial retention on superhydrophobic titanium surfaces fabricated by femtosecond laser ablation," *Langmuir*, vol. 27, no. 6, pp. 3012–3019, 2011.

[239] S. M. Oliveira, W. Song, N. M. Alves, and J. F. Mano, "Chemical modification of bioinspired superhydrophobic polystyrene surfaces to control cell attachment/proliferation," *Soft Matter*, vol. 7, pp. 8932–8941, 2011.

[240] B. Valamehr, S. J. Jonas, J. Polleux, R. Qiao, S. Guo, E. H. Gschweng, B. Stiles, K. Kam, T.-J. M. Luo, O. N. Witte, X. Liu, B. Dunn, and H. Wu, "Hydrophobic surfaces for enhanced differentiation of embryonic stem cell-derived embryoid bodies," *Proceedings of the National Academy of Sciences*, vol. 105, no. 38, pp. 14459–14464, 2008.

[241] J. Kim, Y.-H. Shin, S.-H. Yun, D.-S. Choi, J.-H. Nam, S. R. Kim, S.-K. Moon, B. H. Chung, J.-H. Lee, J.-H. Kim, K.-Y. Kim, K.-M. Kim, and J.-H. Lim, "Direct-Write Patterning of Bacterial Cells by Dip-Pen Nanolithography," *Journal of the American Chemical Society*, vol. 134, no. 40, pp. 16500–16503, 2012.

[242] Y. Ma, M. Zhou, S. Walter, J. Liang, Z. Chen, and L. Wu, "Selective adhesion and controlled activity of yeast cells on honeycomb-patterned polymer films via a microemulsion approach," *Chemical Communications*, vol. 50, no. 100, pp. 15882–15885, 2014.